

# Measuring our universe from galaxy redshift surveys

Ofer Lahav<sup>(1)</sup> and Yasushi Suto<sup>(2),(3)</sup>

<sup>(1)</sup> Institute of Astronomy, University of Cambridge,  
Madingley Road, Cambridge CB3 0HA, UK

<sup>(2)</sup> Department of Physics, The University of Tokyo,  
Tokyo 113-0033, Japan

<sup>(2)</sup> Research Center for the Early Universe, School of Science,  
The University of Tokyo, Tokyo 113-0033, Japan

e-mail: [lahav@ast.cam.ac.uk](mailto:lahav@ast.cam.ac.uk), [suto@phys.s.u-tokyo.ac.jp](mailto:suto@phys.s.u-tokyo.ac.jp)

(last modified: June 13, 2019)

## Abstract

Galaxy redshift surveys have achieved significant progress over the last couple of decades. Those surveys tell us how our universe looks like visually in the most straightforward manner. While the galaxy distribution traces the *bright* side of the universe, detailed quantitative analyses of the data have even revealed the *dark* side of the universe dominated by non-baryonic dark matter as well as more mysterious dark energy (or Einstein's cosmological constant). We describe several methodologies of using galaxy redshift surveys as cosmological probes, and then summarize the recent results from the existing surveys. Finally we present our views on the future of redshift surveys in the era of Precision Cosmology.

# Contents

<b>1</b>	<b>Introduction</b>	<b>4</b>
<b>2</b>	<b>Clustering in the expanding universe</b>	<b>6</b>
2.1	The cosmological principle . . . . .	6
2.2	From the Einstein equation to the Friedmann equation . . . . .	8
2.3	Expansion law and age of the universe . . . . .	11
2.4	Einstein's static model and Lemaître's model . . . . .	12
2.5	Vacuum energy as an effective cosmological constant . . . . .	14
2.6	Gravitational instability . . . . .	14
2.7	Linear growth rate of the density fluctuation . . . . .	16
<b>3</b>	<b>Statistics of cosmological density fluctuations</b>	<b>19</b>
3.1	Gaussian random field . . . . .	19
3.2	Log-normal distribution . . . . .	20
3.3	Higher-order correlation functions . . . . .	23
3.4	Genus statistics . . . . .	24
3.5	Minkowski functionals . . . . .	27
<b>4</b>	<b>Galaxy biasing</b>	<b>29</b>
4.1	Concepts and definitions of biasing . . . . .	29
4.2	Modeling biasing . . . . .	29
4.3	Density peaks and dark matter halos as toy models for galaxy biasing . . . . .	31
4.4	Biasing of galaxies in cosmological hydrodynamic simulations . .	36
4.5	Halo occupation function approach for galaxy biasing . . . . .	41
<b>5</b>	<b>Relativistic effects observable in clustering at high redshifts</b>	<b>43</b>
5.1	Cosmological lightcone effect on the two-point correlation functions	43
5.2	Evaluating two-point correlation functions from N-body simulation data . . . . .	46
5.3	Cosmological redshift-space distortion . . . . .	49
5.4	Two-Point Clustering Statistics on a Light-Cone in Cosmological Redshift Space . . . . .	52
<b>6</b>	<b>Recent results from 2dF and SDSS</b>	<b>57</b>
6.1	The latest galaxy redshift surveys . . . . .	57
6.1.1	The 2dF galaxy redshift survey . . . . .	57
6.1.2	The SDSS galaxy redshift survey . . . . .	58
6.1.3	The 6dF galaxy redshift survey . . . . .	61
6.1.4	The DEEP galaxy redshift survey . . . . .	61
6.1.5	The VIRMOS galaxy redshift survey . . . . .	61
6.2	Cosmological parameters from 2dFGRS . . . . .	62

6.2.1	The Power spectrum of 2dF Galaxies on large scales . . . . .	62
6.2.2	An upper limit on neutrino masses . . . . .	62
6.2.3	Combining 2dFGRS & CMB . . . . .	62
6.2.4	Redshift-space distortion . . . . .	64
6.3	Luminosity and spectral-type dependence of galaxy clustering . . . . .	64
6.3.1	2dFGRS: Clustering per luminosity and spectral type . . . . .	64
6.3.2	SDSS: Clustering per luminosity and colour . . . . .	68
6.4	Topology of the universe: analysis of SDSS galaxies in terms of Minkowski functionals . . . . .	68
6.5	Other statistical measures . . . . .	70
<b>7</b>	<b>Discussion</b>	<b>72</b>
<b>8</b>	<b>Acknowledgements</b>	<b>75</b>

# 1 Introduction

Nowadays the exploration of the universe can be performed by a variety of observational probes and methods over a wide range of the wavelengths; temperature anisotropy map of the cosmic microwave background (CMB), the Hubble diagrams of nearby galaxies and distant Type Ia supernovae, wide-field photometric and spectroscopic surveys of galaxies, power spectrum and abundances of galaxy clusters in optical and X-ray bands combined with the radio observation through the Sunyaev–Zel’dovich effect, deep surveys of galaxies in submm, infrared, and optical bands, quasar surveys in radio and optical, strong and weak lensing of distant galaxies and quasars, high-energy cosmic rays and so on. Undoubtedly gamma-rays, neutrinos, gravitational radiations will join the above already crowded list.

Among those, optical galaxy redshift surveys are the most classical. Indeed one may phrase that the modern observational cosmology started with a sort of a galaxy redshift survey by Edwin Hubble. Still galaxy redshift surveys are of vital importance in cosmology in the 21st century for various reasons:

## **Redshift surveys with the unprecedented quantity and quality:**

The numbers of galaxies and quasars in the spectroscopic sample of Two Degree Field (2dF) are  $\sim 250,000$  and  $\sim 30,000$ , and will reach  $\sim 800,000$  and  $100,000$  upon completion of the on-going Sloan Digital Sky Survey (SDSS). These unprecedented numbers of the objects as well as the homogeneous selection criteria enable the precise statistical analysis of their distribution.

## **The universe at $z \approx 1000$ is well specified:**

The first-year WMAP (*Wilkinson Microwave Anisotropy Probe*) data [5] among others have established a set of cosmological parameters. This may be taken as the *initial condition* of the universe from the point-of-view of the structure evolution toward  $z = 0$ . In a sense, the origin of the universe at  $z \approx 1000$  and the evolution of the universe after the epoch are now equally important, but well separable questions that particle and observational cosmologists focus on, respectively.

## **Gravitational growth of dark matter component is well understood:**

In addition, extensive numerical simulations of structure formation in the universe has significantly advanced our understanding of the gravitational evolution of dark matter component in the standard gravitational instability picture. In fact, we even have very accurate and useful analytic formulae to describe the evolution deep in its nonlinear regime. Thus we can now directly address the evolution of *visible objects* from the analysis of their redshift surveys separately from the nonlinear growth of the underlying dark matter gravitational potentials.

### **Formation and evolution of galaxies:**

In the era of precision cosmology among others, scientific goals of researches out of galaxy redshift surveys are gradually shifting from inferring a set of values of cosmological parameters using galaxy as their probes to understanding the origin and evolution of galaxy distribution given a set of parameters accurately determined by the other probes like CMB and supernovae.

With the above in mind, we will attempt to summarize what we have learned so far from galaxy redshift surveys and then to describe what will be done with future data. The review is organized as follows. We first present a brief overview of the Friedmann model and gravitational instability theory in §2. Then we describe the non-Gaussian nature of density fluctuations generated by the nonlinear gravitational evolution of the primordial Gaussian field (§3). Next we discuss the spatial biasing of galaxies relative to the underlying dark matter distribution in §4. Our understanding of biasing is still far from complete, and its description is necessarily empirical and very approximate. Nevertheless this is one of the most important ingredients for proper interpretation of galaxy redshift surveys. Section 5 introduces general relativistic effects which become important especially for galaxies at high redshifts. We present the latest results from the two currently largest galaxy redshift surveys, 2dF (Two Degree Field) and SDSS (Sloan Digital Sky Survey), in §6. Finally §7 is devoted to summary of the present knowledge of our universe and our personal view of the future direction of cosmological researches in the new millennium.

## 2 Clustering in the expanding universe

### 2.1 The cosmological principle

Our current universe exhibits a wealth of nonlinear structures, but the zero-th order description of our universe is based on the assumption that the universe is homogeneous and isotropic smoothed over sufficiently large scales. This statement is usually referred to as *the cosmological principle*. In fact, the cosmological principle was first adopted when observational cosmology was in its infancy; it was then little more than a conjecture, embodying 'Occam's razor' for the simplest possible model.

Rudnicki (1995) [67] summarized various forms of cosmological principles in modern-day language, which were stated over different periods in human history based on philosophical and aesthetic considerations rather than on fundamental physical laws.

**(i) The ancient Indian cosmological principle:**

*The Universe is infinite in space and time and is infinitely heterogeneous.*

**(ii) The ancient Greek cosmological principle:**

*Our Earth is the natural center of the Universe.*

**(iii) The Copernican cosmological principle:**

*The Universe as observed from any planet looks much the same.*

**(iv) The (generalized) cosmological principle:**

*The Universe is (roughly) homogeneous and isotropic.*

**(v) The perfect cosmological principle:**

*The Universe is (roughly) homogeneous in space and time, and is isotropic in space.*

**(vi) The anthropic principle:**

*A human being, as he/she is, can exist only in the Universe as it is.*

We note that the ancient Indian principle may be viewed as a sort of 'fractal model'. The perfect cosmological principle led to the steady state model, which although more symmetric than the (generalized) cosmological principle, was rejected on observational grounds. The anthropic principle is becoming popular again, e.g. in 'explaining' the non-zero value of the cosmological constant.

Like with any other idea about the physical world, we cannot prove a model, but only falsify it. Proving the homogeneity of the Universe is in particular difficult as we observe the Universe from one point in space, and we can only deduce isotropy directly. The practical methodology we adopt is to assume homogeneity and to assess the level of fluctuations relative to the mean, and hence to test for

consistency with the underlying hypothesis. If the assumption of homogeneity turns out to be wrong, then there are numerous possibilities for inhomogeneous models, and each of them must be tested against the observations.

For that purpose, one needs observational data with good quality and quality extending up to high redshifts. Let us mention some of those.

**The CMB Fluctuations** Ehlers, Garen and Sachs (1968) [18] showed that by combining the CMB isotropy with the Copernican principle one can deduce homogeneity. More formally their theorem (based on the Liouville theorem) states that “If the fundamental observers in a dust space-time see an isotropic radiation field, then the space-time is locally given by the Friedman-Robertson-Walker (FRW) metric”. The COBE (COsmic Background Explorer) measurements of temperature fluctuations  $\Delta T/T = 10^{-5}$  on scales of  $10^\circ$  give via the Sachs Wolfe effect ( $\Delta T/T = \frac{1}{3}\Delta\phi/c^2$ ) and Poisson equation rms density fluctuations of  $\frac{\delta\rho}{\rho} \sim 10^{-4}$  on  $1000 h^{-1} \text{Mpc}$  (e.g. [83]), i.e. the deviations from a smooth Universe are tiny.

**Galaxy Redshift Surveys** The distribution of galaxies in local redshift surveys is highly clumpy, with the Supergalactic Plane seen in full glory. However, deeper surveys like 2dF and SDSS (see §6) show that the fluctuations decline as the length-scales increase. Peebles (1993) [63] has shown that the angular correlation functions for the Lick and APM (Automatic Plate Measuring) surveys scale with magnitude as expected in a universe which approaches homogeneity on large scales. While redshift surveys can provide interesting estimates of the fluctuations on intermediate scales (e.g. [66]), the problems of biasing, evolution and  $K$ -correction, would limit the ability of those redshift surveys to ‘prove’ the Cosmological Principle. Despite these worries the measurement of the power spectrum of galaxies derived on the assumption of an underlying FRW metric shows good agreement the  $\Lambda$ -CDM (cold dark matter) model fitted to the CMB.

**Radio Sources** Radio sources in surveys have typical median redshift  $\bar{z} \sim 1$ , and hence are useful probes of clustering at high redshift. Unfortunately, it is difficult to obtain distance information from these surveys: the radio luminosity function is very broad, and it is difficult to measure optical redshifts of distant radio sources. Earlier studies claimed that the distribution of radio sources supports the ‘Cosmological Principle’. However, the wide range in intrinsic luminosities of radio sources would dilute any clustering when projected on the sky. Recent analyses of new deep radio surveys suggest that radio sources are actually clustered at least as strongly as local optical galaxies. Nevertheless, on the very large scales the distribution of radio sources seems nearly isotropic.

**The XRB** The X-ray Background (XRB) is likely to be due to sources at high redshift. The XRB sources are probably located at redshift  $z < 5$ , making

them convenient tracers of the mass distribution on scales intermediate between those in the CMB as probed by COBE, and those probed by optical and IRAS redshift surveys. The interpretation of the results depends somewhat on the nature of the X-ray sources and their evolution. By comparing the predicted multipoles to those observed by HEAO1, Scharf et al. (2000) [69] estimate the amplitude of fluctuations for an assumed shape of the density fluctuations. The observed fluctuations in the XRB are roughly as expected from interpolating between the local galaxy surveys and the COBE and other CMB experiments. The rms fluctuations  $\frac{\delta\rho}{\rho}$  on a scale of  $\sim 600h^{-1}\text{Mpc}$  are less than 0.2 %.

Since the (generalized) cosmological principle is now well supported by the above observations, we shall assume below that it holds over scales  $l > 100h^{-1}\text{Mpc}$ .

The rest of the current section is devoted to a brief review of the homogeneous and isotropic cosmological model. Further details may be easily found in standard cosmology textbooks [82, 56, 63, 58, 10, 57].

The cosmological principle is mathematically paraphrased as that the metric of the universe (in its zero-th order approximation) is given by

$$ds^2 = -dt^2 + a(t)^2 \left( \frac{dx^2}{1 - Kx^2} + x^2 d\theta^2 + x^2 \sin^2\theta d\phi^2 \right), \quad (1)$$

where  $x$  is the comoving coordinate, and we use the units in which the light velocity  $c = 1$ . The above Robertson – Walker metric is specified by a constant  $K$ , the spatial curvature, and a function of time  $a(t)$ , the scale factor.

The homogeneous and isotropic assumption also implies that the energy momentum tensor of the matter field,  $T_{\mu\nu}$ , should take the form of the ideal fluid:

$$T_{\mu\nu} = (\rho + p)u_\mu u_\nu + p g_{\mu\nu}, \quad (2)$$

where  $u_\mu$  is the 4-velocity of the matter,  $\rho$  is the mean energy density, and  $p$  is the mean pressure.

## 2.2 From the Einstein equation to the Friedmann equation

The next task is to write down the Einstein equation:

$$R_{\mu\nu} - \frac{1}{2}R g_{\mu\nu} + \Lambda g_{\mu\nu} = 8\pi G T_{\mu\nu} \quad (3)$$

using equations (1) and (2). In this case one is left with the following two independent equations:

$$\left( \frac{1}{a} \frac{da}{dt} \right)^2 = \frac{8\pi G}{3} \rho - \frac{K}{a^2} + \frac{\Lambda}{3}, \quad (4)$$

$$\frac{1}{a} \frac{d^2 a}{dt^2} = -\frac{4\pi G}{3}(\rho + 3p) + \frac{\Lambda}{3}, \quad (5)$$

for the three independent functions,  $a(t)$ ,  $\rho(t)$ , and  $p(t)$ .

Differentiation of equation (4) with respect to  $t$  yields

$$\frac{\ddot{a}}{a} = \frac{4\pi G}{3} \left( \dot{\rho} \frac{a}{\dot{a}} + 2\rho \right) + \frac{\Lambda}{3}. \quad (6)$$

Then eliminating  $\ddot{a}$  with equation (5), one obtains

$$\dot{\rho} = -3 \frac{\dot{a}}{a}(\rho + p). \quad (7)$$

This can be easily interpreted as the 1st law of the thermodynamics  $dQ = dU - pdV = d(\rho a^3) - pd(a^3) = 0$  in the present context. Equations (4) and (7) are often used as the two independent basic equations for  $a(t)$ , instead of equations (4) and (5).

In either case, however, one needs another independent equation to solve for  $a(t)$ . This is usually given by the equation of state of the form  $p = p(\rho)$ . In cosmology, the following simple relation:

$$p = w\rho. \quad (8)$$

While the value of  $w$  may change as redshift in principle, it is often assumed that  $w$  is independent of time just for simplicity. Then substituting this equation of state into equation (7) immediately yields

$$\rho \propto a^{-3(1+w)}. \quad (9)$$

The non-relativistic matter (or dust), ultra-relativistic matter (or radiation), and the cosmological constant correspond to  $w = 0$ ,  $1/3$ , and  $-1$ , respectively.

If the universe consists of different fluid species with  $w_i$  ( $i = 1, \dots, N$ ), equation (9) still holds independently as long as they do not interact with each other. If one denotes the present energy density of the  $i$ -th component by  $\rho_{i,0}$ , then the total energy density of the universe at the epoch corresponding to the scale factor of  $a(t)$  is given by

$$\rho = \sum_{i=1}^N \frac{\rho_{i,0}}{a^{3(1+w_i)}}, \quad (10)$$

where the present value of the scale factor,  $a_0$ , is set to be unity without loss of generality. Thus, equation (4) becomes

$$\left( \frac{1}{a} \frac{da}{dt} \right)^2 = \frac{8\pi G}{3} \sum_{i=1}^N \frac{\rho_{i,0}}{a^{3(1+w_i)}} - \frac{K}{a^2} + \frac{\Lambda}{3}. \quad (11)$$

Note that those components with  $w_i = -1$  may be equivalent to the conventional cosmological constant  $\Lambda$  at this level, although they may exhibit spatial variation unlike  $\Lambda$ .

Evaluating equation (11) at the present epoch, one finds

$$H_0^2 = \frac{8\pi G}{3} \sum_{i=1}^N \rho_{i,0} - K + \frac{\Lambda}{3}, \quad (12)$$

where  $H_0$  is the Hubble constant at the present epoch. The above equation is usually rewritten as follows:

$$K \equiv H_0^2 \Omega_K = H_0^2 \left( \sum_{i=1}^N \Omega_{i,0} + \Omega_\Lambda - 1 \right), \quad (13)$$

where the density parameter for the  $i$ -th component is defined as

$$\Omega_{i,0} \equiv \frac{8\pi G}{3H_0^2} \rho_{i,0}, \quad (14)$$

and similarly the dimensionless cosmological constant is

$$\Omega_\Lambda \equiv \frac{\Lambda}{3H_0^2}. \quad (15)$$

Incidentally equation (13) clearly illustrates the Mach principle in the sense that the space curvature is simply determined by the amount of matter components in the universe. In particular, the flat universe ( $K = 0$ ) implies that the sum of the density parameters is unity:

$$\sum_{i=1}^N \Omega_{i,0} + \Omega_\Lambda = 1. \quad (16)$$

Finally the cosmic expansion is described by

$$\left( \frac{da}{dt} \right)^2 = H_0^2 \left( \sum_{i=1}^N \frac{\Omega_{i,0}}{a^{1+3w_i}} + 1 - \sum_{i=1}^N \Omega_{i,0} - \Omega_\Lambda + \Omega_\Lambda a^2 \right). \quad (17)$$

As will be shown below, the present universe is supposed to be dominated by non-relativistic matter (baryons and collisionless dark matter) and the cosmological constant. So in the present review, we approximate equation (17) as

$$\left( \frac{da}{dt} \right)^2 = H_0^2 \left( \frac{\Omega_m}{a} + 1 - \Omega_m - \Omega_\Lambda + \Omega_\Lambda a^2 \right) \quad (18)$$

unless otherwise stated.

### 2.3 Expansion law and age of the universe

Equation (18) has the following analytic solutions in several simple but practically important cases.

(a) Einstein – de Sitter model ( $\Omega_m = 1, \Omega_\Lambda = 0$ )

$$a(t) = \left( \frac{t}{t_0} \right)^{2/3}, \quad t_0 = \frac{2}{3H_0} \quad (19)$$

(b) Open model with vanishing cosmological constant ( $\Omega_m < 1, \Omega_\Lambda = 0$ )

$$a = \frac{\Omega_m}{2(1 - \Omega_m)} (\cosh \theta - 1), \quad H_0 t = \frac{\Omega_m}{2(1 - \Omega_m)^{3/2}} (\sinh \theta - \theta) \quad (20)$$

$$H_0 t_0 = \frac{1}{1 - \Omega_m} - \frac{\Omega_m}{2(1 - \Omega_m)^{3/2}} \ln \frac{2 - \Omega_m + 2\sqrt{1 - \Omega_m}}{\Omega_m} \quad (21)$$

(c) Spatially-flat model with cosmological constant ( $\Omega_m < 1, \Omega_\Lambda = 1 - \Omega_m$ )

$$a(t) = \left( \frac{\Omega_m}{1 - \Omega_m} \right)^{1/3} \left[ \sinh \frac{3\sqrt{1 - \Omega_m}}{2} H_0 t \right]^{2/3}, \quad (22)$$

$$H_0 t_0 = \frac{1}{3\sqrt{1 - \Omega_m}} \ln \frac{2 - \Omega_m + 2\sqrt{1 - \Omega_m}}{\Omega_m} \quad (23)$$

In the above,  $t_0$  denotes the present age of the universe:

$$t_0 = \frac{1}{H_0} \int_0^1 \frac{x \, dx}{\sqrt{\Omega_m x + (1 - \Omega_m - \Omega_\Lambda)x^2 + \Omega_\Lambda x^4}}, \quad (24)$$

and we adopt the initial condition that  $a = 0$  at  $t = 0$ . The expression clearly indicates that  $t_0$  increases as  $\Omega_m$  decreases and/or  $\Omega_\Lambda$  increases. Figure 1 plots the scale factor as a function of  $H_0(t - t_0)$ , and Table 1 summarizes the age of the universe.

Table 1: The present age of the universe [ $h_{70}^{-1}$  Gyr].

$\Omega_m$	Open model ( $\Omega_\Lambda = 0$ )	Spatially-flat model ( $\Omega_\Lambda = 1 - \Omega_m$ )
1.0	9.3	9.3
0.5	10.5	11.6
0.3	11.3	13.5
0.1	12.5	17.8
0.01	13.9	28.0

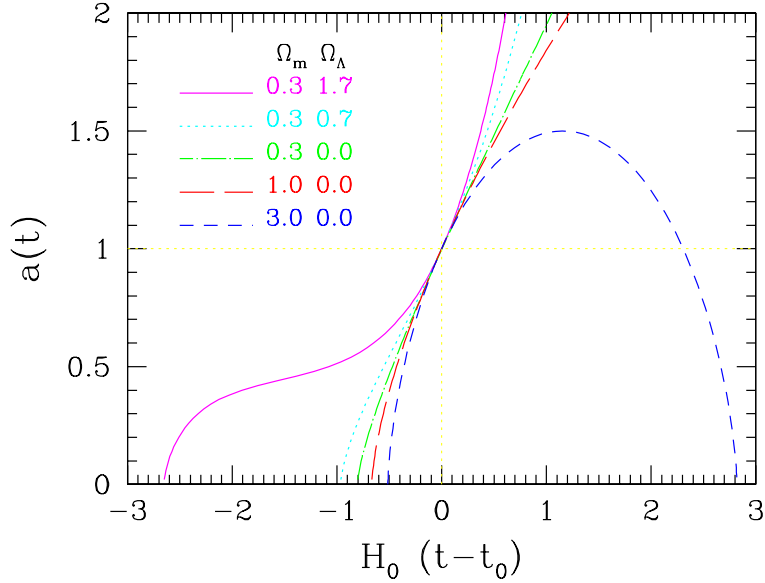


Figure 1: Evolution of the cosmic scale factor as a function of  $H_0(t - t_0)$ . The present value of the scale factor  $a_0$  is set to unity; solid line:  $(\Omega_m, \Omega_\Lambda) = (0.3, 1.7)$ , dotted line:  $(0.3, 0.7)$ , dot-dashed line:  $(0.3, 0.0)$ , long dashed line:  $(1.0, 0.0)$ , short dashed line:  $(3.0, 0.0)$ .

## 2.4 Einstein's static model and Lemaître's model

So far we have shown that solutions of the Einstein equation are *dynamical* in general, i.e., the scale factor  $a$  is time-dependent. As a digression, let us examine why Einstein once introduced the  $\Lambda$ -term to obtain a static cosmological solution. This is mainly important for historical reasons, but also is interesting to observe how the operationally identical parameter (the  $\Lambda$ -term, the cosmological constant, the vacuum energy, the dark energy) shows up in completely different contexts in the course of the development of cosmological physics.

Consider first the case of  $\Lambda = 0$  in equations (4) and (5). Clearly the necessary and sufficient condition that the equations admit the solution of  $a = \text{const.}$  is given by

$$\rho = -3p = \frac{3K}{8\pi Ga^2}. \quad (25)$$

Namely, any static model requires that the universe is dominated by matter with either negative pressure or negative density which is physically unacceptable. If

$\Lambda \neq 0$  on the other hand, the condition for the static solution is

$$K = 4\pi G(\rho + p)a^2, \quad \Lambda = 4\pi G(\rho + 3p), \quad (26)$$

yielding

$$\rho = \frac{1}{8\pi G} \left( \frac{3K}{a^2} - \Lambda \right), \quad p = \frac{1}{8\pi G} \left( \Lambda - \frac{K}{a^2} \right). \quad (27)$$

Thus both  $\rho$  and  $p$  can be positive if

$$\frac{K}{a^2} \leq \Lambda \leq \frac{3K}{a^2}. \quad (28)$$

In particular, if  $p = 0$ ,

$$\rho = \frac{\Lambda}{4\pi G}, \quad K = \Lambda a^2. \quad (29)$$

This represents the closed universe (with positive spatial curvature), and corresponds to Einstein's static model.

The above static model is a special case of Lemaître's universe model with  $\Lambda > 0$  and  $K > 0$ . For simplicity, let us assume that the universe is dominated by non-relativistic matter with negligible pressure, and consider the behavior of Lemaître's model. First define the values of the density and the scale factor corresponding to Einstein's static model:

$$\rho_E = \frac{\Lambda}{4\pi G}, \quad K = \Lambda a_E^2. \quad (30)$$

Suppose the model in which the density at  $a = a_E$  is a factor of  $\alpha (> 1)$  larger than  $\rho_E$ . Then

$$\rho = \alpha \rho_E \left( \frac{a_E}{a} \right)^3 = \frac{\alpha \Lambda}{4\pi G} \left( \frac{a_E}{a} \right)^3, \quad (31)$$

and equations (4) and (5) reduce to

$$\dot{a}^2 = \frac{\Lambda}{3} \left( \frac{2\alpha a_E^3}{a} - 3a_E^2 + a^2 \right), \quad (32)$$

$$\frac{\ddot{a}}{a} = \frac{\Lambda}{3} \left[ 1 - \alpha \left( \frac{a_E}{a} \right)^3 \right]. \quad (33)$$

For the period of  $a \ll a_E$ , equation (32) indicates that  $a \propto t^{2/3}$  and the universe is decelerating ( $\ddot{a} < 0$ ). When  $a$  reaches  $\alpha^{1/3} a_E$ ,  $\dot{a}^2$  takes the minimum value  $\Lambda a_E^2 (\alpha^{2/3} - 1)$  and the universe becomes accelerating ( $\ddot{a} > 0$ ). Finally the universe approaches the exponential expansion or de Sitter model:  $a \propto \exp(t\sqrt{\Lambda/3})$ . If  $\alpha$  becomes closer to unity, the minimum value reaches zero

and the expansion of the universe is effectively frozen. This phase is called the coasting period, and the case with  $\alpha = 1$  corresponds to Einstein's static model in which the coasting period continues forever. A similar consideration for  $\alpha < 1$  indicates that the universe starts collapsing ( $\dot{a}^2 = 0$ ) before  $\ddot{a} = 0$ . Thus the behavior of Lemaître's model is crucially different if  $\alpha$  is larger or smaller than unity. This suggests that Einstein's static model ( $\alpha = 1$ ) is unstable.

## 2.5 Vacuum energy as an effective cosmological constant

So far we discussed the cosmological constant introduced in the l.h.s. of the Einstein equation. Formally one can move the  $\Lambda$ -term to the r.h.s. by assigning

$$\rho_\Lambda = \frac{\Lambda}{8\pi G}, \quad p_\Lambda = -\frac{\Lambda}{8\pi G}. \quad (34)$$

This *effective* matter field, however, should satisfies an equation of state of  $p = -\rho$ . Actually the following example presents a specific example for an *effective* cosmological constant. Consider a real scalar field whose Lagrangian density is given by

$$\mathcal{L} = \frac{1}{2}g_{\mu\nu}\partial^\mu\phi\partial^\nu\phi - V(\phi). \quad (35)$$

Its energy-momentum tensor is

$$T_{\mu\nu} = \partial_\mu\phi\partial_\nu\phi - \mathcal{L}g_{\mu\nu}, \quad (36)$$

and if the field is spatially homogeneous, its energy density and pressure are

$$\rho_\phi = \frac{1}{2}\dot{\phi}^2 + V(\phi), \quad p_\phi = \frac{1}{2}\dot{\phi}^2 - V(\phi). \quad (37)$$

Clearly if the evolution of the field is negligible, i.e.,  $\dot{\phi}^2 \ll V(\phi)$ ,  $p_\phi \approx -\rho_\phi$  and the field acts as a cosmological constant. Of course this model is one of the simplest examples, and one may play with much more complicated models if needed.

If the  $\Lambda$ -term is introduced in the l.h.s., its should be constant to satisfy the energy-momentum conservation  $T_{\mu\nu}{}^{\nu} = 0$ . Once it is regarded as a sort of matter field in the r.h.s, however, it does not have to be constant. In fact, the above example shows that the equation of state for the field has  $w = -1$  only in special cases. This is why recent literature refers to the field as *dark energy* instead of the cosmological constant.

## 2.6 Gravitational instability

We have presented the zero-th order description of the universe neglecting the inhomogeneity or spatial variation of matter inside. Now we are in a position to consider the evolution of matter in the universe. For simplicity we focus on

the non-relativistic regime where Newtonian approximation is valid. Then the basic equations for the self-gravitating fluid are given by the continuity equation, Euler's equation and the Poisson equation:

$$\frac{\partial \rho}{\partial t} + \nabla \cdot (\rho \mathbf{u}) = 0, \quad (38)$$

$$\frac{\partial \mathbf{u}}{\partial t} + (\mathbf{u} \cdot \nabla) \mathbf{u} = -\frac{1}{\rho} \nabla p - \nabla \Phi, \quad (39)$$

$$\nabla^2 \Phi = 4\pi G \rho. \quad (40)$$

We would like to rewrite those equations in the comoving frame. For this purpose, we introduce the position  $\mathbf{x}$  in the comoving coordinate, the peculiar velocity,  $\mathbf{v}$ , density fluctuations  $\delta(t, \mathbf{x})$ , and the gravitational potential  $\phi(t, \mathbf{x})$  which are defined respectively as

$$\mathbf{x} = \frac{\mathbf{r}}{a(t)}, \quad (41)$$

$$\mathbf{v} = a(t) \dot{\mathbf{x}}, \quad (42)$$

$$\delta(t, \mathbf{x}) = \frac{\rho(t, \mathbf{x})}{\bar{\rho}(t)} - 1, \quad (43)$$

$$\phi(t, \mathbf{x}) = \Phi + \frac{1}{2} a \ddot{a} |\mathbf{x}|^2. \quad (44)$$

Then equations (38) to (40) reduce to

$$\dot{\delta} + \frac{1}{a} \nabla \cdot [(1 + \delta) \mathbf{v}] = 0, \quad (45)$$

$$\dot{\mathbf{v}} + \frac{1}{a} (\mathbf{v} \cdot \nabla) \mathbf{v} + \frac{\dot{a}}{a} \mathbf{v} = -\frac{1}{\rho a} \nabla p - \frac{1}{a} \nabla \phi, \quad (46)$$

$$\nabla^2 \phi = 4\pi G \bar{\rho} a^2 \delta, \quad (47)$$

where the dot and  $\nabla$  in the above equations are the time derivative for a given  $\mathbf{x}$  and the spatial derivative with respect to  $\mathbf{x}$ , i.e., defined in the comoving coordinate (while those in eqs.[38] to [40] are defined in the proper coordinate).

A standard picture of the cosmic structure formation assumes that the initially tiny amplitude of density fluctuation grow according to equations (45) to (47). Also the universe smoothed over large scales approaches a homogeneous model. Thus at early epochs and/or on large scales, the nonlinear effect is small and one can linearize those equations with respect to  $\delta$  and  $\mathbf{v}$ :

$$\dot{\delta} + \frac{1}{a} \nabla \cdot \mathbf{v} = 0, \quad (48)$$

$$\dot{\mathbf{v}} + \frac{\dot{a}}{a} \mathbf{v} = -\frac{c_s^2}{a} \nabla \delta - \frac{1}{a} \nabla \phi, \quad (49)$$

$$\nabla^2 \phi = 4\pi G \bar{\rho} a^2 \delta, \quad (50)$$

where  $c_s^2 \equiv (\partial p / \partial \rho)$  is the sound velocity.

As usual, we transform the above equations in  $\mathbf{k}$  space using

$$\delta_{\mathbf{k}}(t) \equiv \frac{1}{V} \int \delta(t, \mathbf{x}) \exp(i\mathbf{k} \cdot \mathbf{x}) d\mathbf{x}. \quad (51)$$

Then the equation for  $\delta_{\mathbf{k}}$  reduces to

$$\ddot{\delta}_{\mathbf{k}} + 2\frac{\dot{a}}{a}\dot{\delta}_{\mathbf{k}} + \left(\frac{c_s^2 k^2}{a^2} - 4\pi G \bar{\rho}\right) \delta_{\mathbf{k}} = 0. \quad (52)$$

If the signature of the third term is positive,  $\delta_{\mathbf{k}}$  has an unstable, or, monotonically increasing solution. This condition is equivalent to *the Jeans criterion*:

$$\lambda \equiv \frac{2\pi}{k} > \lambda_J \equiv c_s \sqrt{\frac{\pi}{G\bar{\rho}}}, \quad (53)$$

namely, the wavelength of the fluctuation is larger than the Jeans length  $\lambda_J$  which characterizes the scale that the sound wave can propagate within the dynamical time of the fluctuation  $\sqrt{\pi/G\bar{\rho}}$ . Below the scale the pressure wave can suppress the gravitational instability, and the fluctuation amplitude oscillates.

## 2.7 Linear growth rate of the density fluctuation

Most likely our universe is dominated by collisionless dark matter, and thus  $\lambda_J$  is negligibly small. Thus at most scales of cosmological interest, equation (53) is well approximated as

$$\ddot{\delta}_{\mathbf{k}} + 2\frac{\dot{a}}{a}\dot{\delta}_{\mathbf{k}} - 4\pi G \bar{\rho} \delta_{\mathbf{k}} = 0. \quad (54)$$

For a given set of cosmological parameters, one can solve the above equation by substituting the expansion law for  $a(t)$  as described in §2.3. Since equation (54) is the second-order differential equation with respect to  $t$ , there are two independent solutions; a decaying mode and a growing mode which monotonically decreases and increases as  $t$ , respectively. The former mode becomes negligibly small as the universe expands, and thus one is usually interested in the growing mode alone.

More specifically those solutions are explicitly obtained as follows. First note that the l.h.s. of equation (18) is the Hubble parameter at  $t$ ,  $H(t) = \dot{a}/a$ :

$$H^2 = H_0^2 \left( \frac{\Omega_m}{a^3} + \frac{1 - \Omega_m - \Omega_\Lambda}{a^2} + \Omega_\Lambda \right) \quad (55)$$

$$= H_0^2 [\Omega_m(1+z)^3 + (1 - \Omega_m - \Omega_\Lambda)(1+z)^2 + \Omega_\Lambda]. \quad (56)$$

The first and second differentiation of equation (55) with respect to  $t$  yields

$$2H\dot{H} = H_0^2 \left( -3\frac{\Omega_m}{a^3} - 2\frac{1 - \Omega_m - \Omega_\Lambda}{a^2} \right) H. \quad (57)$$

and

$$\ddot{H} = H_0^2 \left( 9 \frac{\Omega_m}{2a^3} + 2 \frac{1 - \Omega_m - \Omega_\Lambda}{a^2} \right) H. \quad (58)$$

Thus the differential equation for  $H$  reduces to

$$\ddot{H} + 2H\dot{H} = H_0^2 H \frac{3\Omega_m}{2a^3} = 4\pi G \bar{\rho} H. \quad (59)$$

This coincides with the linear perturbation equation for  $\delta_{\mathbf{k}}$  (eq.[54]). Since  $H(t)$  is a decreasing function of  $t$ , this implies that  $H(t)$  is the decaying solution for equation (54). Then the corresponding growing solution  $D(t)$  can be obtained according to the standard procedure: subtracting equation (54) from equation (59) yields

$$a^2 \frac{d}{dt}(\dot{D}H - D\dot{H}) + \frac{da^2}{dt}(\dot{D}H - D\dot{H}) = \frac{d}{dt} \left[ a^2 H^2 \frac{d}{dt} \left( \frac{D}{H} \right) \right] = 0, \quad (60)$$

and therefore the formal expression for the growing solution in linear theory is

$$D(t) \propto H(t) \int \frac{dt}{a^2 H^2(t)}. \quad (61)$$

It is often more useful to rewrite  $D(t)$  in terms of the redshift  $z$  as follows:

$$D(z) = \frac{5\Omega_m H_0^2}{2} H(z) \int_z^\infty \frac{1+z'}{H^3(z')} dz', \quad (62)$$

where the proportional factor is chosen so as to reproduce  $D(z) \rightarrow 1/(1+z)$  for  $z \rightarrow \infty$ . Linear growth rates for the models described in §2.3 are summarized below.

(a) Einstein – de Sitter model ( $\Omega_m = 1, \Omega_\Lambda = 0$ )

$$D(z) = \frac{1}{1+z} \quad (63)$$

(b) Open model with vanishing cosmological constant ( $\Omega_m < 1, \Omega_\Lambda = 0$ )

$$D(z) \propto 1 + \frac{3}{x} + 3 \sqrt{\frac{1+x}{x^3}} \ln(\sqrt{1+x} - \sqrt{x}), \quad x \equiv \frac{1 - \Omega_m}{\Omega_m(1+z)} \quad (64)$$

(c) Spatially-flat model with cosmological constant ( $\Omega_m < 1, \Omega_\Lambda = 1 - \Omega_m$ )

$$D(z) \propto \sqrt{1 + \frac{2}{x^3}} \int_0^x \left( \frac{u}{2+u^3} \right)^{3/2} du, \quad x \equiv \frac{2^{1/3}(\Omega_m^{-1} - 1)^{1/3}}{1+z}. \quad (65)$$

For most purposes, the following fitting formulae [59] provide sufficiently accurate approximations.

$$D(z) = \frac{g(z)}{1+z}, \quad (66)$$

$$g(z) = \frac{5\Omega(z)}{2} \frac{1}{\Omega^{4/7}(z) - \lambda(z) + [1 + \Omega(z)/2][1 + \lambda(z)/70]}, \quad (67)$$

where

$$\Omega(z) = \Omega_m(1+z)^3 \left[ \frac{H_0}{H(z)} \right]^2 = \frac{\Omega_m(1+z)^3}{\Omega_m(1+z)^3 + (1 - \Omega_m - \Omega_\Lambda)(1+z)^2 + \Omega_\Lambda}, \quad (68)$$

$$\lambda(z) = \Omega_\Lambda \left[ \frac{H_0}{H(z)} \right]^2 = \frac{\Omega_\Lambda}{\Omega_m(1+z)^3 + (1 - \Omega_m - \Omega_\Lambda)(1+z)^2 + \Omega_\Lambda}. \quad (69)$$

Note that  $\Omega_m$  and  $\Omega_\Lambda$  refer to the *present* values of the density parameter and the dimensionless cosmological constant, respectively, which will be frequently used in the rest of the review.

Figure 2 shows the comparison of the numerically computed growth rate (thick lines) against the above fitting formulae (thin lines) which are practically indistinguishable.

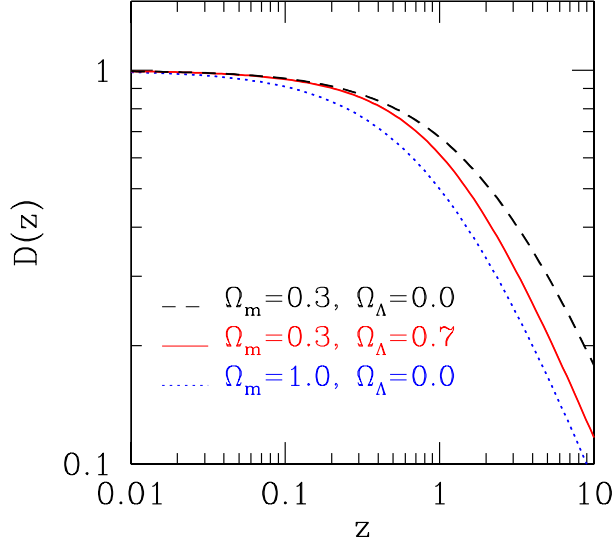


Figure 2: Linear growth rate of density fluctuations.

### 3 Statistics of cosmological density fluctuations

#### 3.1 Gaussian random field

Consider the density contrast  $\delta_i \equiv \delta(\mathbf{x}_i) = \rho(\mathbf{x})/\bar{\rho} - 1$  defined at the comoving position  $\mathbf{x}_i$ . The density field is regarded as a stochastic variable, and thus forms a random field. The conventional assumption is that the primordial density field (in its linear regime) is Gaussian, i.e., its  $m$ -point joint probability distribution obeys the multi-variate Gaussian:

$$P(\delta_1, \delta_2, \dots, \delta_m) d\delta_1 d\delta_2 \cdots d\delta_m = \frac{1}{\sqrt{(2\pi)^m \det(M)}} \exp \left[ \sum_{i,j=1}^m \frac{1}{2} \delta_i (M^{-1})_{ij} \delta_j \right] d\delta_1 d\delta_2 \cdots d\delta_m, \quad (70)$$

for an arbitrary positive integer  $m$ . Here  $M_{ij} \equiv \langle \delta_i \delta_j \rangle$  is the covariance matrix, and  $M^{-1}$  is its inverse. Since  $M_{ij} = \xi(\mathbf{x}_i, \mathbf{x}_j)$ , equation (70) implies that the statistical nature of the Gaussian density field is completely specified by the two-point correlation function  $\xi$  and its linear combination (including its derivative and integral). For an extensive discussion of the cosmological Gaussian density field, see ref. [4].

The Gaussian nature of the primordial density field is preserved in its linear evolution stage, but this is not the case in nonlinear stage. This is clear even from the definition of the Gaussian distribution: equation (70) formally assumes that the density contrast distributes symmetrically in the range of  $-\infty < \delta_i < \infty$ , but in the real density field  $\delta_i$  cannot be less than  $-1$ . This assumption does not make any practical difference as long as the fluctuations are (infinitesimally) small, but is invalid in nonlinear regime where the typical amplitude of the fluctuations exceeds unity.

In describing linear theory of cosmological density fluctuations, the Fourier transform of the spatial density contrast  $\delta(\mathbf{x}) \equiv \rho(\mathbf{x})/\langle \bar{\rho} \rangle - 1$  is the most basic variable:

$$\delta_{\mathbf{k}} = \frac{1}{V} \int d\mathbf{x} \delta(\mathbf{x}) \exp(i\mathbf{k} \cdot \mathbf{x}). \quad (71)$$

Since  $\delta_{\mathbf{k}}$  is a complex variable, it is decomposed by a set of two real variables, the amplitude  $D_{\mathbf{k}}$  and the phase  $\phi_{\mathbf{k}}$ :

$$\delta_{\mathbf{k}} \equiv D_{\mathbf{k}} \exp(i\phi_{\mathbf{k}}). \quad (72)$$

Then linear perturbation equation reads

$$\ddot{D}_{\mathbf{k}} + 2\frac{\dot{a}}{a}\dot{D}_{\mathbf{k}} - (4\pi G\bar{\rho} + \dot{\phi}^2)D_{\mathbf{k}} = 0, \quad (73)$$

$$\ddot{\phi}_{\mathbf{k}} + 2 \left( \frac{\dot{a}}{a} + \frac{\dot{D}_{\mathbf{k}}}{D_{\mathbf{k}}} \right) \dot{\phi}_{\mathbf{k}} = 0. \quad (74)$$

Equation (74) yields  $\dot{\phi}(t) \propto a^{-2}(t)D_{\mathbf{k}}^{-2}(t)$ , and  $\phi(t)$  rapidly converges to a constant value. Thus  $D_{\mathbf{k}}$  evolves following the growing solution in linear theory.

The most popular statistic of clustering in the universe is the power spectrum of the density fluctuations:

$$P(t, \mathbf{k}) \equiv \langle |D_{\mathbf{k}}(t)|^2 \rangle \quad (75)$$

which measures the amplitude of the mode of the wavenumber  $\mathbf{k}$ . This is the Fourier transform of the two-point correlation function:

$$\xi(\mathbf{x}, t) = \frac{1}{8\pi^3} \int P(t, \mathbf{k}) \exp(-i\mathbf{k} \cdot \mathbf{x}) d\mathbf{k}. \quad (76)$$

If the density field is globally homogeneous and isotropic (i.e., no preferred position or direction), equation (76) reduces to

$$\xi(x, t) = \frac{1}{2\pi^2} \int_0^\infty P(t, k) \frac{\sin kx}{x} k dk. \quad (77)$$

Since the above expression obtained after the ensemble average,  $x$  does not denote an amplitude of the position vector, but a comoving wavelength  $2\pi/k$  corresponding to the wavenumber  $k = |\mathbf{k}|$ . It should be noted that neither the power spectrum or the two-point correlation function contains information for the phase  $\phi_{\mathbf{k}}$ . Thus in principle two clustering patterns may be completely different even if they have the identical two-point correlation functions. This implies the practical importance to describe the statistics of phases  $\phi_{\mathbf{k}}$  in addition to the amplitude  $D_{\mathbf{k}}$  of clustering.

In the Gaussian field, however, one can directly show that equation (70) reduces to the probability distribution function of  $\phi_{\mathbf{k}}$  and  $D_{\mathbf{k}}$  that are explicitly written as

$$P(|\delta_{\mathbf{k}}|, \phi_{\mathbf{k}}) d|\delta_{\mathbf{k}}| d\phi_{\mathbf{k}} = \frac{2|\delta_{\mathbf{k}}|}{P(k)} \exp\left(-\frac{|\delta_{\mathbf{k}}|^2}{P(k)}\right) d|\delta_{\mathbf{k}}| \frac{d\phi_{\mathbf{k}}}{2\pi}. \quad (78)$$

mutually independently of  $k$ . The phase distribution is uniform, and thus does not carry information. The above probability distribution function is also derived when the real and imaginary parts of the Fourier components  $\delta_{\mathbf{k}}$  are uncorrelated and Gaussian distributed (with the dispersion  $P(k)/2$ ) independently of  $\mathbf{k}$ . As is expected, the distribution function (78) is completely fixed if  $P(k)$  is specified. This rephrases the previous statement that the Gaussian field is completely specified by the two-point correlation function in real space.

### 3.2 Log-normal distribution

A probability distribution function (PDF) of the cosmological density fluctuations is the most fundamental statistic characterizing the large-scale structure

of the universe. As long as the density fluctuations are in the linear regime, their PDF remains Gaussian. Once they reach the nonlinear stage, however, their PDF significantly deviates from the initial Gaussian shape due to the strong non-linear mode-coupling and the non-locality of the gravitational dynamics. The functional form for the resulting PDFs in nonlinear regimes are not known exactly, and a variety of phenomenological models have been proposed [30, 68, 9, 22].

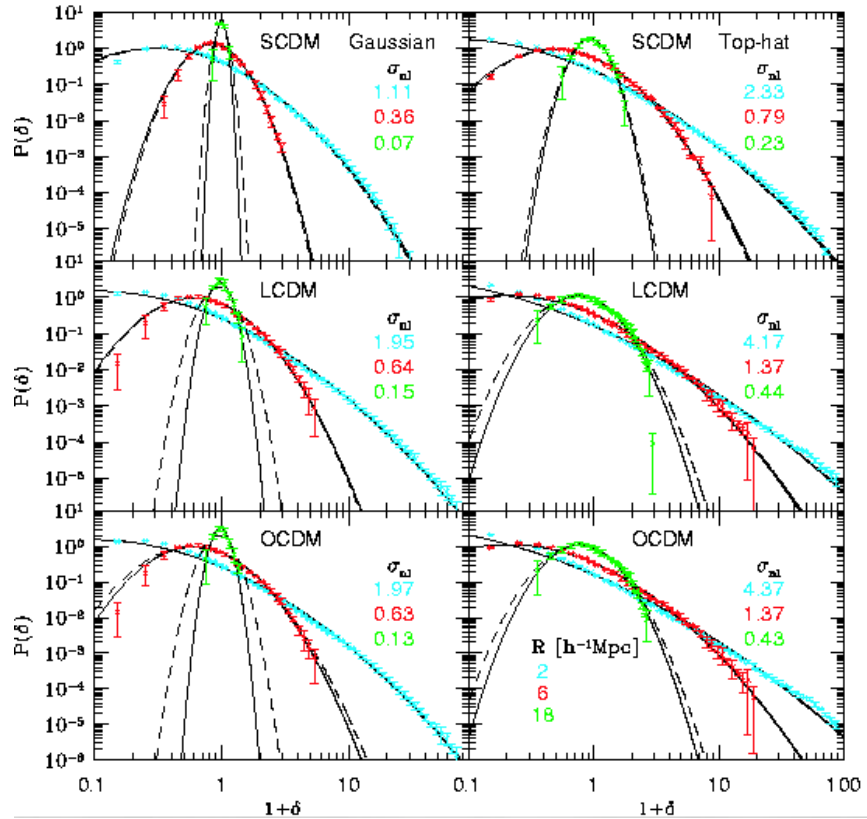


Figure 3: One-point PDFs in CDM models with Gaussian (left panels) and top-hat (right panels) smoothing windows;  $R = 2h^{-1}\text{Mpc}$  (cyan),  $6h^{-1}\text{Mpc}$  (red), and  $18h^{-1}\text{Mpc}$  (green). The *solid* and *long-dashed* lines represent the log-normal PDF adopting  $\sigma_{\text{nl}}$  calculated directly from the simulations and estimated from the nonlinear fitting formula of ref. [59], respectively. (ref. [35])

Kayo et al. (2001) [35] showed that the one-point log-normal PDF:

$$P_{\text{LN}}^{(1)}(\delta) = \frac{1}{\sqrt{2\pi\sigma_1^2}} \exp\left[-\frac{\{\ln(1+\delta) + \sigma_1^2/2\}^2}{2\sigma_1^2}\right] \frac{1}{1+\delta}. \quad (79)$$

describes very accurately the cosmological density distribution even in the non-linear regime (the rms variance  $\sigma_{\text{nl}} \lesssim 4$  and the over-density  $\delta \lesssim 100$ ). The above function is characterized by a single parameter  $\sigma_1$  which is related to the variance of  $\delta$ . Since we use  $\delta$  to represent the density fluctuation field smoothed over  $R$ , its variance is computed from its power spectrum  $P_{\text{nl}}$  explicitly as

$$\sigma_{\text{nl}}^2(R) \equiv \frac{1}{2\pi^2} \int_0^\infty P_{\text{nl}}(k) \tilde{W}^2(kR) k^2 dk. \quad (80)$$

Here we use subscripts “lin” and “nl” to distinguish the variables corresponding to the primordial (linear) and the evolved (nonlinear) density fields, respectively. Then  $\sigma_1$  depends on the smoothing scale  $R$  alone and is given by

$$\sigma_1^2(R) = \ln[1 + \sigma_{\text{nl}}^2(R)]. \quad (81)$$

Given a set of cosmological parameters, one can compute  $\sigma_{\text{nl}}(R)$  and thus  $\sigma_1(R)$  very accurately using a fitting formula for  $P_{\text{nl}}(k)$  (e.g., ref. [59]). In this sense, the above log-normal PDF is completely specified without any free parameter.

Figure 3 plots the one-point PDFs computed from cosmological N-body simulations in SCDM, LCDM and OCDM (for Standard, Lambda and Open CDM) models, respectively [31, 35]. The simulations employ  $N = 256^3$  dark matter particles in a periodic comoving cube ( $100h^{-1}\text{Mpc}$ )<sup>3</sup>. The density fields are smoothed over Gaussian (*Left panels*) and Top-hat (*Right panels*) windows with different smoothing lengths;  $R = 2h^{-1}\text{Mpc}$ ,  $6h^{-1}\text{Mpc}$  and  $18h^{-1}\text{Mpc}$ . Solid lines show the log-normal PDFs adopting the value of  $\sigma_{\text{nl}}$  directly evaluated from simulations (shown in each panel). The agreement between the log-normal model and the simulation results is quite impressive. A small deviation is noticeable only for  $\delta \lesssim -0.5$ .

From an empirical point of view, Hubble (1934) [30] first noted that the galaxy distribution in angular cells on the celestial sphere may be approximated by a log-normal distribution, rather than a Gaussian. Theoretically the above log-normal function may be obtained from the one-to-one mapping between the linear random-Gaussian and the nonlinear density fields [9]. Define a linear density field  $g$  smoothed over  $R$  obeying the Gaussian PDF:

$$P_{\text{G}}^{(1)}(g) = \frac{1}{\sqrt{2\pi\sigma_{\text{lin}}^2}} \exp\left(-\frac{g^2}{2\sigma_{\text{lin}}^2}\right), \quad (82)$$

where the variance is computed from its linear power spectrum:

$$\sigma_{\text{lin}}^2(R) \equiv \frac{1}{2\pi^2} \int_0^\infty P_{\text{lin}}(k) \tilde{W}^2(kR) k^2 dk. \quad (83)$$

If one introduces a new field  $\delta$  from  $g$  as

$$1 + \delta = \frac{1}{\sqrt{1 + \sigma_{\text{nl}}^2}} \exp \left\{ \frac{g}{\sigma_{\text{lin}}} \sqrt{\ln(1 + \sigma_{\text{nl}}^2)} \right\}, \quad (84)$$

the PDF for  $\delta$  is simply given by  $(dg/d\delta)P_{\text{G}}^{(1)}(g)$  which reduces to equation (79).

At this point, the transformation (84) is nothing but a mathematical procedure to relate the Gaussian and the log-normal functions. Thus there is no physical reason to believe that the new field  $\delta$  should be regarded as a nonlinear density field evolved from  $g$  even in an approximate sense. In fact it is physically unacceptable since the relation, if taken at face value, implies that the nonlinear density field is completely determined by its linear counterpart locally. We know, on the other hand, that the nonlinear gravitational evolution of cosmological density fluctuations proceeds in a quite nonlocal manner, and is sensitive to the surrounding mass distribution. Nevertheless the fact that the log-normal PDF provides a good fit to the simulation data empirically implies that the transformation (84) somehow captures an important aspect of the nonlinear evolution in the real universe.

### 3.3 Higher-order correlation functions

One of the most direct methods to evaluate the deviation from the Gaussianity is to compute the higher-order correlation functions. Suppose that  $x_i$  now labels the position of the  $i$ -th object (galaxy), and then the two-point correlation function  $\xi_{12} \equiv \xi(\mathbf{x}_1, \mathbf{x}_2)$  is defined also in terms of the joint probability as

$$\delta P_{12} = \bar{n}^2 \delta V_1 \delta V_2 [1 + \xi_{12}]. \quad (85)$$

This definition is generalized to three- and four-point correlation functions,  $\zeta_{123} \equiv \zeta(\mathbf{x}_1, \mathbf{x}_2, \mathbf{x}_3)$  and  $\eta_{1234} \equiv \eta(\mathbf{x}_1, \mathbf{x}_2, \mathbf{x}_3, \mathbf{x}_4)$ , in a straightforward manner:

$$\delta P_{123} = \bar{n}^3 \delta V_1 \delta V_2 \delta V_3 [1 + \xi_{12} + \xi_{23} + \xi_{31} + \zeta_{123}], \quad (86)$$

$$\begin{aligned} \delta P_{1234} = & \bar{n}^4 \delta V_1 \delta V_2 \delta V_3 \delta V_4 [1 + \xi_{12} + \xi_{13} + \xi_{14} + \xi_{23} + \xi_{24} + \xi_{34} \\ & + \zeta_{123} + \zeta_{124} + \zeta_{134} + \zeta_{234} \\ & + \xi_{12}\xi_{34} + \xi_{13}\xi_{24} + \xi_{14}\xi_{23} + \eta_{1234}], \end{aligned} \quad (87)$$

Apparently  $\xi_{12}$ ,  $\zeta_{123}$ , and  $\eta_{1234}$  are symmetric with respect to the change of the indices. Define the following quantities with the same symmetry properties:

$$Z_{123} \equiv \xi_{12}\xi_{23} + \xi_{21}\xi_{13} + \xi_{23}\xi_{31}, \quad (88)$$

$$\begin{aligned} A_{1234} \equiv & \xi_{12}\xi_{23}\xi_{34} + \xi_{23}\xi_{34}\xi_{41} + \xi_{24}\xi_{41}\xi_{12} + \xi_{13}\xi_{32}\xi_{24} + \xi_{32}\xi_{24}\xi_{41} \\ & + \xi_{24}\xi_{41}\xi_{13} + \xi_{12}\xi_{24}\xi_{43} + \xi_{24}\xi_{43}\xi_{31} + \xi_{31}\xi_{12}\xi_{24} + \xi_{13}\xi_{34}\xi_{42} \\ & + \xi_{34}\xi_{42}\xi_{21} + \xi_{42}\xi_{21}\xi_{13}, \end{aligned} \quad (89)$$

$$B_{1234} \equiv \xi_{12}\xi_{13}\xi_{14} + \xi_{21}\xi_{23}\xi_{24} + \xi_{31}\xi_{32}\xi_{34} + \xi_{41}\xi_{42}\xi_{43}, \quad (90)$$

$$C_{1234} \equiv \zeta_{123}(\xi_{14} + \xi_{24} + \xi_{34}) + \zeta_{134}(\xi_{12} + \xi_{32} + \xi_{42})$$

$$+ \zeta_{124}(\xi_{31} + \xi_{32} + \xi_{34}) + \zeta_{234}(\xi_{12} + \xi_{13} + \xi_{14}). \quad (91)$$

Then it is not unreasonable to suspect that the following relations hold

$$\zeta_{123} = Q Z_{123}, \quad (92)$$

$$\eta_{1234} = R_a A_{1234} + R_b B_{1234}, \quad (93)$$

$$\eta_{1234} = R_c C_{1234}, \quad (94)$$

where  $Q$ ,  $R_a$ ,  $R_b$ , and  $R_c$  are constants. In fact, the analysis of the two-dimensional galaxy catalogues [62] revealed

$$Q = 1.29 \pm 0.21 \quad (0.1h^{-1}\text{Mpc} \lesssim r \lesssim 10h^{-1}\text{Mpc}), \quad (95)$$

$$R_a = 2.5 \pm 0.6, \quad R_b = 4.3 \pm 1.2 \quad (0.5h^{-1}\text{Mpc} \lesssim r \lesssim 4h^{-1}\text{Mpc}). \quad (96)$$

The generalization of those relations for  $N$ -point correlation functions is suspected to be hold generally:

$$\xi_N(\mathbf{r}_1, \dots, \mathbf{r}_N) = \sum_j Q_{N,j} \sum_{(ab)} \prod_{(ab)}^{N-1} \xi(r_{ab}), \quad (97)$$

and called *the hierarchical clustering ansatz*. Cosmological N-body simulations approximately support the validity of the above ansatz, but also detect the finite deviation from it [74].

### 3.4 Genus statistics

A complementary approach to characterize the clustering of the universe beyond the two-point correlation functions is the genus statistics [23]. This is a mathematical measure of the topology of the isodensity surface. For definiteness, consider the density contrast field  $\delta(\mathbf{x})$  at the position  $\mathbf{x}$  in the survey volume  $V_{\text{all}}$ . This may be evaluated, for instance, by taking the ratio of the number of galaxies  $N(\mathbf{x}, V_f)$  in the volume  $V_f$  centered at  $\mathbf{x}$  to its average value  $\overline{N}(V_f)$ :

$$\delta(\mathbf{x}, V_f) = \frac{N(\mathbf{x}, V_f)}{\overline{N}(V_f)} - 1, \quad \sigma(V_f) = \langle |\delta(\mathbf{x}, V_f)|^2 \rangle^{1/2}, \quad (98)$$

where  $\sigma(V_f)$  is its rms value. Consider the isodensity surface parameterized by a value of  $\nu \equiv \delta(\mathbf{x}, V_f)/\sigma(V_f)$ . Genus is one of the topological numbers characterizing the surface defined as

$$g \equiv -\frac{1}{4\pi} \int \kappa \, dA, \quad (99)$$

where  $\kappa$  is the Gaussian curvature of the isolated surface. The Gauss – Bonnet theorem implies that the value of  $g$  is indeed an integer and equal to the number

of holes minus 1. This is qualitatively understood as follows; expand an arbitrary two-dimensional surface around a point as

$$z = \frac{1}{2}ax^2 + bxy + \frac{1}{2}cy^2 = \frac{1}{2}\kappa_1 x_1^2 + \frac{1}{2}\kappa_2 x_2^2. \quad (100)$$

Then the Gaussian curvature of the surface is defined by  $\kappa = \kappa_1\kappa_2$ . A surface topologically equivalent to a sphere (a torus) has  $\kappa = 1$  ( $\kappa = 0$ ), and thus equation (99) yields  $g = -1$  ( $g = 0$ ) which coincides with the number of holes minus 1.

In reality, there are many disconnected isodensity surfaces for a given  $\nu$ , and thus it is more convenient to define the genus density in the survey volume  $V_{\text{all}}$  using the additivity of the genus:

$$G(\nu) \equiv \frac{1}{V_{\text{all}}} \sum_{i=1}^I g_i = -\frac{1}{4\pi V_{\text{all}}} \sum_{i=1}^I \int_{A_i} \kappa \, dA, \quad (101)$$

where  $A_i$  ( $i = 1 \sim I$ ) denote the disconnected isodensity surfaces with the same value of  $\nu = \delta(\mathbf{x}, V_f)/\sigma(V_f)$ . Interestingly the Gaussian density field has an analytic expression for equation (101):

$$G(\nu) = \frac{1}{4\pi^2} \left( \frac{\langle k^2 \rangle}{3} \right)^{3/2} e^{-\nu^2/2} (1 - \nu^2), \quad (102)$$

where

$$\langle k^2 \rangle \equiv \frac{\int k^2 P(k) \tilde{W}^2(kR) d^3k}{\int P(k) \tilde{W}^2(kR) d^3k} \quad (103)$$

is the moment of  $k^2$  weighted over the power spectrum of fluctuations  $P(k)$ , and the smoothing function  $\tilde{W}^2(kR)$  (e.g., ref. [4]). It should be noted that in the Gaussian density field the information of the power spectrum shows up only in the proportional constant of equation (102), and its functional form is determined uniquely by the threshold value  $\nu$ . This  $\nu$ -dependence reflects the phase information which is ignored in the two-point correlation function and power spectrum. In this sense, genus statistics is a complementary measure of the clustering pattern of universe.

Even if the primordial density field obeys the Gaussian statistics, the subsequent nonlinear gravitational evolution generates the significant non-Gaussianity. To distinguish the initial non-Gaussianity from that acquired by the nonlinear gravity is of fundamental importance in inferring the initial condition of the universe in a standard gravitational instability picture of structure formation. In a weakly nonlinear regime, Matsubara (1996) derived an analytic expression

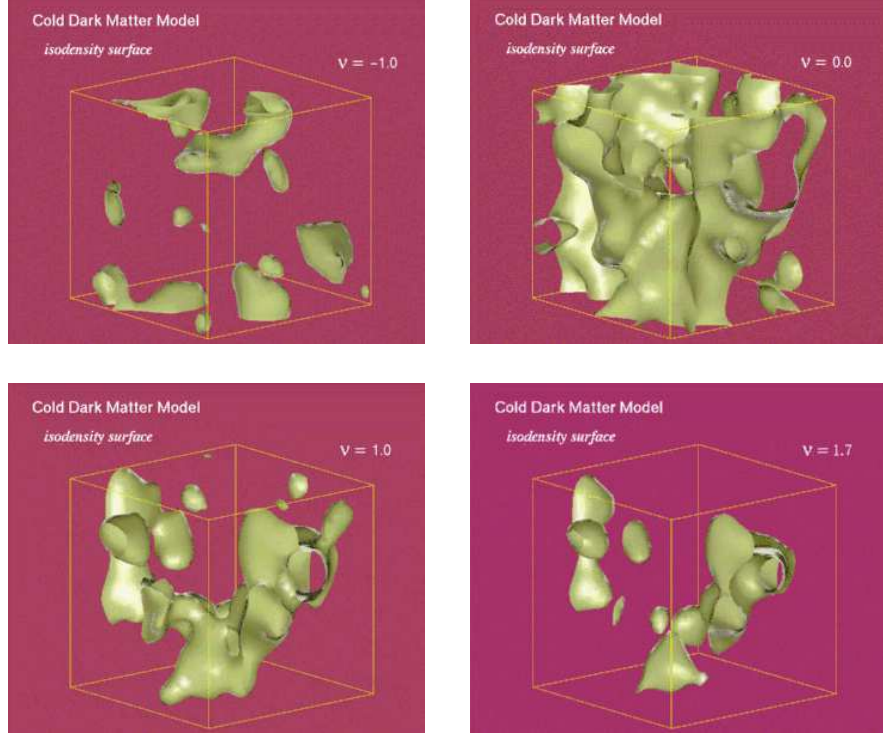


Figure 4: Isodensity surfaces of dark matter distribution from N-body simulation; LCDM in  $(100h^{-1}\text{Mpc})^3$  at  $\nu = -1.0, 0.0, 1.0$ , and  $1.7$ . (ref. [47])

for the non-Gaussianity emerging from the primordial Gaussian field [45]:

$$G(\nu) = -\frac{1}{4\pi^2} \left( \frac{\langle k^2 \rangle}{3} \right)^{3/2} e^{-\nu^2/2} \left[ H_2(\nu) + \sigma \left( \frac{S}{6} H_5(\nu) + \frac{3T}{2} H_3(\nu) + 3U H_1(\nu) \right) \right], \quad (104)$$

where

$$H_n(\nu) \equiv (-1)^n e^{\nu^2/2} \left( \frac{d}{d\nu} \right)^n e^{-\nu^2/2} \quad (105)$$

are the Hermite polynomials;  $H_1 = \nu$ ,  $H_2 = \nu^2 - 1$ ,  $H_3 = \nu^3 - 3\nu$ ,  $H_4 = \nu^4 - 6\nu^2 + 3$ ,  $H_5 = \nu^5 - 10\nu^3 + 15\nu$ , .... The three quantities:

$$S = \frac{1}{\sigma^4} \langle \delta^3 \rangle, \quad T = -\frac{1}{2\langle k^2 \rangle \sigma^4} \langle \delta^2 \nabla^2 \delta \rangle, \quad U = -\frac{3}{4\langle k^2 \rangle^2 \sigma^4} \langle \nabla \delta \cdot \nabla \delta \nabla^2 \delta \rangle \quad (106)$$

denote the third-order moments of  $\delta$ . This expression plays a key role in un-

derstanding if the non-Gaussianity in galaxy distribution is ascribed to the primordial departure from the Gaussian statistics.

### 3.5 Minkowski functionals

In fact, genus is one of the complete sets of  $N + 1$  quantities, known as the Minkowski functionals (MFs), which determine the morphological properties of a pattern in  $N$ -dimensional space. In the analysis of galaxy redshift survey data, one considers isodensity contours from the three-dimensional density contrast field  $\delta$  by taking its excursion set  $F_\nu$ , i.e., the set of all points where the density contrast  $\delta$  exceeds the threshold level  $\nu$  as was the case in the case of genus described in the above subsection.

All MFs can be expressed as integrals over the excursion set. While the first MF is simply given by the volume integration of a Heaviside step function  $\Theta$  normalized to the total volume  $V_{\text{tot}}$ ,

$$V_0(\nu) = \frac{1}{V_{\text{tot}}} \int_V d^3x \Theta(\nu - \nu(x)), \quad (107)$$

the other MFs,  $V_k$  ( $k = 1, 2, 3$ ), are calculated by the surface integration of the local MFs,  $v_k^{\text{loc}}$ . The general expression is

$$V_k(\nu) = \frac{1}{V_{\text{tot}}} \int_{\partial F_\nu} d^2S(\mathbf{x}) v_k^{\text{loc}}(\nu, \mathbf{x}), \quad (108)$$

with the local Minkowski Functionals for  $k = 1, 2, 3$  given by

$$v_1^{\text{loc}}(\nu, \mathbf{x}) = \frac{1}{6}, \quad (109)$$

$$v_2^{\text{loc}}(\nu, \mathbf{x}) = \frac{1}{6\pi} \left( \frac{1}{R_1} + \frac{1}{R_2} \right), \quad (110)$$

$$v_3^{\text{loc}}(\nu, \mathbf{x}) = \frac{1}{4\pi} \frac{1}{R_1 R_2}, \quad (111)$$

where  $R_1$  and  $R_2$  are the principal radii of curvature of the isodensity surface.

For a 3-D Gaussian random field, the average MFs per unit volume can be expressed analytically as follows:

$$V_0(\nu) = \frac{1}{2} - \frac{1}{\sqrt{2\pi}} \int_0^\nu \exp\left(-\frac{x^2}{2}\right) dx, \quad (112)$$

$$V_1(\nu) = \frac{2}{3} \frac{\lambda}{\sqrt{2\pi}} \exp\left(-\frac{1}{2}\nu^2\right) \quad (113)$$

$$V_2(\nu) = \frac{2}{3} \frac{\lambda^2}{\sqrt{2\pi}} \nu \exp\left(-\frac{1}{2}\nu^2\right), \quad (114)$$

$$V_3(\nu) = \frac{\lambda^3}{\sqrt{2\pi}} (\nu^2 - 1) \exp\left(-\frac{1}{2}\nu^2\right), \quad (115)$$

where  $\lambda = \sqrt{\sigma_1^2/6\pi\sigma^2}$ ,  $\sigma \equiv \langle \delta^2 \rangle^{1/2}$ ,  $\sigma_1 \equiv \langle |\nabla \delta|^2 \rangle^{1/2}$ , and  $\delta$  is the density contrast.

The above MFs can be indeed interpreted as well-known geometric quantities; the volume fraction  $V_0(\nu)$ , the total surface area  $V_1(\nu)$ , the integral mean curvature  $V_2(\nu)$ , and the integral Gaussian curvature, i.e., the Euler characteristic  $V_3(\nu)$ . In our current definitions (eqs. [101] and [108], or eqs.[102] and [115]), one can easily show that  $V_3(\nu)$  reduces simply to  $-G(\nu)$ . The MFs were first introduced to cosmological studies by Mecke et al. (1994) [52], and further details may be found in refs. [52, 27]. Analytic expressions of MFs in weakly non-Gaussian fields are derived in ref. [46].

## 4 Galaxy biasing

### 4.1 Concepts and definitions of biasing

As discussed above, luminous objects, such as galaxies and quasars, are not direct tracers of the mass in the universe. In fact, the difference of the spatial distribution between luminous objects and dark matter, or the *bias*, has been indicated from a variety of observations. Galaxy “biasing” clearly exists. The fact that galaxies of different types cluster differently (e.g., ref. [14]) implies that not all of them are exact tracers of the underlying mass distribution. See also §6.

In order to confront theoretical model predictions for the *mass* distribution against observational data, one needs a relation of density fields of mass and luminous objects. The biasing of density peaks in a Gaussian random field is well formulated [33, 4] and it provides the first theoretical framework for the origin of galaxy density biasing. In this scheme, the galaxy–galaxy and mass–mass correlation functions are related in the linear regime via

$$\xi_{gg}(r) = b^2 \xi_{mm}(r), \quad (116)$$

where the biasing parameter  $b$  is a constant independent of scale  $r$ . However, a much more specific linear biasing model is often assumed in common applications, in which the local density fluctuation fields of galaxies and mass are assumed to be deterministically related via the relation

$$\delta_g(\mathbf{x}) = b \delta_m(\mathbf{x}). \quad (117)$$

Note that equation (116) follows from equation (117), but the reverse is not true.

The above deterministic linear biasing is not based on a reasonable physical motivation. If  $b > 1$ , it must break down in deep voids because values of  $\delta_g$  below  $-1$  are forbidden by definition. Even in the simple case of no evolution in comoving galaxy number density, the linear biasing relation is not preserved during the course of fluctuation growth. Non-linear biasing, where  $b$  varies with  $\delta_m$ , is inevitable.

Indeed, an analytical model for biasing of halos on the basis of the extended Press-Schechter approximation [53] predicts that the biasing is nonlinear and provides a useful approximation for its behavior as a function of scale, time and mass threshold.  $N$ -body simulations provide a more accurate description of the nonlinearity of the halo biasing confirming the validity of the Mo & White model [32, 81].

### 4.2 Modeling biasing

Biasing is likely to be *stochastic*, not deterministic [13]. An obvious part of this stochasticity can be attributed to the discrete sampling of the density field by

galaxies, i.e. the shot noise. In addition, a statistical, physical scatter in the efficiency of galaxy formation as a function of  $\delta_m$  is inevitable in any realistic scenario. For example, the random variations in the density on smaller scales is likely to be reflected in the efficiency of galaxy formation. As another example, the local geometry of the background structure, via the deformation tensor, must play a role too. Such ‘hidden variables’ would show up as physical scatter in the density-density relation [77].

Consider the density contrasts of visible objects and mass,  $\delta_{\text{obj}}(\mathbf{x}, z|R)$  and  $\delta_m(\mathbf{x}, z|R)$ , at a position  $\mathbf{x}$  and a redshift  $z$  smoothed over a scale  $R$  [78]. In general, the former should depend on various other auxiliary variables  $\vec{\mathcal{A}}$  defined at different locations  $\mathbf{x}'$  and redshifts  $z'$  smoothed over different scales  $R'$  in addition to the mass density contrast at the same position,  $\delta_m(\mathbf{x}, z|R)$ . While this relation can be schematically expressed as

$$\delta_{\text{obj}}(\mathbf{x}, z|R) = \mathcal{F}[\mathbf{x}, z, R, \delta_m(\mathbf{x}, z|R), \vec{\mathcal{A}}(\mathbf{x}', z'|R'), \dots], \quad (118)$$

it is impossible even to specify the list of the astrophysical variables  $\vec{\mathcal{A}}$ , and thus hopeless to predict the functional form in a rigorous manner. Therefore if one simply focuses on the relation between  $\delta_{\text{obj}}(\mathbf{x}, z|R)$  and  $\delta_m(\mathbf{x}, z|R)$ , the relation becomes inevitably *stochastic* and *nonlinear* due to the dependence on unspecified auxiliary variables  $\vec{\mathcal{A}}$ .

For illustrative purposes, define the *biasing* factor as the ratio of the density contrasts of luminous objects and mass:

$$B_{\text{obj}}(\mathbf{x}, z|R) \equiv \frac{\delta_{\text{obj}}(\mathbf{x}, z|R)}{\delta_m(\mathbf{x}, z|R)} = \frac{\mathcal{F}[\mathbf{x}, z, R, \delta_m(\mathbf{x}, z|R), \vec{\mathcal{A}}(\mathbf{x}', z'|R'), \dots]}{\delta_m(\mathbf{x}, z|R)}. \quad (119)$$

Only in very idealized situations, the above *nonlocal stochastic nonlinear* factor in terms of  $\delta_m$  may be approximated by

1. a *local stochastic nonlinear* bias:

$$B_{\text{obj}}(\mathbf{x}, z|R) = b_{\text{obj}}^{(\text{sn})}[\mathbf{x}, z, R, \delta_m(\mathbf{x}, z|R), \vec{\mathcal{A}}(\mathbf{x}, z|R), \dots], \quad (120)$$

2. a *local deterministic nonlinear* bias:

$$B_{\text{obj}}(\mathbf{x}, z|R) = b_{\text{obj}}^{(\text{dn})}[z, R, \delta_m(\mathbf{x}, z|R)], \quad (121)$$

and

3. a *local deterministic linear* bias:

$$B_{\text{obj}}(\mathbf{x}, z|R) = b_{\text{obj}}(z, R) \quad (122)$$

From the above point of view, the local deterministic linear bias is obviously unrealistic, but is still a widely used conventional model for biasing. In fact, the

time- and scale-dependence of the linear bias factor  $b_{\text{obj}}(z, R)$  was neglected in many previous studies of biased galaxy formation until very recently. Currently, however, various models beyond the deterministic linear biasing have been seriously considered with particular emphasis on the nonlinear and stochastic aspects of the biasing [65, 13, 77, 78].

### 4.3 Density peaks and dark matter halos as toy models for galaxy biasing

Let us illustrate the biasing from numerical simulations by considering two specific and popular models; primordial density peaks and dark matter halos [78]. We use the N-body simulation data of  $L = 100h^{-1}\text{Mpc}$  again for this purpose [31]. We select density peaks with the threshold of the peak height  $\nu_{\text{th}} = 1.0, 2.0$ , and  $3.0$ . As for the dark matter halos, these are identified using the standard friend-of-friend algorithm with a linking length of  $0.2$  in units of the mean particle separation. We select halos of mass larger than the threshold  $M_{\text{th}} = 2.0 \times 10^{12}, 5.0 \times 10^{12}$  and  $1.0 \times 10^{13} h^{-1} M_{\odot}$ .

Figures 5 and 6 depicts the distribution of dark matter particles (*upper-panel*), peaks (*middle-panel*) and halos (*lower-panel*) in  $\Lambda\text{CDM}$  model at  $z = 0$  and  $z = 2.2$  within a circular slice (*comoving* radius of  $150h^{-1}\text{Mpc}$  and thickness of  $15h^{-1}\text{Mpc}$ ). We locate a fiducial observer in the center of the circle. Then the *comoving* position vector  $\mathbf{r}$  for a particle with a *comoving* peculiar velocity  $\mathbf{v}$  at a redshift  $z$  is observed at the position  $\mathbf{s}$  in redshift space:

$$\mathbf{s} = \mathbf{r} + \frac{1}{H(z)} \frac{\mathbf{r} \cdot \mathbf{v}}{|\mathbf{r}|} \frac{\mathbf{r}}{|\mathbf{r}|}, \quad (123)$$

where  $H(z)$  is the Hubble parameter at  $z$ . The right panels in Figures 5 and 6 plot the observed distribution in redshift space, where the redshift-space distortion is quite visible; the coherent velocity field enhances the structure perpendicular to the line-of-sight of the observer (*squashing*) while the virialized clump becomes elongated along the line-of-sight (*finger-of-God*).

We use two-point correlation functions to quantify stochasticity and nonlinearity in biasing of peaks and halos, and explore the signature of the redshift-space distortion. Since we are interested in the relation of the biased objects and the dark matter, we introduce three different correlation functions; the auto-correlation functions of dark matter and the objects,  $\xi_{\text{mm}}$  and  $\xi_{\text{oo}}$ , and their cross-correlation function  $\xi_{\text{om}}$ . In the present case, the subscript  $\text{o}$  refers to either  $\text{h}$  (halos) or  $\nu$  (peaks). We also use the superscripts  $\text{R}$  and  $\text{S}$  to distinguish quantities defined in real and redshift spaces, respectively. We estimate those correlation functions using the standard pair-count method. The correlation function  $\xi^{(S)}$  is evaluated under the distant-observer approximation.

Those correlation functions are plotted in Figures 7 and 8 for peaks and halos, respectively. The correlation functions of biased objects generally have

larger amplitudes than those of mass. In nonlinear regimes ( $\xi > 1$ ) the finger-of-god effect suppresses the amplitude of  $\xi^{(S)}$  relative to  $\xi^{(R)}$ , while  $\xi^{(S)}$  is larger than  $\xi^{(R)}$  in linear regimes ( $\xi < 1$ ) due to the coherent velocity field.

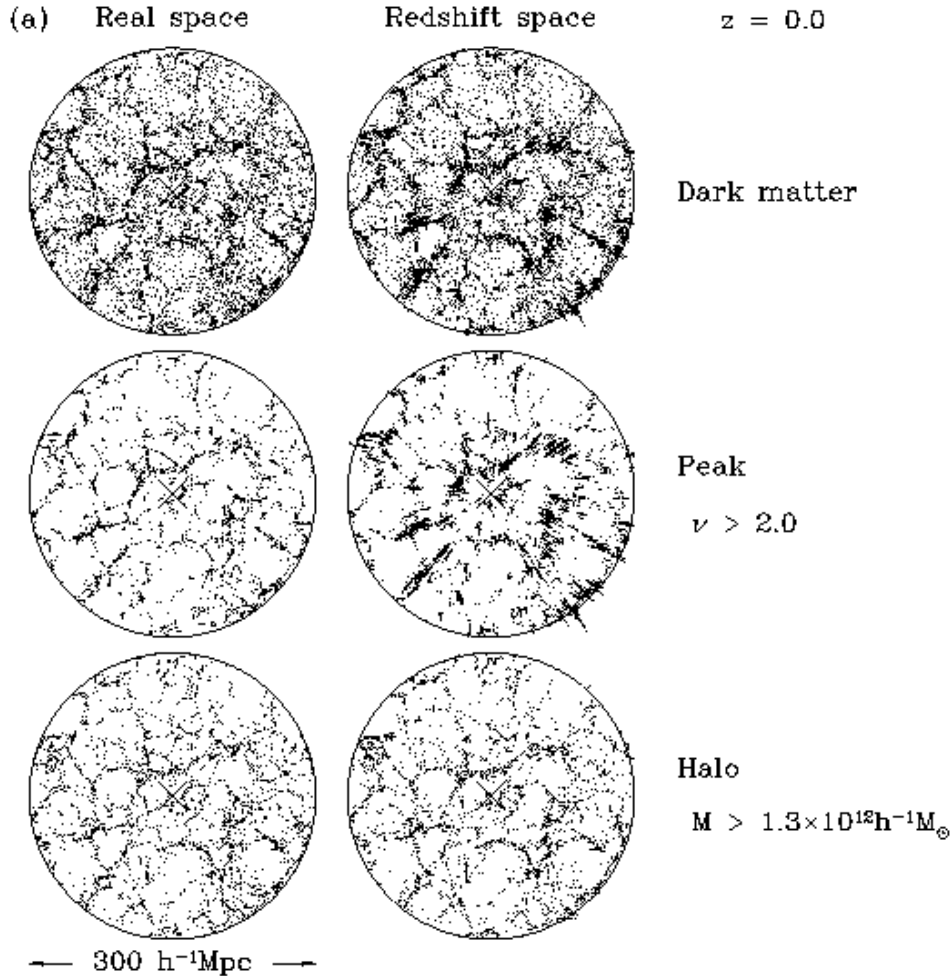


Figure 5: Top-view of distribution of objects at  $z = 0$  in real (left panels) and redshift (right panels) spaces around the fiducial observer at the center; dark matter particles (top panels), peaks with  $\nu > 2$  (middle panels) and halos with  $M > 1.3 \times 10^{12} M_{\odot}$  (bottom panels) in LCDM model. The thickness of those slices is  $15 h^{-1} \text{Mpc}$ . (ref. [78])

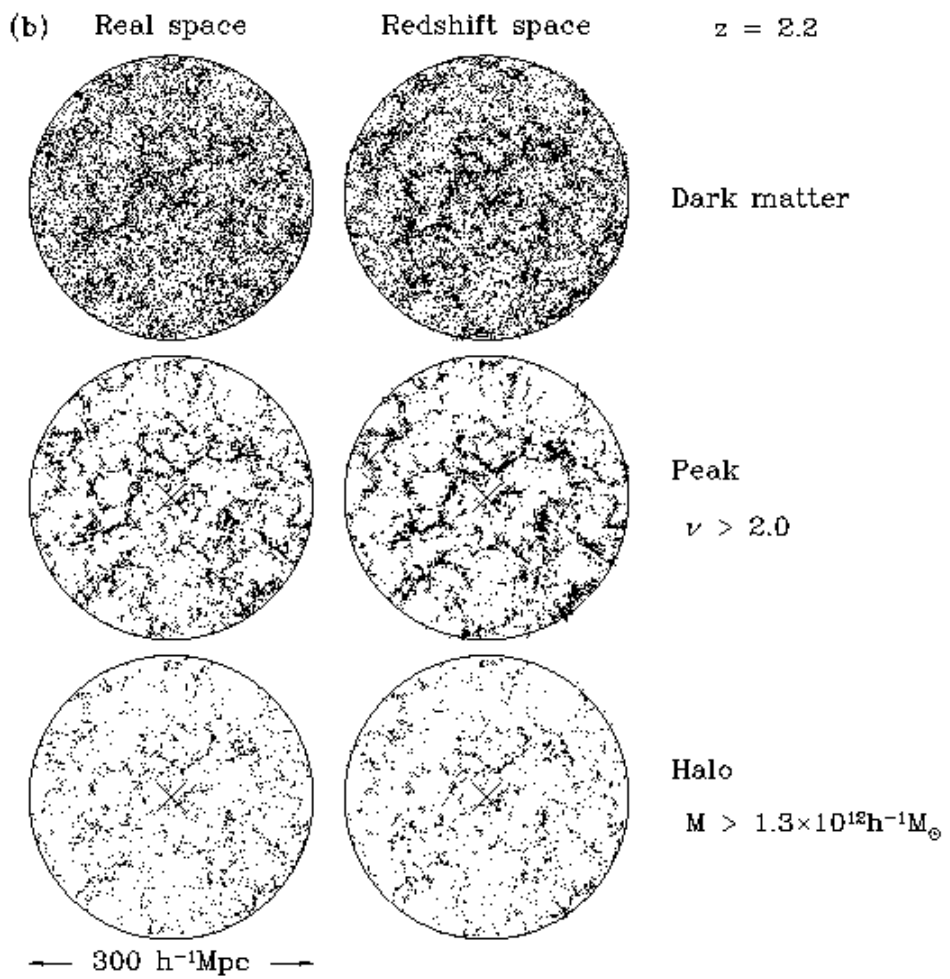


Figure 6: Same as Fig.5 but at  $z = 2.2$ . (ref. [78])

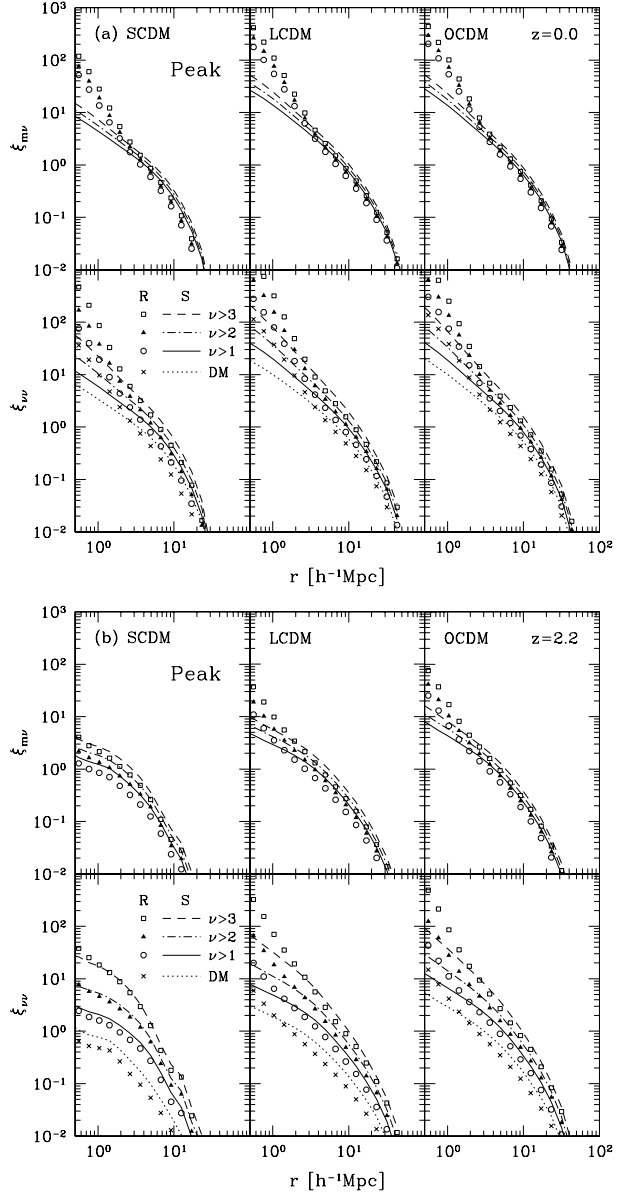


Figure 7: Auto- and cross-correlation functions of dark matter and peaks in SCDM (left panels), LCDM (middle panels) and OCDM (right panels). Different symbols indicate the results in real space (open squares for  $\nu > 3$ , filled triangles for  $\nu > 2$ , open circles for  $\nu > 1$ , and crosses for dark matter), while different curves indicate those in redshift space (dashed for  $\nu > 3$ , dot-dashed for  $\nu > 2$ , solid for  $\nu > 1$ , and dotted for dark matter). (a)  $z = 0$ , (b)  $z = 2.2$ . (ref. [78])

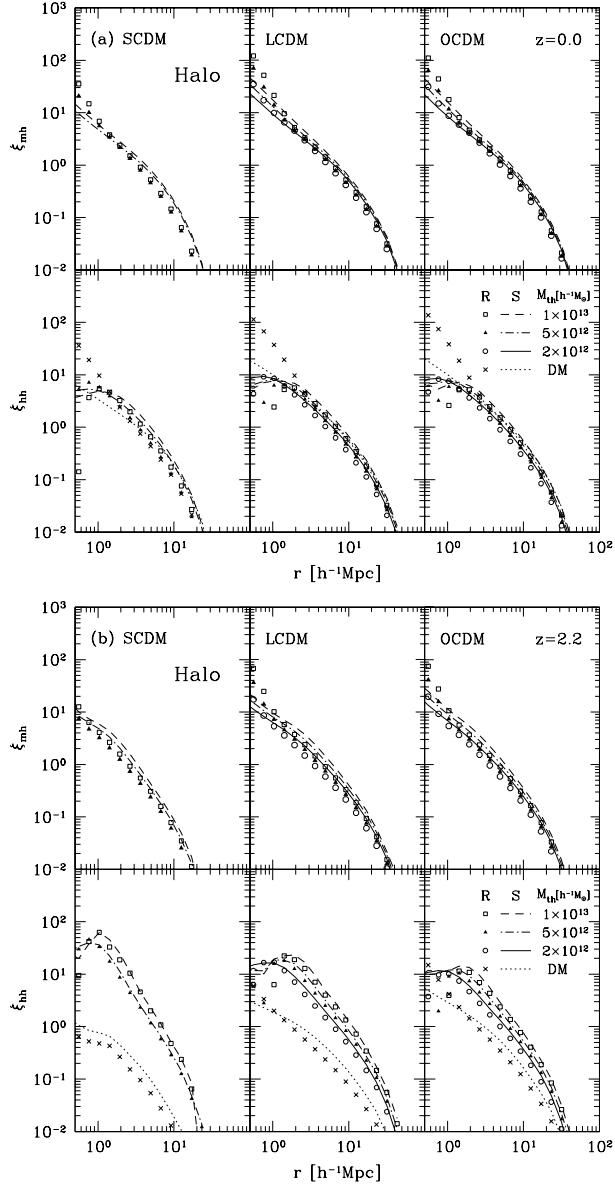


Figure 8: Same as Fig. 7 but for halo model; open squares and dashed lines for  $M > 10^{13}h^{-1}M_{\odot}$ , filled triangles and dot-dashed lines for  $M > 5 \times 10^{12}h^{-1}M_{\odot}$ , open circles and solid lines for  $M > 2 \times 10^{12}h^{-1}M_{\odot}$ , and crosses and dotted lines for dark matter. For SCDM model, we only plot the correlation functions with  $M_{\text{th}} = 5 \times 10^{12}, 10^{13}h^{-1}M_{\odot}$ . (a)  $z = 0$ , (b)  $z = 2.2$ . (ref. [78])

#### 4.4 Biasing of galaxies in cosmological hydrodynamic simulations

Popular models of the biasing based on the peak or the dark halos are successful in capturing some essential features of biasing. None of the existing models of bias, however, seems to be sophisticated enough for the coming precision cosmology era. Development of a more detailed theoretical model of bias is needed. A straightforward next step is to resort to numerical simulations which take account of galaxy formation even if phenomenological at this point. We show an example of such approaches from Yoshikawa et al. (2001) [81] who apply cosmological smoothed particle hydrodynamic simulations in  $\Lambda$ CDM model with particular attention to the comparison of the biasing of dark halos and simulated galaxies (see also ref. [71]).

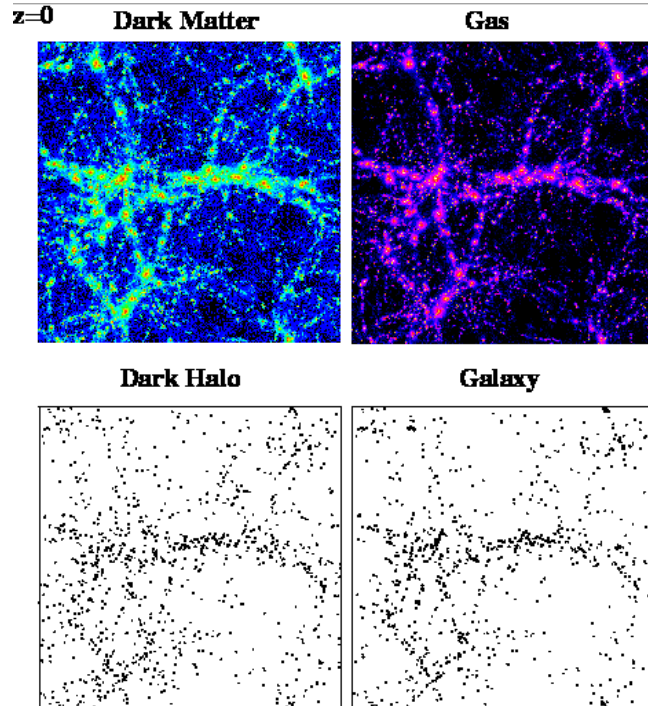


Figure 9: Distribution of gas particles, dark matter particles, galaxies and dark halos in the volume of  $75h^{-1} \times 75h^{-1} \times 30h^{-1}\text{Mpc}^3$  model at  $z = 0$ . *Upper-right*: gas particles; *Upper-left*: dark matter particles; *Lower-right*: galaxies; *Lower-left*: DM cores. (ref. [81])

Figure 9 illustrates the distribution of dark matter particles, gas particles, dark halos and galaxies at  $z = 0$  where galaxies are more strongly clustered than dark halos. Figure 10 depicts a close-up snapshot of the most massive cluster at  $z = 0$  with mass  $M \simeq 8 \times 10^{14} M_{\odot}$ . Circles in lower panels indicate the positions of galaxies identified in our simulation.

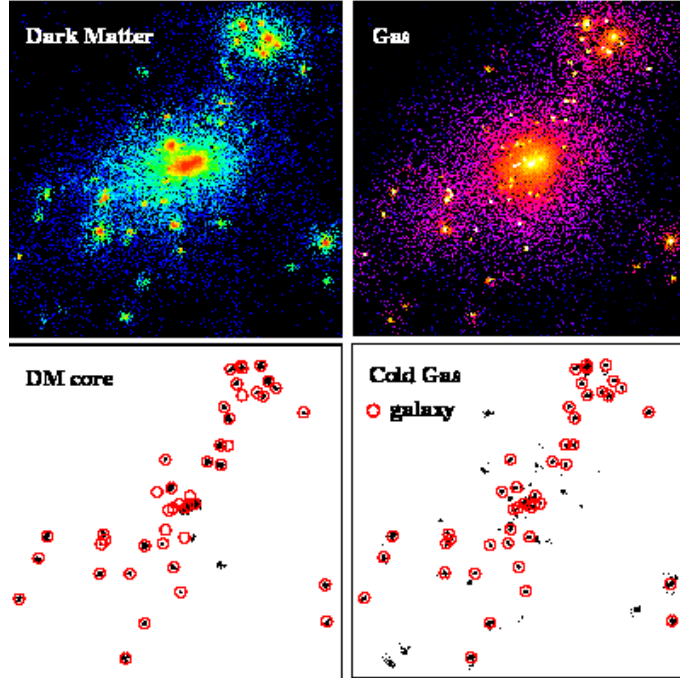


Figure 10: Snapshots of the most massive cluster ( $M \simeq 8 \times 10^{14} M_{\odot}$ ) in the simulation at  $z = 0$ . *Upper-left:* dark matter; *Upper-right:* gas; *Lower-left:* DM cores; *Lower-right:* cold gas. Circles in lower panels indicate the positions of galaxies identified according to our criteria. The comoving size of the box is  $6.25h^{-1}\text{Mpc}$  per side. (ref. [81])

Figure 11 shows the joint distribution of  $\delta_h$  and  $\delta_g$  with mass density field  $\delta_m$  at redshift  $z = 0, 1$  and  $2$  smoothed over  $R_s = 12h^{-1}\text{Mpc}$ . The conditional mean relation  $\delta_i(\delta_m)$  computed directly from the simulation is plotted in solid lines while dashed lines indicate theoretical predictions of halo biasing by Taruya & Suto (2000) [77]. For a given smoothing scale, the simulated halos exhibit positive biasing for relatively small  $\delta_m$  in agreement with the predictions. On the other hand, they tend to be underpopulated for large  $\delta_m$ , or *anti-biased*. This is mainly due to the exclusion effect of dark halos due to their finite volume size

which is not taken into account in the theoretical model. Since our simulated *galaxies* have smaller spatial extent than the halos, the exclusion effect is not so serious. This is clearly illustrated in lower panels in Figure 11, and indeed they show much better agreement with the theoretical model.

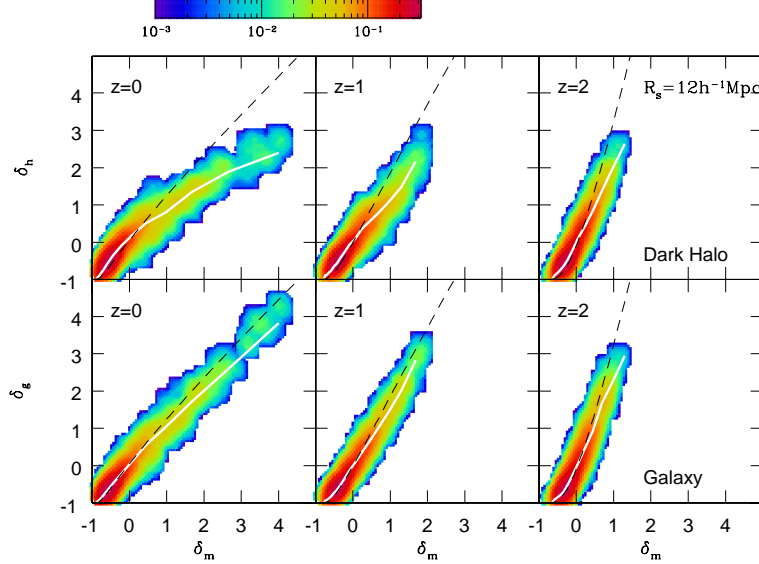


Figure 11: Joint probability distributions of overdensity fields for dark halos and galaxies with dark matter overdensity smoothed over  $R_s = 12h^{-1}\text{Mpc}$  at redshift  $z = 0, 1$  and  $2$ . Solid lines indicate the conditional mean  $\bar{\delta}_i(\delta_m)$  for each object. Dashed lines in each panel depict the theoretical prediction of conditional mean by Taruya & Suto (2000). (ref. [81])

Turn next to a more conventional biasing parameter defined through the two-point statistics:

$$b_{\xi,i}(r) \equiv \sqrt{\frac{\xi_{ii}(r)}{\xi_{mm}(r)}}, \quad (124)$$

where  $\xi_{ii}(r)$  and  $\xi_{mm}(r)$  are two-point correlation functions of objects  $i$  and of dark matter, respectively. While the above biasing parameter is ill-defined where either  $\xi_{ii}(r)$  or  $\xi_{mm}(r)$  becomes negative, it is not the case at clustering scales of interest ( $< 10h^{-1}\text{Mpc}$ ). Figure 12 shows two-point correlation functions of dark matter, galaxies, dark halos and DM cores (*upper and middle panels*), and the profiles of biasing parameters  $b_\xi(r)$  for those objects (*lower panels*) at  $z = 0, 1$  and  $2$ . In lower panels, we also plot the parameter  $b_{\text{var}}$  on the smoothing scale  $R_s = 4h^{-1}\text{Mpc}$ ,  $8h^{-1}\text{Mpc}$  and  $12h^{-1}\text{Mpc}$  at  $r = R_s$  for each kind of objects

by different symbols. In the upper panels, we show the correlation functions of DM cores identified with two different maximum linking length;  $l_{\max} = 0.05$  and  $l_{\max} = b_h/2$ . Correlation functions of DM cores identified with  $l_{\max} = 0.05$  are similar to those of galaxies. On the other hand, those identified with  $l_{\max} = b_h/2$  exhibit much weaker correlation, and are rather similar to those of dark halos. This is due to the fact that the present algorithm of group identification with larger  $l_{\max}$  tends to pick up lower mass halos which are poorly resolved in our numerical resolution.

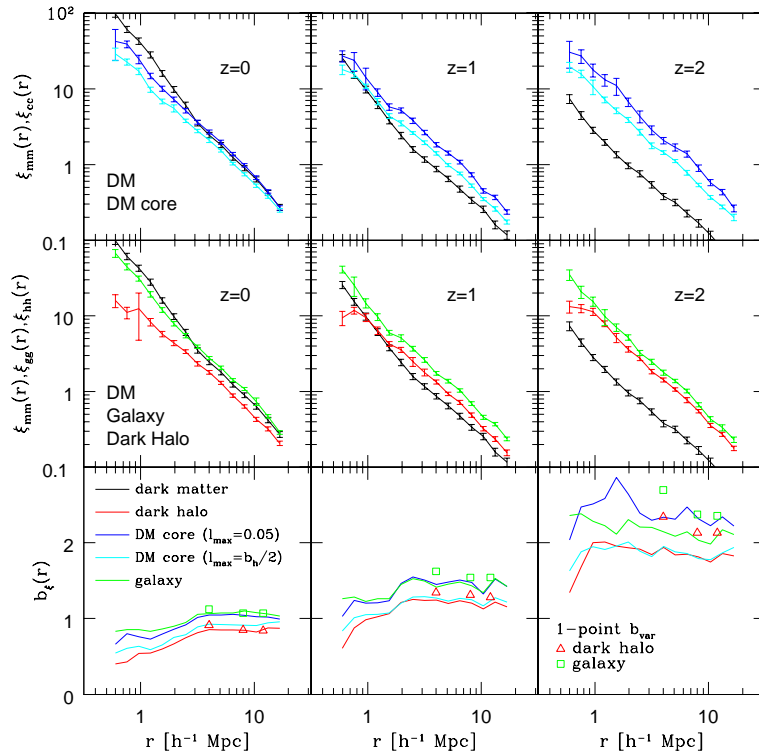


Figure 12: Two-point correlation functions of dark matter, galaxies, and dark halos from cosmological hydrodynamical simulations. (ref. [81])

The correlation functions of galaxies are almost unchanged with redshift, and that of dark halos only slightly evolves between  $z = 0$  and 2. By contrast, the amplitude of the dark matter correlation function evolves rapidly by factor of  $\sim 10$  from  $z = 2$  to  $z = 0$ . The biasing parameter  $b_{\xi,g}$  is larger at a higher redshift, for example,  $b_{\xi,g} \simeq 2\text{--}2.5$  at  $z = 2$ . The biasing parameter  $b_{\xi,h}$  for dark halos is systematically lower than that of galaxies and DM cores again due

to the volume exclusion effect. At  $z = 0$ , galaxies and DM cores are slightly anti-biased relative to dark matter at  $r \simeq 1h^{-1}\text{Mpc}$ . In lower panels, we also plot the one-point biasing parameter  $b_{\text{var},i} \equiv \sigma_i/\sigma_{\text{m}}$  at  $r = R_s$  for comparison. In general we find that  $b_{\xi,i}$  is very close to  $b_{\text{var},i}$  at  $z \sim 0$ , but systematically lower than  $b_{\text{var},i}$  at higher redshifts.

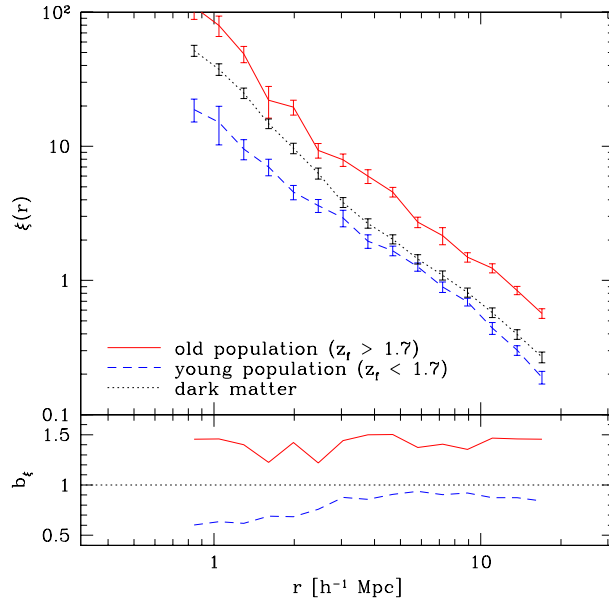


Figure 13: Two-point correlation functions for the old and young populations of galaxies at  $z = 0$  as well as that of dark matter distribution. The profiles of bias parameters  $b_\xi(r)$  for both of the two populations are also shown in the lower panel. (ref. [81])

For each galaxy identified at  $z = 0$ , we define its formation redshift  $z_f$  by the epoch when half of its *cooled gas* particles satisfy our criteria of galaxy formation. Roughly speaking,  $z_f$  corresponds to the median formation redshift of *stars* in the present-day galaxies. We divide all simulated galaxies at  $z = 0$  into two populations (the young population with  $z_f < 1.7$  and the old population with  $z_f > 1.7$ ) so as to approximate the observed number ratio of 3/1 for late-type and early-type galaxies.

The difference of the clustering amplitude can be also quantified by their two-point correlation functions at  $z = 0$  as plotted in Figure 13. The old population indeed clusters more strongly than the mass, and the young population is anti-biased. The relative bias between the two populations  $b_{\xi,g}^{\text{rel}} \equiv \sqrt{\xi_{\text{old}}/\xi_{\text{young}}}$

ranges 1.5 and 2 for  $1h^{-1}\text{Mpc} < r < 20h^{-1}\text{Mpc}$ , where  $\xi_{\text{young}}$  and  $\xi_{\text{old}}$  are the two-point correlation functions of the young and old populations.

#### 4.5 Halo occupation function approach for galaxy biasing

Since the clustering of dark matter halos is well understood now, one can describe the galaxy biasing if the halo model is combined with the relation between the halos and luminous objects. This is another approach to galaxy biasing, *halo occupation function* (HOF), which becomes very popular recently. Indeed the basic idea behind HOF has a long history, but the model predictions have been significantly improved with the recent accurate models for the mass function, the biasing and the density profile of dark matter halos. We refer the readers for an extensive review on the HOF by Cooray & Sheth (2002) [12]. Here we briefly outline this approach.

We adopt a simple parametric form for the average number of a given galaxy population as a function of the hosting halo mass:

$$N_g(M) = \begin{cases} (M/M_1)^\alpha & (M > M_{\min}) \\ 0 & (M < M_{\min}) \end{cases}. \quad (125)$$

The above statistical and empirical relation is the essential ingredient in the current modeling characterized by the minimum mass of halos which host the population of galaxies ( $M_{\min}$ ), a normalization parameter which can be interpreted as the critical mass above which halos typically host more than one galaxy ( $M_1$ ; note that  $M_1$  may exceed  $M_{\min}$  since the above relation represents the statistical expected value of number of galaxies), and the power-law index of the mass dependence of the efficiency of galaxy formation ( $\alpha$ ). We will put constraints on the three parameters from the observed number density and clustering amplitude for each galaxy population. In short, the number density of galaxies is most sensitive to  $M_1$  which changes the average number of galaxies per halo. The clustering amplitude on large scales is determined by the hosting halos and thus very sensitive to the mass of those halos,  $M_{\min}$ . The clustering on smaller scales, on the other hand, depends on those three parameters in a fairly complicated fashion; roughly speaking,  $M_{\min}$  changes the amplitude,  $\alpha$ , and to a lesser extent  $M_1$  as well, changes the slope.

With the above relation, the number density of the corresponding galaxy population at redshift  $z$  is given by

$$n_{g,z}(z) = \int_{M_{\min}}^{\infty} dM n_{\text{halo}}(M, z) N_g(M), \quad (126)$$

where  $n_{\text{halo}}(M)$  denotes the halo mass function.

The galaxy two-point correlation function on small scales is dominated by contributions of galaxy pairs located in the same halo. For instance, Bullock

et al. (2002) [8] adopted the mean number of galaxy pairs  $\langle N_g(N_g - 1) \rangle(M)$  within a halo of mass  $M$  of the form:

$$\langle N_g(N_g - 1) \rangle(M) = \begin{cases} N_g^2(M) & (N_g(M) > 1) \\ N_g^2(M) \log(4N_g(M))/\log(4) & (1 > N_g(M) > 0.25) \\ 0 & (N_g(M) < 0.25) \end{cases}. \quad (127)$$

In the framework of the halo model, the galaxy power spectrum consists of two contributions, one from galaxy pairs located in the same halo (1-halo term) and the other from galaxy pairs located in two different halos (2-halo term):

$$P_g^{tot}(k) = P_g^{1h}(k) + P_g^{2h}(k). \quad (128)$$

The 1-halo term is written as

$$P_g^{1h}(k) = \frac{1}{(2\pi)^3 n_{g,z}^2} \int dM n_{\text{halo}}(M) \langle N_g(N_g - 1) \rangle b(M) |y(k, M)|^p. \quad (129)$$

Seljak (2000) [70] chose  $p = 2$  for  $\langle N_g(N_g - 1) \rangle > 1$  and  $p = 1$  for  $\langle N_g(N_g - 1) \rangle < 1$ . The 2-halo term on the assumption of the linear halo bias model [53] reduces to

$$P_g^{2h}(k) = \frac{P_{\text{lin}}(k)}{n_{g,z}^2} \left[ \int dM n_{\text{halo}}(M) N_g(M) b(M) y(k, M) \right]^2, \quad (130)$$

where  $P_{\text{lin}}(k)$  is the linear dark matter power spectrum,  $b(M)$  is the halo bias factor, and  $y(k, M)$  is the Fourier transform of the halo dark matter profile normalized by its mass,  $y(k, M) = \bar{\rho}(k, M)/M$  [70].

The halo occupation formalism, although simple, provides a useful framework in deriving constraints on galaxy formation models from large data sets of the upcoming galaxy redshift surveys. For example, Zehavi et al. (2003) [86] used the halo occupation formalism to model departures from a power law in the SDSS galaxy correlation function. They demonstrated that this is due to the transition from a large-scale regime dominated by galaxy pairs in different halos to a small-scale regime dominated by those in the same halo. Magliocchetti & Porciani (2003) [43] applied the halo occupation formalism to the 2dFGRS clustering results per spectral type of Madgwick et al. (2003) [41]. This provides constraints on the distribution of late-type and early-type galaxies within the dark matter halos of different mass.

## 5 Relativistic effects observable in clustering at high redshifts

Redshift surveys of galaxies definitely serve as the central database for observational cosmology. In addition to the existing *shallower* surveys ( $z < 0.2$ ), clustering in the universe in the range  $z = 1 - 3$  has been partially revealed by, for instance, the Lyman-break galaxies and X-ray selected AGNs. In particular, the 2dF and SDSS QSO redshift surveys promise to extend the observable scale of the universe by an order of magnitude, up to a few Gpc. A proper interpretation of such redshift surveys in terms of the clustering evolution, however, requires an understanding of many cosmological effects which can be neglected for  $z \ll 1$  and thus have not been considered seriously so far. These cosmological *contaminations* include linear redshift-space (velocity) distortion, nonlinear redshift-space (velocity) distortion, cosmological redshift-space (geometrical) distortion, and cosmological light-cone effect.

We describe a theoretical formalism to incorporate those effects, in particular the cosmological redshift-distortion and light-cone effects, and present several specific predictions in CDM models. The details of the material presented in this section may be found in refs. [75, 79, 80, 42, 24, 25].

### 5.1 Cosmological lightcone effect on the two-point correlation functions

Observing a distant patch of the universe is equivalent to observing the past. Due to the finite light velocity, a line-of-sight direction of a redshift survey is along the time, as well as spatial, coordinate axis. Therefore the entire sample does not consist of objects on a constant-time hypersurface, but rather on a light-cone, i.e., a null hypersurface defined by observers at  $z = 0$ . This implies that many properties of the objects change across the depth of the survey volume, including the mean density, the amplitude of spatial clustering of dark matter, the bias of luminous objects with respect to mass, and the intrinsic evolution of the absolute magnitude and spectral energy distribution. These aspects should be properly taken into account in order to extract cosmological information from observed samples of redshift surveys.

In order to predict quantitatively the two-point statistics of objects on the light cone, one must take account of (i) nonlinear gravitational evolution, (ii) linear redshift-space distortion, (iii) nonlinear redshift-space distortion, (iv) weighted averaging over the light-cone, (v) cosmological redshift-space distortion due to the geometry of the universe, and (vi) object-dependent clustering bias. The effect (v) comes from our ignorance of the correct cosmological parameters, and (vi) is rather sensitive to the objects which one has in mind. Thus the latter two effects will be discussed in the next subsection.

Nonlinear gravitational evolution of mass density fluctuations is now well

understood, at least for two-point statistics. In practice, we adopt an accurate fitting formula [59] for the nonlinear power spectrum  $P_{\text{nl}}^{\text{R}}(k, z)$  in terms of its linear counterpart. If one assumes a scale-independent deterministic linear bias, furthermore, the power spectrum distorted by the peculiar velocity field is known to be well approximated by the following expression:

$$P^{(\text{S})}(k_{\perp}, k_{\parallel}; z) = b^2(z) P_{\text{mass}}^{(\text{R})}(k; z) \left[ 1 + \beta(z) \left( \frac{k_{\parallel}}{k} \right)^2 \right]^2 D_{\text{vel}}[k_{\parallel} \sigma_{\text{P}}(z)], \quad (131)$$

where  $k_{\perp}$  and  $k_{\parallel}$  are the comoving wavenumber perpendicular and parallel to the line-of-sight of an observer, and  $P_{\text{mass}}^{(\text{R})}(k; z)$  is the mass power spectrum in real space. The second factor in the right-hand-side comes from the linear redshift-space distortion [34], and the last factor is a phenomenological correction for non-linear velocity effect [59]. In the above, we introduce

$$\beta(z) \equiv \frac{1}{b(z)} \frac{d \ln D(z)}{d \ln a} \simeq \frac{1}{b(z)} \left\{ \Omega^{0.6}(z) + \frac{\lambda(z)}{70} \left[ 1 + \frac{\Omega(z)}{2} \right] \right\}. \quad (132)$$

We assume that the pair-wise velocity distribution in real space is approximated by

$$f_v(v_{12}) = \frac{1}{\sqrt{2}\sigma_{\text{P}}} \exp \left( -\frac{\sqrt{2}|v_{12}|}{\sigma_{\text{P}}} \right), \quad (133)$$

with  $\sigma_{\text{P}}$  being the 1-dimensional pair-wise peculiar velocity dispersion. Then the finger-of-god effect is modeled by the damping function,  $D_{\text{vel}}[k_{\parallel} \sigma_{\text{P}}(z)]$ :

$$D_{\text{vel}}[k \mu \sigma_{\text{P}}] = \frac{1}{1 + \kappa^2 \mu^2}, \quad (134)$$

where  $\mu$  is the direction cosine in  $k$ -space, and the dimensionless wavenumber  $\kappa$  is related to the peculiar velocity dispersion  $\sigma_{\text{P}}$  in the physical velocity units:

$$\kappa(z) = \frac{k(1+z)\sigma_{\text{P}}(z)}{\sqrt{2}H(z)}. \quad (135)$$

Since we are mainly interested in the scales around  $1h^{-1}\text{Mpc}$ , we adopt the following fitting formula throughout the analysis below which better approximates the small-scale dispersions in physical units:

$$\sigma_{\text{P}}(z) \sim \begin{cases} 740(1+z)^{-1}\text{km/s} & \text{for SCDM model} \\ 650(1+z)^{-0.8}\text{km/s} & \text{for } \Lambda\text{CDM model.} \end{cases} \quad (136)$$

Integrating equation (131) over  $\mu$ , one obtains the direction-averaged power spectrum in redshift space:

$$\frac{P_{\text{nl}}^{\text{S}}(k, z)}{P_{\text{nl}}^{\text{R}}(k, z)} = A(\kappa) + \frac{2}{3}\beta(z)B(\kappa) + \frac{1}{5}\beta^2(z)C(\kappa) \quad (137)$$

where

$$A(\kappa) = \frac{\arctan(\kappa)}{\kappa}, \quad (138)$$

$$B(\kappa) = \frac{3}{\kappa^2} \left[ 1 - \frac{\arctan(\kappa)}{\kappa} \right], \quad (139)$$

$$C(\kappa) = \frac{5}{3\kappa^2} \left[ 1 - \frac{3}{\kappa^2} + \frac{3\arctan(\kappa)}{\kappa^3} \right]. \quad (140)$$

Adopting those approximations, the direction-averaged correlation functions on the light-cone are finally computed as

$$\xi^{\text{LC}}(x_s) = \frac{\int_{z_{\min}}^{z_{\max}} dz \frac{dV_c}{dz} [\phi(z)n_0(z)]^2 \xi(x_s; z)}{\int_{z_{\min}}^{z_{\max}} dz \frac{dV_c}{dz} [\phi(z)n_0(z)]^2}, \quad (141)$$

where  $z_{\min}$  and  $z_{\max}$  denote the redshift range of the survey, and

$$\xi(x_s; z) \equiv \frac{1}{2\pi^2} \int_0^\infty P_{\text{nl}}^S(k, z) \frac{\sin kx_s}{kx_s} k^2 dk. \quad (142)$$

Throughout the present analysis, we assume a standard Robertson – Walker metric of the form:

$$ds^2 = -dt^2 + a(t)^2 \{d\chi^2 + S_K(\chi)^2 [d\theta^2 + \sin^2 \theta d\phi^2]\}, \quad (143)$$

where  $S_K(\chi)$  is determined by the sign of the curvature  $K$  as

$$S_K(\chi) = \begin{cases} \sin(\sqrt{K}\chi)/\sqrt{K} & (K > 0) \\ \chi & (K = 0) \\ \sinh(\sqrt{-K}\chi)/\sqrt{-K} & (K < 0) \end{cases}, \quad (144)$$

where the present scale factor  $a_0$  is normalized as unity, and the spatial curvature  $K$  is given as (eq.[13])

$$K = H_0^2(\Omega_m + \Omega_\Lambda - 1). \quad (145)$$

The radial comoving distance  $\chi(z)$  is computed by

$$\chi(z) = \int_t^{t_0} \frac{dt}{a(t)} = \int_0^z \frac{dz}{H(z)}. \quad (146)$$

The comoving angular diameter distance  $D_c(z)$  at redshift  $z$  is equivalent to  $S^{-1}(\chi(z))$ , and, in the case of  $\Omega_\Lambda = 0$ , is explicitly given by Mattig's formula:

$$D_c(z) = \frac{1}{H_0} \frac{z}{1+z} \frac{1+z+\sqrt{1+\Omega_m z}}{1+\Omega_m z/2+\sqrt{1+\Omega_m z}}. \quad (147)$$

Then  $dV_c/dz$ , the comoving volume element per unit solid angle, is explicitly given as

$$\begin{aligned}\frac{dV_c}{dz} &= S_K^2(\chi) \frac{d\chi}{dz} \\ &= \frac{S_K^2(\chi)}{H_0 \sqrt{\Omega_m(1+z)^3 + (1-\Omega_m-\Omega_\Lambda)(1+z)^2 + \Omega_\Lambda}}.\end{aligned}\quad (148)$$

## 5.2 Evaluating two-point correlation functions from N-body simulation data

The theoretical modeling described above was tested against simulation results by Hamana, Colombi & Suto (2001) [24]. Using cosmological  $N$ -body simulations in SCDM and  $\Lambda$ CDM models, we generated light-cone samples as follows; first, we adopt a distance observer approximation and assume that the line-of-sight direction is parallel to  $Z$ -axis regardless with its  $(X, Y)$  position. Second, we periodically duplicate the simulation box along the  $Z$ -direction so that at a redshift  $z$ , the position and velocity of those particles locating within an interval  $\chi(z) \pm \Delta\chi(z)$  are dumped, where  $\Delta\chi(z)$  is determined by the output time-interval of the original  $N$ -body simulation. Finally we extract five independent (non-overlapping) cone-shape samples with the angular radius of 1 degree (the field-of-view of  $\pi$  degree<sup>2</sup>). In this manner, we have generated mock data samples on the light-cone continuously extending up to  $z = 0.4$  (relevant for galaxy samples) and  $z = 2.0$  (relevant for QSO samples), respectively from the small and large boxes.

Two-point correlation function is estimated by the conventional pair-count adopting the following estimator [39]:

$$\xi(x) = \frac{DD(x) - 2DR(x) + RR(x)}{RR(x)}.\quad (149)$$

The comoving separation  $x_{12}$  of two objects located at  $z_1$  and  $z_2$  with an angular separation  $\theta_{12}$  is given by

$$\begin{aligned}x_{12}^2 &= x_1^2 + x_2^2 - Kx_1^2x_2^2(1 + \cos^2\theta_{12}) \\ &\quad - 2x_1x_2\sqrt{1 - Kx_1^2}\sqrt{1 - Kx_2^2}\cos\theta_{12},\end{aligned}\quad (150)$$

where  $x_1 \equiv D_c(z_1)$  and  $x_2 \equiv D_c(z_2)$ .

In redshift space, the observed redshift  $z_{\text{obs}}$  for each object differs from the “real” one  $z_{\text{real}}$  due to the velocity distortion effect:

$$z_{\text{obs}} = z_{\text{real}} + (1 + z_{\text{real}})v_{\text{pec}},\quad (151)$$

where  $v_{\text{pec}}$  is the line of sight relative peculiar velocity between the object and the observer in *physical* units. Then the comoving separation  $s_{12}$  of two objects

in redshift space is computed as

$$\begin{aligned} s_{12}^2 &= s_1^2 + s_2^2 - K s_1^2 s_2^2 (1 + \cos^2 \theta_{12}) \\ &\quad - 2s_1 s_2 \sqrt{1 - K s_1^2} \sqrt{1 - K s_2^2} \cos \theta_{12}, \end{aligned} \quad (152)$$

where  $s_1 \equiv D_c(z_{\text{obs},1})$  and  $s_2 \equiv D_c(z_{\text{obs},2})$ .

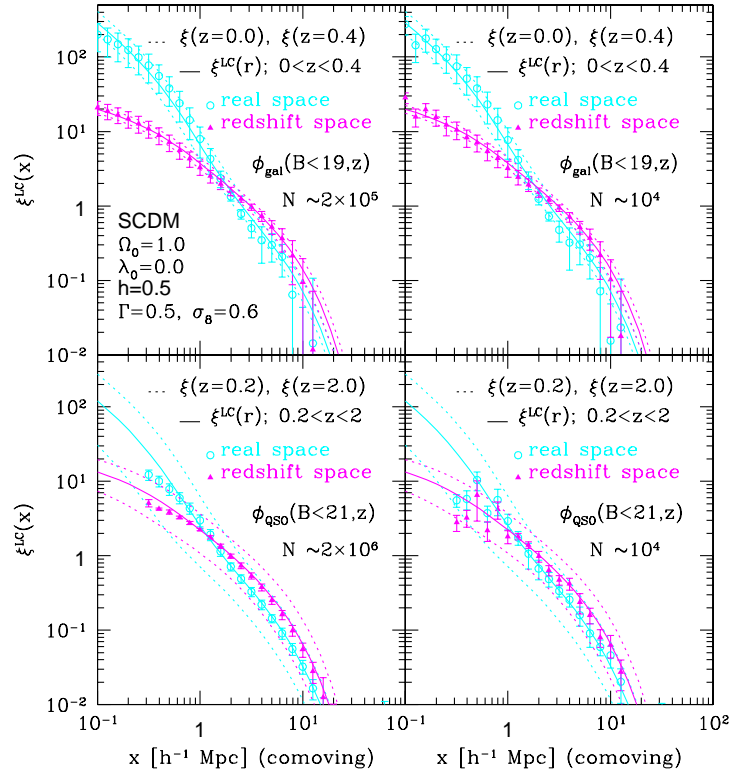


Figure 14: Mass two-point correlation functions on the light cone for particles with redshift-dependent selection functions in SCDM model. *Upper:*  $z < 0.4$ , *Lower:*  $0.2 < z < 2.0$ . *Left:* with selection function whose shape is the same as that of the B-band magnitude limit of 19 for galaxies (upper) and 21 for QSOs (lower). *Right:* randomly selected  $N \sim 10^4$  particles from the particles in the left results. (ref. [24])

In properly predicting the power spectra on the light cone, the selection function should be specified. For galaxies, we adopt a B-band luminosity function of the APM galaxies fitted to the Schechter function [40]. For quasars, we

adopt the B-band luminosity function from the 2dF QSO survey data [7]. To compute the B-band apparent magnitude from a quasar of absolute magnitude  $M_B$  at  $z$  (with the luminosity distance  $d_L(z)$ ), we applied the K-correction:

$$B = M_B + 5 \log(d_L(z)/10\text{pc}) - 2.5(1-p) \log(1+z) \quad (153)$$

for the quasar energy spectrum  $L_\nu \propto \nu^{-p}$  (we use  $p = 0.5$ ). In practice, we adopt the galaxy selection function  $\phi_{\text{gal}}(< B_{\text{lim}}, z)$  with  $B_{\text{lim}} = 19$  and  $z_{\text{min}} = 0.01$  for the small box realizations, while the QSO selection function  $\phi_{\text{QSO}}(< B_{\text{lim}}, z)$  with  $B_{\text{lim}} = 21$  and  $z_{\text{min}} = 0.2$  for the large box realizations. We do not introduce the spatial biasing between selected particles and the underlying dark matter.

Figures 14 and 15 plot the two-point correlation functions in SCDM and  $\Lambda$ CDM, respectively, taking account of the selection functions. It is clear that the simulation results and the predictions are in good agreement.

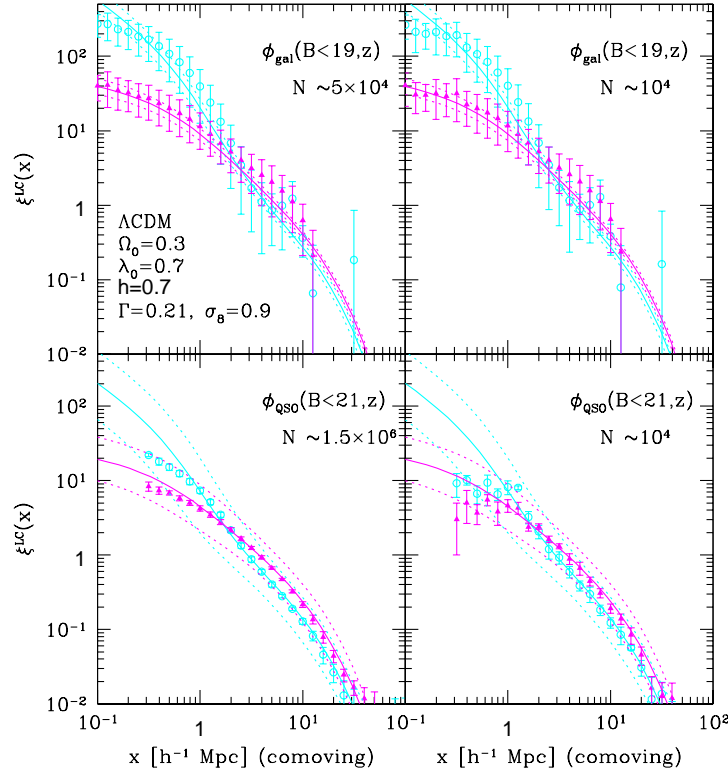


Figure 15: Same as Figure 14 but for  $\Lambda$ CDM model. (ref. [24])

### 5.3 Cosmological redshift-space distortion

Consider a spherical object at high redshift. If the wrong cosmology is assumed in interpreting the distance-redshift relation along the line of sight and in the transverse direction, the sphere will appear distorted. Alcock & Paczynski (1979) [2] pointed out that this curvature effect could be used to estimate the cosmological constant. Matsubara & Suto (1996) [47] and Ballinger, Peacock & Heavens (1996) [3] developed a theoretical framework to describe the geometrical distortion effect (cosmological redshift distortion) in the two-point correlation function and the power spectrum of distant objects, respectively. Certain studies were less optimistic than others about the possibility of measuring this AP effect. For example, Ballinger, Peacock and Heavens (1996) argued that the geometrical distortion could be confused with the dynamical redshift distortions caused by peculiar velocities and characterized by the linear theory parameter  $\beta \equiv \frac{\Omega_m^{0.6}}{b}$ . Matsubara & Szalay (2002, 2003) [49, 50] showed that the typical SDSS and 2dF samples of normal galaxies at low redshift ( $\sim 0.1$ ) have sufficiently low signal-to-noise, but they are too shallow to detect the A-P effect. On the other hand, the quasar SDSS and 2dFGRS surveys are at a useful redshift, but they are too sparse. A more promising sample is the SDSS Luminous Red Galaxies survey (out to redshift  $z \sim 0.5$ ) which turns out to be optimal in terms of both depth and density.

While this analysis is promising, it remains to be tested if non-linear clustering and complicated biasing (which is quite plausible for red galaxies) would not ‘contaminate’ the measurement of the Equation of State. Even if the A-P test turns out to be less accurate than other cosmological tests (e.g., CMB and SN Ia) the effect itself is an interesting and important ingredient in analyzing the clustering pattern of galaxies at high redshifts. We shall now present the formalism for this effect.

Due to a general-relativistic effect through the geometry of the universe, the *observable* separations perpendicular and parallel to the line-of-sight direction,  $x_{s\perp} = (c/H_0)z\delta\theta$  and  $x_{s\parallel} = (c/H_0)\delta z$ , are mapped differently to the corresponding comoving separations in real space  $x_\perp$  and  $x_\parallel$ :

$$x_{s\perp}(z) = x_\perp cz/[H_0(1+z)d_A(z)] \equiv x_\perp/c_\perp(z), \quad (154)$$

$$x_{s\parallel}(z) = x_\parallel H(z)/H_0 \equiv x_\parallel/c_\parallel(z), \quad (155)$$

with  $d_A(z)$  being the angular diameter distance. The difference between  $c_\perp(z)$  and  $c_\parallel(z)$  generates an apparent anisotropy in the clustering statistics, which should be isotropic in the comoving space. Then the power spectrum in cosmological redshift space,  $P^{(\text{CRD})}$ , is related to  $P^{(\text{S})}$  defined in the *comoving* redshift space as

$$P^{(\text{CRD})}(k_{s\perp}, k_{s\parallel}; z) = \frac{1}{c_\perp(z)^2 c_\parallel(z)} P^{(\text{S})} \left( \frac{k_{s\perp}}{c_\perp(z)}, \frac{k_{s\parallel}}{c_\parallel(z)}; z \right), \quad (156)$$

where the first factor comes from the Jacobian of the volume element  $dk_{s\perp}^2 dk_{s\parallel}$ , and  $k_{s\perp} = c_\perp(z)k_\perp$  and  $k_{s\parallel} = c_\parallel(z)k_\parallel$  are the wavenumber perpendicular and parallel to the line-of-sight direction.

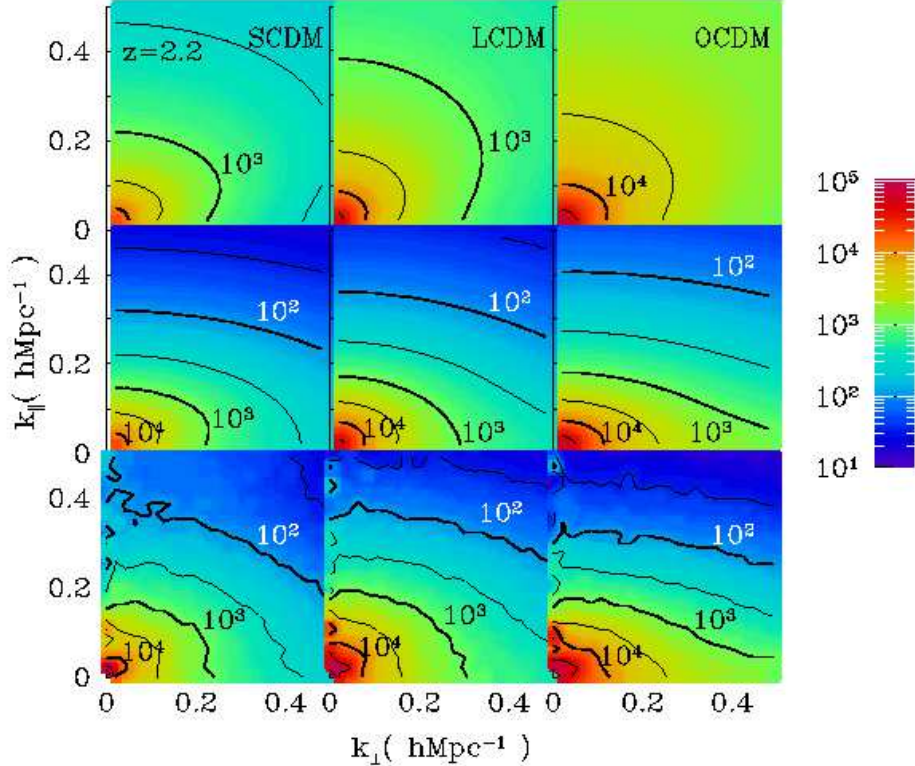


Figure 16: Two-dimensional power spectra in cosmological redshift space at  $z = 2.2$ . (ref. [42])

Using equation (131), equation (156) reduces to

$$\begin{aligned} P^{(\text{CRD})}(k_s, \mu_k; z) &= \frac{b^2(z)}{c_\perp(z)^2 c_\parallel(z)} P_{\text{mass}}^{(\text{R})} \left( \frac{k_s}{c_\perp(z)} \sqrt{1 + \left[ \frac{1}{\eta(z)^2} - 1 \right] \mu_k^2}; z \right) \\ &\times \left\{ 1 + \left[ \frac{1}{\eta(z)^2} - 1 \right] \mu_k^2 \right\}^{-2} \left\{ 1 + \left[ \frac{1 + \beta(z)}{\eta(z)^2} - 1 \right] \mu_k^2 \right\}^2 \left[ 1 + \frac{k_s^2 \mu_k^2 \sigma_p^2}{2 c_\parallel^2(z)} \right]^{-1}, \end{aligned} \quad (157)$$

where

$$k_s \equiv \sqrt{k_{s\perp}^2 + k_{s\parallel}^2}, \quad \mu_k \equiv k_{s\parallel}/k_s, \quad \eta \equiv c_\parallel/c_\perp. \quad (158)$$

Figure 16 shows anisotropic power spectra  $P^{(\text{CRD})}(k_s, \mu_k; z = 2.2)$ . As specific examples, we consider SCDM, LCDM and OCDM models, which have  $(\Omega_m, \Omega_\Lambda, h, \sigma_8) = (1.0, 0.0, 0.5, 0.6)$ ,  $(0.3, 0.7, 0.7, 1.0)$ , and  $(0.3, 0.0, 0.7, 1.0)$ , respectively. Clearly the linear theory predictions ( $\sigma_p = 0$ ; top panels) are quite different from the results of N-body simulations (bottom panels), indicating the importance of the nonlinear velocity effects ( $\sigma_p$  computed according to ref. [51]; middle panels).

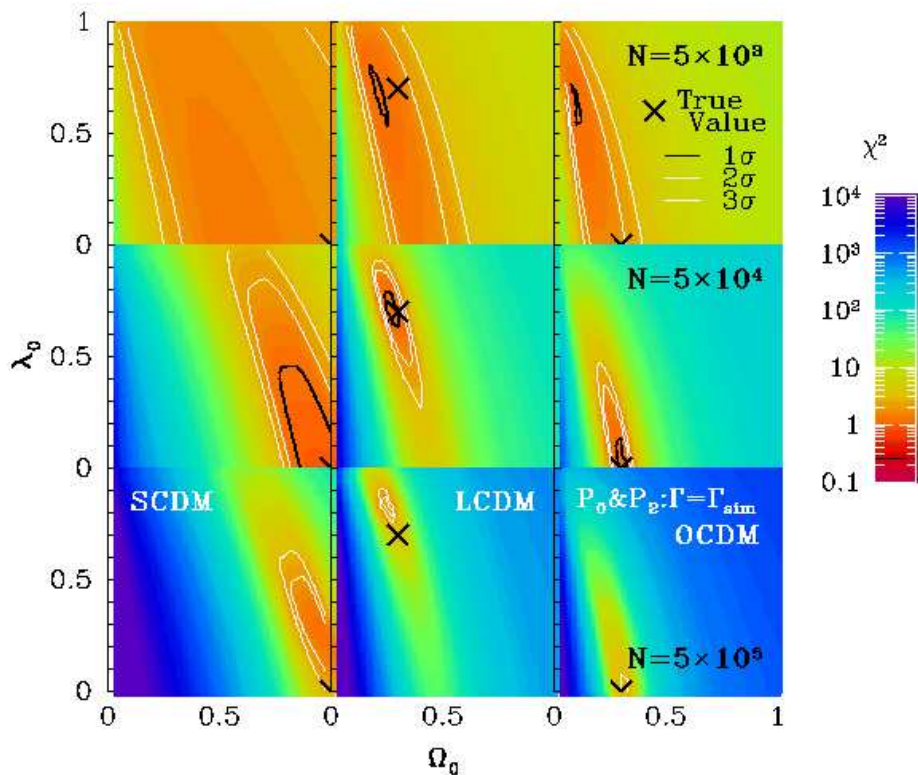


Figure 17: The confidence contours on  $\Omega_m$ - $\Omega_\Lambda$  plane from the  $\chi^2$ -analysis of the monopole and quadrupole moments of the power spectrum in the cosmological redshift space at  $z = 2.2$ . We randomly selected  $N = 5 \times 10^3$  (upper panels),  $N = 5 \times 10^4$  (middle panels), and  $N = 5 \times 10^5$  (lower panels) particles from N-body simulation. The value of  $\sigma_8$  is adopted from the cluster abundance. (ref. [42])

Next we decompose the power spectrum into harmonics:

$$P(k, \mu_k; z) = \sum_{l:\text{even}} P_l(k) L_l(\mu_k), \quad P_l(k; z) \equiv \frac{2l+1}{2} \int_{-1}^1 d\mu_k P(k, \mu_k; z) L_l(\mu_k) \quad (159)$$

where  $L_l(\mu_k)$  are the  $l$ -th order Legendre polynomials. Similarly, the two-point correlation function is decomposed as

$$\xi(x, \mu_x; z) = \sum_{l:\text{even}} \xi_l(x) L_l(\mu_x), \quad \xi_l(x; z) \equiv \frac{2l+1}{2} \int_{-1}^1 d\mu_x \xi(x, \mu_x; z) L_l(\mu_x) \quad (160)$$

using the direction cosine,  $\mu_x$ , between the separation vector and the line-of-sight. The above multipole moments satisfy the following relations:

$$\xi_l(x; z) = \frac{1}{2\pi^2 i^l} \int_0^\infty P_l(k; z) j_l(kx) k^2 dk, \quad (161)$$

$$P_l(k; z) = 4\pi i^l \int_0^\infty \xi_l(x; z) j_l(kx) x^2 dx, \quad (162)$$

with  $j_l(kx)$  being spherical Bessel functions. Substituting  $P^{(\text{CRD})}(k_s, \mu_k; z)$  in equation (159) yields  $P_l^{(\text{CRD})}(k_s; z)$ , and then  $\xi^{(\text{CRD})}(\mathbf{x}_s; z)$  can be computed from equation (161).

Comparison of the monopoles and quadrupoles from simulations and model predictions exhibits how the results are sensitive to the cosmological parameters, which in turn may put potentially useful constraints on  $(\Omega_m, \Omega_\Lambda)$ . Figure 17 indicates the feasibility, which interestingly results in a constraint fairly orthogonal to that from the Supernovae Ia Hubble diagram.

## 5.4 Two-Point Clustering Statistics on a Light-Cone in Cosmological Redshift Space

In order to explore the relation between the two-point statistics on a constant-time hypersurface in real space and that on a light-cone hypersurface in cosmological redshift space, we simply consider the case of the deterministic, linear, and scale-independent bias:

$$\delta(\mathbf{x}, z) = b(z) \delta_m(\mathbf{x}, z). \quad (163)$$

In what follows, we explicitly use the subscript, mass, to indicate the quantities related to the mass density field, and those without the subscript correspond to objects satisfying equation (163).

Using equation (157), the two-point correlation function in the cosmological redshift space,  $\xi^{(\text{CRD})}(x_{s\perp}, x_{s\parallel}; z)$ , is computed as

$$\xi^{(\text{CRD})}(\mathbf{x}_s; z) = \frac{1}{(2\pi)^3} \int P^{(\text{CRD})}(\mathbf{k}_s; z) \exp(-i\mathbf{k}_s \cdot \mathbf{x}_s) d^3 k_s$$

$$\begin{aligned}
&= \frac{1}{(2\pi)^3} \int P^{(S)}(\mathbf{k}; z) \exp(-i\mathbf{k} \cdot \mathbf{x}) d^3k \\
&= \xi^{(S)}(c_{\perp}x_{s\perp}, c_{\parallel}x_{s\parallel}; z),
\end{aligned} \tag{164}$$

where  $\xi^{(S)}(x_{\perp}, x_{\parallel}; z)$  is the redshift-space correlation function defined through equation (131).

Since  $P_l^{(\text{CRD})}(k_s; z)$  and  $\xi_l^{(\text{CRD})}(x_s; z)$  are defined in redshift space, the proper weight should be

$$d^3s^{(\text{CRD})} [\phi(z)n_0^{\text{CRD}}(z)]^2 = d^3x[\phi(z)n_0^{\text{com}}(z)]^2 c_{\perp}(z)^2 c_{\parallel}(z), \tag{165}$$

where  $n_0^{\text{CRD}}(z)$  and  $n_0^{\text{com}}(z)$  denote the number densities of the objects in cosmological redshift space and comoving space, respectively, and  $\phi(z)$  is the selection function determined by the observational target selection and the luminosity function of the objects. Then, the final expressions [76] reduce to

$$P_l^{(\text{LC,CRD})}(k_s) = \frac{\int_{z_{\min}}^{z_{\max}} dz \frac{dV_c}{dz} [\phi(z)n_0^{\text{com}}(z)]^2 c_{\perp}(z)^2 c_{\parallel}(z) P_l^{(\text{CRD})}(k_s; z)}{\int_{z_{\min}}^{z_{\max}} dz \frac{dV_c}{dz} [\phi(z)n_0^{\text{com}}(z)]^2 c_{\perp}(z)^2 c_{\parallel}(z)} \tag{166}$$

$$\xi_l^{(\text{LC,CRD})}(x_s) = \frac{\int_{z_{\min}}^{z_{\max}} dz \frac{dV_c}{dz} [\phi(z)n_0^{\text{com}}(z)]^2 c_{\perp}(z)^2 c_{\parallel}(z) \xi_l^{\text{CRD}}(x_s; z)}{\int_{z_{\min}}^{z_{\max}} dz \frac{dV_c}{dz} [\phi(z)n_0^{\text{com}}(z)]^2 c_{\perp}(z)^2 c_{\parallel}(z)}, \tag{167}$$

where  $z_{\min}$  and  $z_{\max}$  denote the redshift range of the survey,  $dV_c/dz = d_c^2(z)/H(z)$  is the comoving volume element per unit solid angle.

Note that  $k_s$  and  $x_s$ , defined in  $P_l^{(\text{CRD})}(k_s; z)$  and  $\xi_l^{\text{CRD}}(x_s; z)$ , are related to their comoving counterparts at  $z$  through equations (158) and (154), while those in  $P_l^{(\text{LC,CRD})}(k_s)$  and  $\xi_l^{(\text{LC,CRD})}(x_s)$  are not specifically related to any comoving wavenumber and separation. Rather, they correspond to the quantities averaged over the range of  $z$  satisfying the observable conditions  $x_s = (c/H_0)\sqrt{\delta z^2 + z^2\delta\theta^2}$  and  $k_s = 2\pi/x_s$ .

Let us show specific examples of the two-point clustering statistics on a light-cone in cosmological redshift space. We consider SCDM and LCDM models, and take into account the selection functions relevant to the upcoming SDSS spectroscopic samples of galaxies and quasars by adopting the  $B$ -band limiting magnitudes of 19 and 20, respectively.

Figure 18 compares the predictions for the angle-averaged (monopole) power spectra under various approximations. The upper and lower panels adopt the selection functions appropriate for galaxies in  $0 < z < z_{\max} = 0.2$  and QSOs in  $0 < z < z_{\max} = 5$ , respectively. The left and right panels present the results in SCDM and LCDM models. For simplicity we adopt a scale-independent linear

bias model [20]:

$$b(z) = 1 + \frac{1}{D(z)}[b(k, z = 0) - 1], \quad (168)$$

with  $b(k, z = 0) = 1$  and 1.5 for galaxies and quasars, respectively.

The upper and lower panels correspond to magnitude-limited samples of galaxies ( $B < 19$  in  $0 < z < z_{\max} = 0.2$ ; no bias model) and QSOs ( $B < 20$  in  $0 < z < z_{\max} = 5$ ; Fry's linear bias model), respectively. We present the results normalized by the real-space power spectrum in linear theory  $P^{(\text{R,lin})}(k; z)$  [4], and  $P_0^{(\text{S})}(k; z = 0)$ ,  $P_0^{(\text{S})}(k; z = z_{\max})$ ,  $P_0^{(\text{CRD})}(k_s; z = z_{\max})$ , and  $P_0^{(\text{LC,CRD})}(k_s)$  are computed using the nonlinear power spectrum [59].

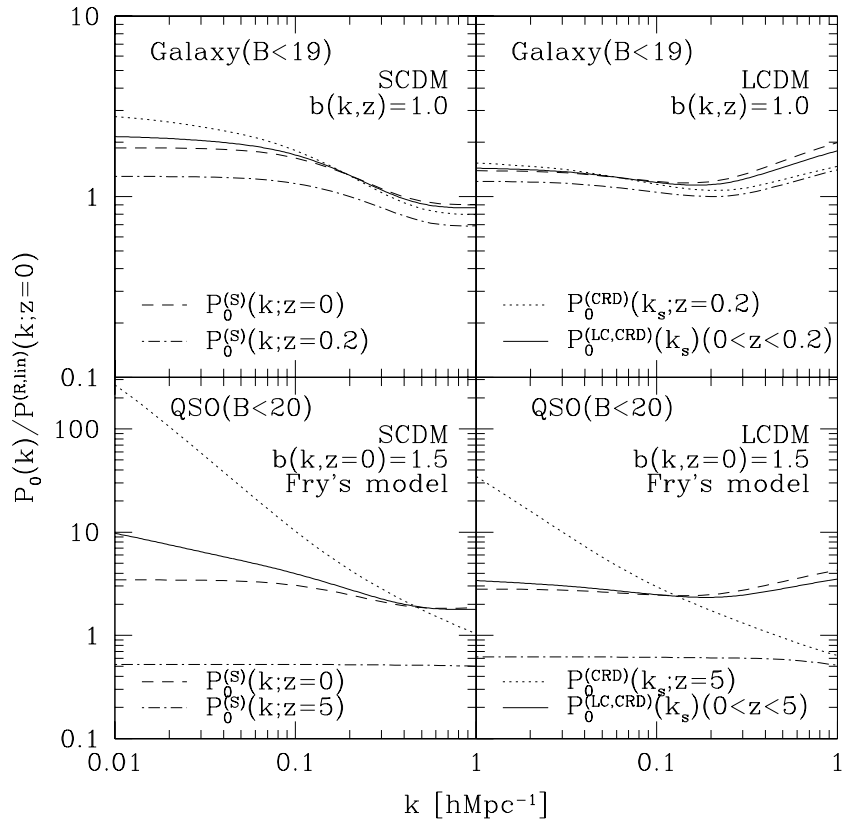


Figure 18: Light-cone and cosmological redshift-space distortion effects on angle-averaged power spectra. (ref. [76])

Consider first the results for the galaxy sample (upper panels). On linear

scales ( $k < 0.1h \text{ Mpc}^{-1}$ ),  $P_0^{(\text{S})}(k; z = 0)$  plotted in dashed lines is enhanced relative to that in real space, mainly due to a linear redshift-space distortion [the Kaiser factor in equation (131)]. For nonlinear scales, the nonlinear gravitational evolution increases the power spectrum in real space, while the finger-of-god effect suppresses that in redshift space. Thus, the net result is sensitive to the shape and the amplitude of the fluctuation spectrum, itself; in the LCDM model that we adopted, the nonlinear gravitational growth in real space is stronger than the suppression due to the finger-of-god effect. Thus,  $P_0^{(\text{S})}(k; z = 0)$  becomes larger than its real-space counterpart in linear theory. In the SCDM model, however, this is opposite and  $P_0^{(\text{S})}(k; z = 0)$  becomes smaller.

The power spectra at  $z = 0.2$  (dash-dotted lines) are smaller than those at  $z = 0$  by the corresponding growth factor of the fluctuations, and one might expect that the amplitude of the power spectra on the light-cone (solid lines) would be in-between the two. While this is correct, if we use the comoving wavenumber, the actual observation on the light-cone in the cosmological redshift space should be expressed in terms of  $k_s$  [equation (158)]. If we plot the power spectra at  $z = 0.2$  taking into account the geometrical distortion,  $P_0^{(\text{CRD})}(k_s; z = 0.2)$  in the dotted lines becomes significantly larger than  $P_0^{(\text{S})}(k; z = 0.2)$ . Therefore,  $P_0^{(\text{LC,CRD})}(k_s)$  should take a value between those of  $P_0^{(\text{CRD})}(k_s; z = 0) = P_0^{(\text{S})}(k; z = 0)$  and  $P_0^{(\text{CRD})}(k_s; z = 0.2)$ . This explains the qualitative features shown in the upper panels of Figure 18. As a result, both the cosmological redshift-space distortion and the light-cone effect substantially change the predicted shape and amplitude of the power spectra, even for the galaxy sample [54]. The results for the QSO sample can be basically understood in a similar manner, except that the evolution of the bias makes a significant difference, since the sample extends to much higher redshifts.

Figure 19 shows the results for the angle-averaged (monopole) two-point correlation functions, exactly corresponding to those in Figure 18. The results in this figure can also be understood by an analogy of those presented in Figure 18 at  $k \sim 2\pi/x$ . Unlike the power spectra, however, two-point correlation functions are not positive definite. The funny features in Figure 19 on scales larger than  $30h^{-1}\text{Mpc}$  ( $100h^{-1}\text{Mpc}$ ) in SCDM (LCDM) originate from the fact that  $\xi^{(\text{R,lin})}(x, z = 0)$  becomes negative there.

In fact, since the resulting predictions are sensitive to the bias, which is unlikely to quantitatively be specified by theory, the present methodology will find two completely different applications. For relatively shallower catalogues, like galaxy samples, the evolution of bias is not supposed to be so strong. Thus, one may estimate the cosmological parameters from the observed degree of the redshift distortion, as has been conducted conventionally. Most importantly, we can correct for the systematics due to the light-cone and geometrical distortion effects, which affect the estimate of the parameters by  $\sim 10\%$ . Alternatively, for deeper catalogues like high-redshift quasar samples, one can extract information on the object-dependent bias only by correcting the observed data on the basis

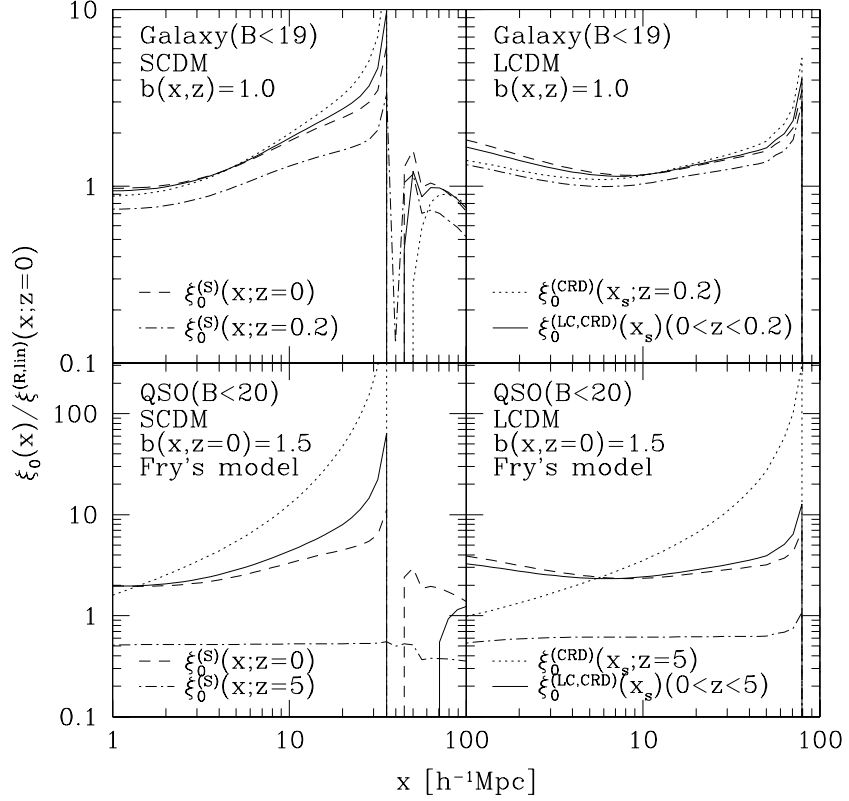


Figure 19: Same as Figure 18 on angle-averaged two-point correlation functions. (ref. [76])

of our formulae.

In a sense, the former approach uses the light-cone and geometrical distortion effects as real cosmological signals, while the latter regards them as inevitable, but physically removable, noise. In both cases, the present methodology is important in properly interpreting the observations of the universe at high redshifts.

## 6 Recent results from 2dF and SDSS

### 6.1 The latest galaxy redshift surveys

Redshifts surveys in the 1980s and the 1990s (e.g the CfA, IRAS and Las campanas surveys) measured thousands to tens of thousands galaxy redshifts. Multifibre technology now allows us to measure redshifts of millions of galaxies. Below we summarize briefly the properties of the main new surveys, 2dFGRS, SDSS, 6dF, VIRMOS, DEEP2 and we discuss key results from 2dFGRS and SDSS. Further analysis of these surveys is currently underway.

#### 6.1.1 The 2dF galaxy redshift survey

The Anglo-Australian 2 degree Field Galaxy Redshift (2dFGRS)<sup>1</sup> has recently been completed with redshifts for 230,000 galaxies selected from the APM catalogue (December 2002) down to an extinction corrected magnitude limit of  $b_J < 19.45$ . The main survey regions are two declination strips, in the northern and southern Galactic hemispheres, and also 100 random fields, covering in total about 1800 deg<sup>2</sup> (Figs. 20 and 21). The median redshift of the 2dFGRS is  $\bar{z} \sim 0.1$  (see refs. [11, 61] for reviews).

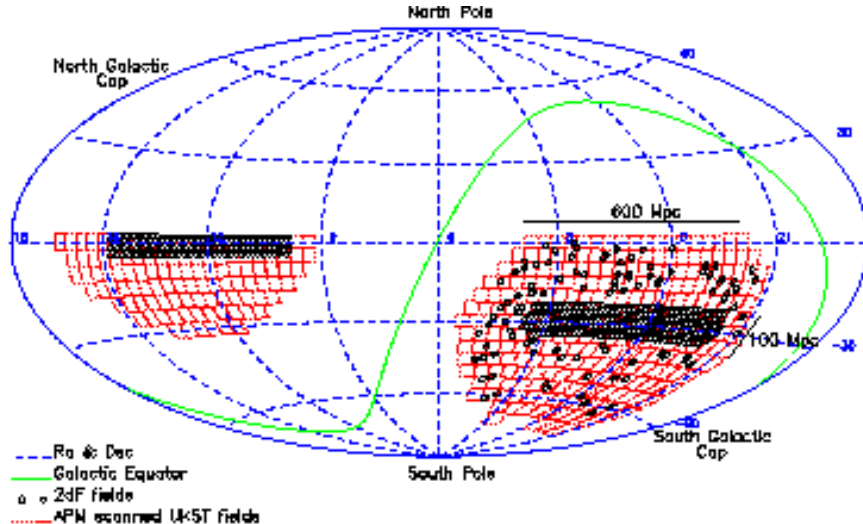


Figure 20: The 2dFGRS fields (small circles) superimposed on the APM catalogue area (dotted outlines of Sky Survey plates).

<sup>1</sup><http://www.mso.anu.edu.au/2dFGRS/>

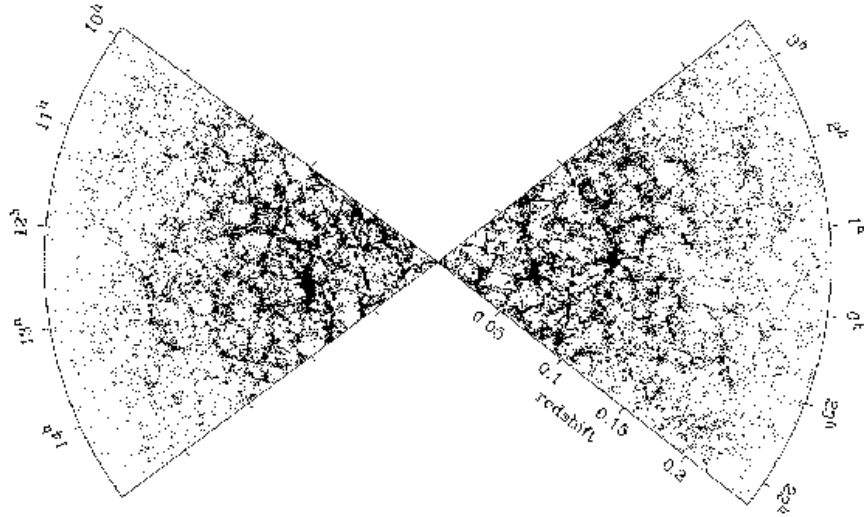


Figure 21: The distribution of 63,000 2dFGRS galaxies in the NGP (*Left*) and SGP (*Right*) strips.

### 6.1.2 The SDSS galaxy redshift survey

The SDSS (Sloan Digital Sky Survey) is a US-Japan-Germany joint project to image a quarter of the Celestial Sphere at high Galactic latitude as well as to obtain spectra of galaxies and quasars from the imaging data<sup>2</sup>. The dedicated 2.5 meter telescope at Apache Point Observatory is equipped with a multi-CCD camera with five broad bands centered at 3561, 4676, 6176, 7494, and 8873 Å. For further details of SDSS, see refs. [84, 73]

The latest map of the SDSS galaxy distribution, together with a typical slice, are shown in Figures 22, and 23 [27]. The three-dimensional map centered on us in equatorial coordinate system is shown Figure 22. Redshift slices of galaxies centered around the equatorial plane with various redshift limits and thicknesses of planes are shown in Figure 23:  $z < 0.05$  with thickness of  $10h^{-1}\text{Mpc}$  centered around the equatorial plane in the upper-left panel;  $z < 0.1$  with thickness of  $15h^{-1}\text{Mpc}$  in the upper-right panel;  $z < 0.2$  with thickness of  $20h^{-1}\text{Mpc}$  in the lower panel.

---

<sup>2</sup><http://www.sdss.org/>

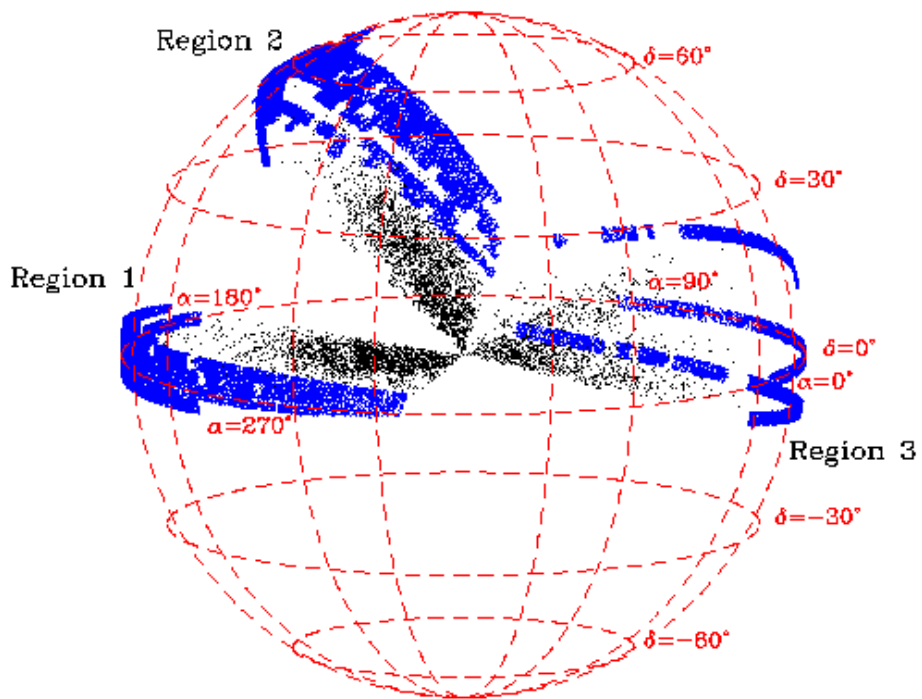


Figure 22: 3D redshift-space map centered on us, and its projection on the celestial sphere of SDSS galaxy subset, including the three main regions. (ref. [27])

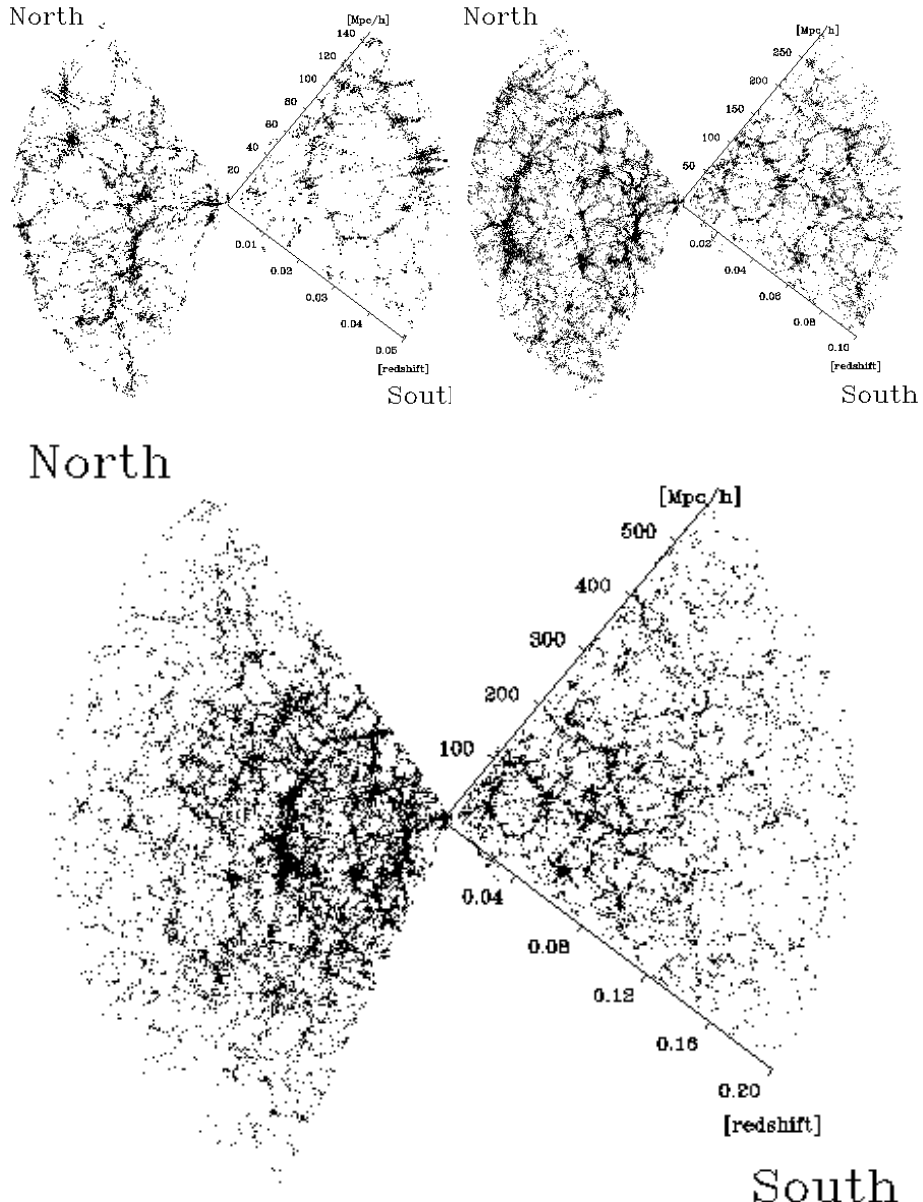


Figure 23: Redshift slices of SDSS galaxy data around the equatorial plane. The redshift limits and the thickness of the planes are: *Upper-left*  $z < 0.05$ ,  $10h^{-1}\text{Mpc}$ ; *Upper-right*  $z < 0.1$ ,  $15h^{-1}\text{Mpc}$ ; *Lower*  $z < 0.2$ ,  $20h^{-1}\text{Mpc}$ . The size of points has been adjusted. Note that the data for the Southern part are sparser than those for the Northern part, especially for thick slices. (ref. [27])

### 6.1.3 The 6dF galaxy redshift survey

The 6dF (6-degree Field)<sup>3</sup> is a survey of redshifts and peculiar velocities of galaxies selected primarily in the Near Infrared from new 2MASS (Two Micron All Sky Survey) catalogue<sup>4</sup>. One goal is to measure redshifts of more than 170,000 galaxies over nearly the whole Southern sky. Another exciting aim of the survey is to measure peculiar velocities (using 2MASS photometry and 6dF velocity dispersions) of about 15,000 galaxies out to  $150h^{-1}\text{Mpc}$ . The high quality data of this survey could revive peculiar velocities as a cosmological probe (which was very popular about 10-15 years ago). Observations have so far obtained nearly 40,000 redshifts and completion is expected in 2005.

### 6.1.4 The DEEP galaxy redshift survey

The DEEP survey is a two-phased project using the Keck telescopes to study the properties and distribution of high redshift galaxies<sup>5</sup>. Phase 1 used the LRIS spectrograph to study a sample of 1000 galaxies to a limit of  $I=24.5$ . Phase 2 of the DEEP project will use the new DEIMOS spectrograph to obtain spectra of 65,000 faint galaxies with redshifts  $z \sim 1$ . The scientific goals are to study the evolution of properties of galaxies and the evolution of the clustering of galaxies compared to samples at low redshift. The survey is designed to have the fidelity of local redshift surveys such as the LCRS survey, and to be complementary to ongoing large redshift surveys such as the SDSS project and the 2dF survey. The DEIMOS/DEEP or DEEP2 survey will be executed with resolution  $R = 4000$ , and we therefore expect to measure linewidths and rotation curves for a substantial fraction of the target galaxies. DEEP2 will thus also be complementary to the VLT/VIRMOS project, which will survey more galaxies in a larger region of the sky but with much lower spectral resolution and with fewer objects at high redshift.

### 6.1.5 The VIRMOS galaxy redshift survey

The on-going Franco-Italian VIRMOS project<sup>6</sup> has delivered the VIMOS spectrograph for the European Southern Observatory Very Large Telescope (ESO-VLT). VIMOS is a VIable imaging Multi-Object Spectrograph with outstanding multiplex capabilities: with 10 arcsec slits, spectra can be taken of 600 objects simultaneously. In integral field mode, a 6400-fibre Integral Field Unit (IFU) provides spectroscopy for all objects covering a  $54 \times 54 \text{ arcsec}^2$  area. VIMOS therefore provides unsurpassed efficiency for large surveys. The VIRMOS project consists of: Construction of VIMOS, and a Mask Manufacturing Unit for the ESO-VLT. The VIRMOS-VLT Deep Survey (VVDS), a comprehensive

<sup>3</sup><http://www.mso.anu.edu.au/6dFGS/>

<sup>4</sup><http://www.ipac.caltech.edu/2mass/>

<sup>5</sup><http://deep.berkeley.edu/~marc/deep/>

<sup>6</sup><http://www.astrsp-mrs.fr/virmos/>

imaging and redshift survey of the deep universe based on more than 150,000 redshifts in four 4 sq.-degree fields.

## 6.2 Cosmological parameters from 2dFGRS

### 6.2.1 The Power spectrum of 2dF Galaxies on large scales

An initial estimate of the convolved, redshift-space power spectrum of the 2dFGRS was determined by Percival et al. (2002) [66] for a sample of 160,000 redshifts. On scales  $0.02h/\text{Mpc} < k < 0.15h/\text{Mpc}$ , the data are fairly robust and the shape of the power spectrum is not significantly affected by redshift-space distortion or non-linear effects, while its overall amplitude is increased due to the linear redshift-space distortion effect (see §5).

If one fits the  $\Lambda$ -CDM model predictions to the 2dFGRS power spectrum (Fig. 24) over the above range in  $k$ , one can constrain the cosmological parameters. For instance, assuming a Gaussian prior on the Hubble constant  $h = 0.7 \pm 0.07$  (from ref. [19]), Percival et al. (2002) [66] obtained the 68 percent confidence limits on the shape parameter  $\Omega_m h = 0.20 \pm 0.03$ , and the baryon fraction  $\Omega_b/\Omega_m = 0.15 \pm 0.07$ . For a fixed set of cosmological parameters, i.e.,  $n = 1$ ,  $\Omega_m = 1 - \Omega_\Lambda = 0.3$ ,  $\Omega_b h^{-2} = 0.02$  and  $h = 0.70$ , the rms mass fluctuation amplitude of 2dFGRS galaxies smoothed over a top-hat radius of  $8h^{-1}\text{Mpc}$  in redshift space turned out to be  $\sigma_{8g}^S(L_s, z_s) \approx 0.94$ .

### 6.2.2 An upper limit on neutrino masses

The recent results of atmospheric and solar neutrino oscillations [21, 1] imply non-zero mass-squared differences of the three neutrino flavours. While these oscillation experiments do not directly determine the absolute neutrino masses, a simple assumption of the neutrino mass hierarchy suggests a lower limit on the neutrino mass density parameter,  $\Omega_\nu = m_{\nu, \text{tot}} h^{-2} / (94\text{eV}) \approx 0.001$ . Large scale structure data can put an upper limit on the ratio  $\Omega_\nu/\Omega_m$  due to the neutrino ‘free streaming’ effect [29]. By comparing the 2dF galaxy power-spectrum of fluctuations with a four-component model (baryons, cold dark matter, a cosmological constant and massive neutrinos) it was estimated that  $\Omega_\nu/\Omega_m < 0.13$  (95% CL), or with concordance prior of  $\Omega_m = 0.3$ ,  $\Omega_\nu < 0.04$ , or an upper limit of  $\sim 2$  eV on the total neutrino mass, assuming a prior of  $h \approx 0.7$  [15, 16] (see Fig. 24). In order to minimize systematic effects due to biasing and non-linear growth, the analysis was restricted to the range  $0.02 < k < 0.15 h \text{Mpc}^{-1}$ . Additional cosmological data sets bring down this upper limit by a factor of 2 [72].

### 6.2.3 Combining 2dFGRS & CMB

While the CMB probes the fluctuations in matter, the galaxy redshift surveys measure the perturbations in the light distribution of particular tracer (e.g.

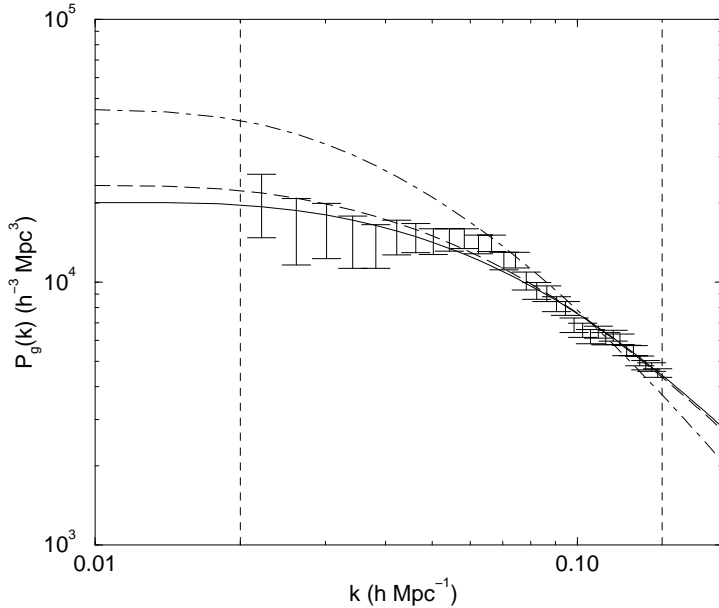


Figure 24: The power spectrum of the 2dFGRS. The points with error bars show the measured 2dFGRS power spectrum measurements in redshift space, convolved with the window function. Also plotted are linear CDM models with neutrino contribution of  $\Omega_\nu = 0, 0.01$  and  $0.05$  (bottom to top lines). The other parameters are fixed to the concordance model. The good fit of the linear theory power spectrum at  $k > 0.15 h \text{ Mpc}^{-1}$  is due to a conspiracy between the non-linear gravitational growth and the Finger-of-God smearing. (refs. [66, 15])

galaxies of certain type). Therefore, for a fixed set of cosmological parameters, a combination of the two can constrain better cosmological parameters, and it can also provide important information on the way galaxies are ‘biased’ relative to the mass fluctuations,

The CMB fluctuations are commonly represented by the spherical harmonics  $C_\ell$ . The connection between the harmonic  $\ell$  and  $k$  is roughly

$$\ell \simeq k \frac{2c}{H_0 \Omega_m^{0.4}} \quad (169)$$

for a spatially-flat universe. For  $\Omega_m = 0.3$  the 2dFGRS range  $0.02 < k < 0.15 h \text{ Mpc}^{-1}$  corresponds approximately to  $200 < \ell < 1500$ , which is well covered by the recent CMB experiments.

Recent CMB measurements have been used in combination with the 2dF power spectrum. Efstathiou et al. (2002) [17] showed that 2dFGRS+CMB

provide evidence for a positive Cosmological Constant  $\Omega_\Lambda \sim 0.7$  (assuming  $w = -1$ ), independently of the studies of Supernovae Ia. As explained in ref. [66], the shapes of the CMB and the 2dFGRS power spectra are insensitive to Dark Energy. The main important effect of the Dark Energy is to alter the angular diameter distance to the last scattering, and thus the position of the first acoustic peak. Indeed, the latest result from a combination of WMAP with 2dFGRS and other probes gives  $h = 0.71^{+0.04}_{-0.03}$ ,  $\Omega_b h^2 = 0.0224 \pm 0.0009$ ,  $\Omega_m h^2 = 0.135^{+0.008}_{-0.009}$ ,  $\sigma_8 = 0.84 \pm 0.04$ ,  $\Omega_{\text{tot}} = 1.02 \pm 0.02$ , and  $w < -0.78$  (95% CL, assuming  $w \geq -1$ ) [72].

#### 6.2.4 Redshift-space distortion

An independent measurement of cosmological parameters on the basis of 2dFGRS comes from redshift-space distortions on scales  $\lesssim 10 h^{-1} \text{ Mpc}$ ; a correlation function  $\xi(\pi, \sigma)$  in parallel and transverse pair separations  $\pi$  and  $\sigma$ . As described in §5, the distortion pattern is a combination of the coherent infall, parameterized by  $\beta = \Omega_m^{0.6}/b$  and random motions modelled by an exponential velocity distribution function (eq.[133]). This methodology has been applied by many authors. For instance, Peacock et al. (2001) [60] derived  $\beta(L_s = 0.17, z_s = 1.9L_*) = 0.43 \pm 0.07$  and Hawkins et al. (2003) [26] obtained  $\beta(L_s = 0.15, z_s = 1.4L_*) = 0.49 \pm 0.09$  and velocity dispersion  $\sigma_v = 506 \pm 52 \text{ km/sec}$ . Using the full 2dF+CMB likelihood function on the  $(b, \Omega_m)$  plane, Lahav et al. (2002) [38] derived a slightly larger (but consistent within the quoted error-bars) value,  $\beta(L_s = 0.17, z_s = 1.9L_*) \simeq 0.48 \pm 0.06$ .

### 6.3 Luminosity and spectral-type dependence of galaxy clustering

Although biasing was commonly neglected until the early 1980s, it has become evident observationally that on scales  $\lesssim 10 h^{-1} \text{ Mpc}$  different galaxy populations exhibit different clustering amplitudes, the so-called morphology-density relation [14]. As discussed in §4, galaxy biasing is naturally predicted from a variety of theoretical considerations as well as direct numerical simulations [33, 53, 13, 77, 78, 81]. Thus in this subsection, we summarize the extent to which the galaxy clustering is dependent on the luminosity, spectral-type and color of the galaxy sample from the 2dFGRS and SDSS.

#### 6.3.1 2dFGRS: Clustering per luminosity and spectral type

Madgwick et al. (2003) [41] applied the Principal Component Analysis to compress each galaxy spectrum into one quantity,  $\eta \approx 0.5 pc_1 + pc_2$ . Qualitatively,  $\eta$  is an indicator of the ratio of the present to the past star formation activity of each galaxy. This allows one to divide the 2dFGRS into  $\eta$ -types, and to study e.g. luminosity functions and clustering per type. Norberg et al.

(2002) [55] showed that, at all luminosities, early-type galaxies have a higher bias than late-type galaxies, and that the biasing parameter, defined here as the ratio of the galaxy to matter correlation function,  $b \equiv \sqrt{\xi_g/\xi_m}$  varies as  $b/b_* = 0.85 + 0.15L/L_*$ . Figure 25 indicates that for  $L_*$  galaxies, the real space correlation function amplitude of  $\eta$  early-type galaxies is  $\sim 50\%$  higher than that of late-type galaxies.

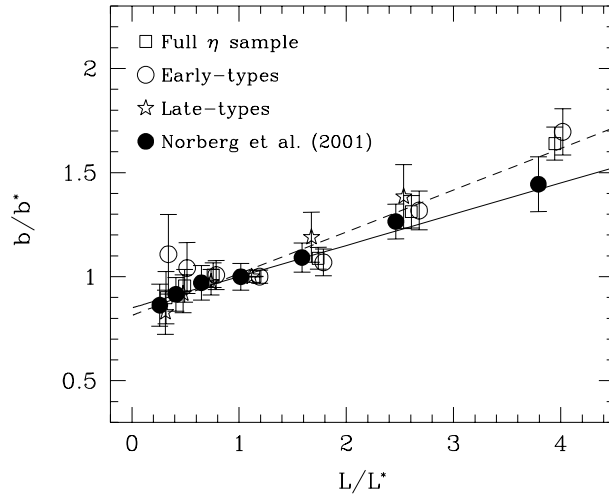


Figure 25: The variation of the galaxy biasing parameter with luminosity, relative to an  $L_*$  galaxy for the full sample and for subsamples of early and late spectra types (ref. [55]).

Figure 26 shows the redshift-space correlation function in terms of the line-of-sight and perpendicular to the line-of-sight separation  $\xi(\sigma, \pi)$ . The correlation function calculated from the most passively ('red', for which the present rate of star formation is less than 10 % of its past averaged value) and actively ('blue') star-forming galaxies. The clustering properties of the two samples are clearly distinct on scales  $\lesssim 10 h^{-1}$  Mpc. The 'red' galaxies display a prominent 'finger-of-god' effect and also have a higher overall normalization than the 'blue' galaxies. This is a manifestation of the well-known morphology-density relation. By fitting  $\xi(\pi, \sigma)$  over the separation range  $8 - 20 h^{-1}$  Mpc for each class, it was found that  $\beta_{active} = 0.49 \pm 0.13$ ,  $\beta_{passive} = 0.48 \pm 0.14$  and corresponding pairwise velocity dispersions  $\sigma_p$  of  $416 \pm 76$  km/sec and  $612 \pm 92$  km/sec [41]. At small separations, the real space clustering of passive galaxies is stronger than that of active galaxies, the slopes  $\gamma$  are respectively 1.93 and 1.50 (Fig. 27) and the relative bias between the two classes is a declining function of separation. On scales larger than  $10 h^{-1}$  Mpc the biasing ratio is approaching unity.

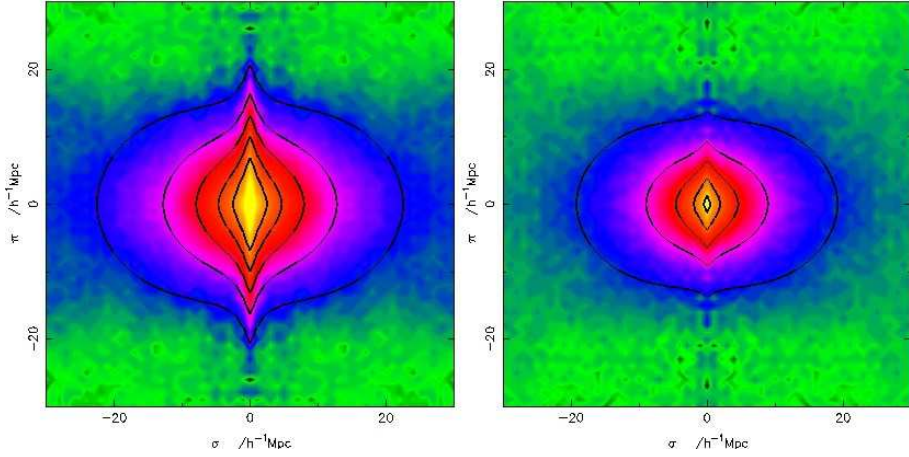


Figure 26: The two point correlation function  $\xi(\sigma, \pi)$  plotted for passively (left) and actively (right) star-forming galaxies. The line contours levels show the best-fitting model (ref. [41]).

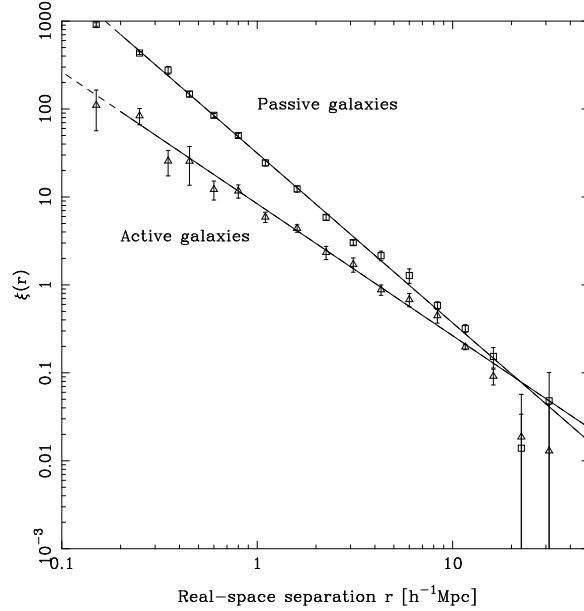


Figure 27: The correlation function for early and late spectral types. The solid lines show best-fitting models, whereas the dashes lines are extrapolations of these lines (ref. [41]).

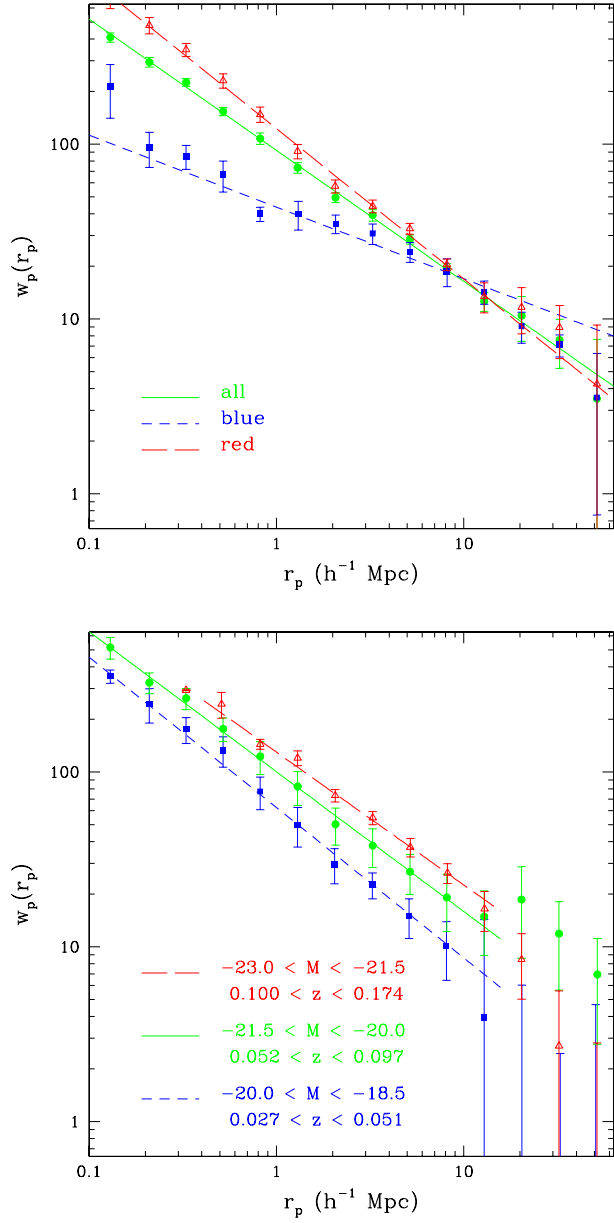


Figure 28: *Upper*: The SDSS (EDR) projected correlation function for blue (squares), red (triangles) and the full sample, with best-fitting models over the range  $0.1 < r_p < 16h^{-1}\text{Mpc}$ . *Lower*: The SDSS (EDR) projected correlation function for three volume-limited samples, with absolute magnitude and redshift ranges as indicated and best-fitting power-law models. (ref. [85])

### 6.3.2 SDSS: Clustering per luminosity and colour

Zehavi et al. (2002) [85] analysed the Early Data Release (EDR) sample of the SDSS 30,000 galaxies to explore the clustering of per luminosity and colour. The inferred real-space correlation function is well described by a single power-law;  $\xi(r) = (r/6.1 \pm 0.2h^{-1}\text{Mpc})^{-1.75 \pm 0.03}$ , for  $0.1h^{-1}\text{Mpc} \leq r \leq 16h^{-1}\text{Mpc}$ . The galaxy pairwise velocity dispersion is  $\sigma_{12} \approx 600 \pm 100\text{km/sec}$  for projected separations  $0.15h^{-1}\text{Mpc} \leq r_p \leq 5h^{-1}\text{Mpc}$ . When divided by color, the red galaxies exhibit a stronger and steeper real-space correlation function and a higher pairwise velocity dispersion than do the blue galaxies. In agreement with 2dFGRS there is clear evidence for scale-independent luminosity bias at  $r \sim 10h^{-1}\text{Mpc}$ . Subsamples with absolute magnitude ranges centered on  $M_* - 1.5$ ,  $M_*$ , and  $M_* + 1.5$  have real-space correlation functions that are parallel power laws of slope  $\approx -1.8$  with correlation lengths of approximately  $7.4h^{-1}\text{Mpc}$ ,  $6.3h^{-1}\text{Mpc}$ , and  $4.7h^{-1}\text{Mpc}$ , respectively.

Figures 27 and 28 pose an interesting challenge to the theory of galaxy formation, to explain why the correlation functions per luminosity bins have similar slope, while the slope for early type galaxies is steeper than for late type.

## 6.4 Topology of the universe: analysis of SDSS galaxies in terms of Minkowski functionals

All the observational results presented in the preceding subsections were restricted to the two-point statistics. As emphasized in §3, the clustering pattern of galaxies has much richer content than the two-point statistics can probe. Historically the primary goal of the topological analysis of galaxy catalogues was to test Gaussianity of the primordial density fluctuations. Although the major role for that goal has been superseded by the CMB map analysis [37], the proper characterization of the morphology of large-scale structure beyond the two-point statistics is of fundamental importance in cosmology. In order to illustrate a possibility to explore the topology of the universe by utilizing the new large surveys, we summarize the results of the Minkowski Functionals (MF) analysis of SDSS galaxy data [27].

In an apparent-magnitude limited catalogue of galaxies, the average number density of galaxies decreases with distance because only increasingly bright galaxies are included in the sample at larger distance. With the large redshift surveys it is possible to avoid this systematic change in both density and galaxy luminosity by construct volume-limited samples of galaxies, with cuts on both absolute-magnitude and redshift. This is in particular useful for analyses such as MF and was carried out in the analysis shown here.

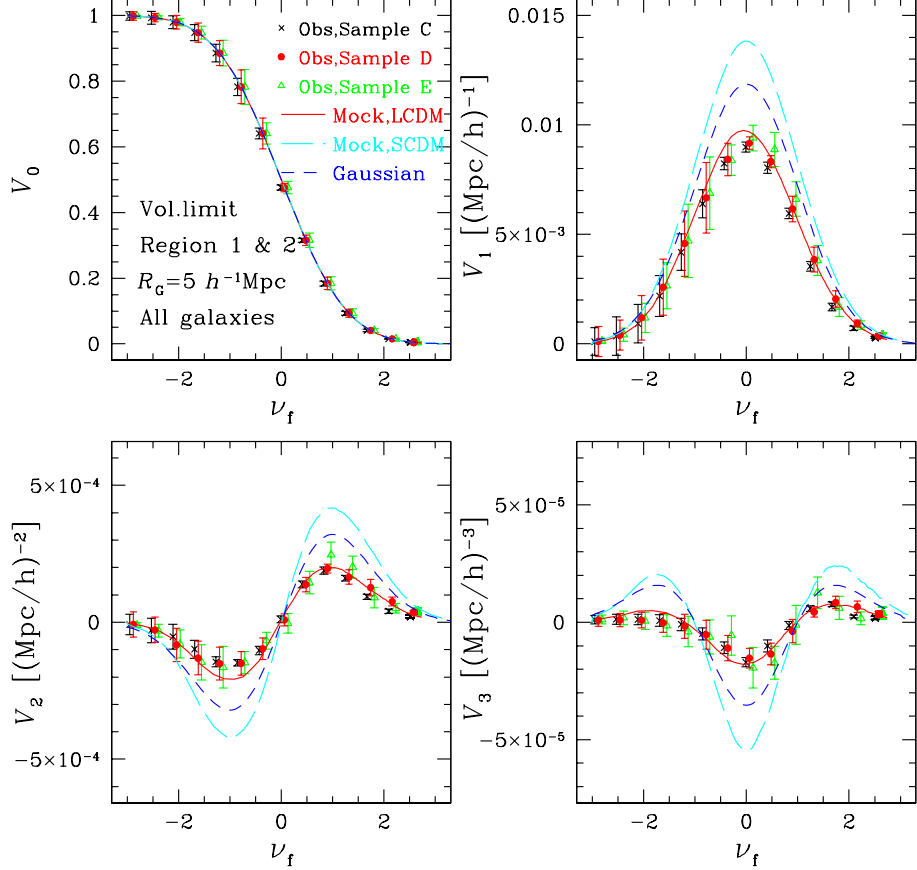


Figure 29: MFs as a function of  $\nu_f$  for  $R_G = 5h^{-1}\text{Mpc}$  for SDSS data. The results favor the LCDM model with random-Gaussian initial conditions. (ref. [27]).

Figure 29 shows the MFs as a function of  $\nu_f$  defined from the volume fraction [23]:

$$f = \frac{1}{\sqrt{2\pi}} \int_{\nu_f}^{\infty} e^{-x^2/2} dx. \quad (170)$$

This is intended to map the threshold so that the volume fraction on the high-density side of the isodensity surface is identical to the volume in regions with density contrast  $\delta = \nu_f \sigma$ , for a Gaussian random field with r.m.s. density fluctuations  $\sigma$ . If the evolved density field may approximately have a good one-to-one correspondence with the initial random-Gaussian field, then this transformation

removes the effect of evolution of the PDF of the density field. Under this assumption, the MFs as a function of volume fraction  $w$  would be sensitive only to the topology of the isodensity contours rather than evolution with time of the density threshold assigned to a contour. While the limitations of the approximation of monotonicity in the relation between initial and evolved density fields are well recognized [35], we plot the result in this way for simplicity.

The good match between the observed MFs and the mock predictions based on the  $\Lambda$ CDM model with the initial random-Gaussianity, as illustrated in Figure 29, might be interpreted to imply that the primordial Gaussianity is confirmed. A more conservative interpretation is that, given the size of the estimated uncertainties, these data do not provide evidence for initial non-Gaussianity, i.e., the data are *consistent* with primordial Gaussianity. Unfortunately due to the statistical limitation of current SDSS data, it is not easy to put more quantitative statement concerning the initial Gaussianity, but this is definitely what we intend to conduct with the improved datasets available in near future. Moreover, in order to go further and place more quantitative constraints on primordial Gaussianity with upcoming data, one needs a more precise and reliable theoretical model for the MFs which properly describes the nonlinear gravitational effect possibly as well as galaxy biasing beyond the simple mapping on the basis of the volume fraction. In fact, galaxy biasing is a major source of uncertainty for relating the observed MFs to those obtained from the mock samples for dark matter distributions. If  $\Lambda$ CDM is the correct cosmological model, the good match of the MFs for mock samples from the  $\Lambda$ CDM simulations to the observed SDSS MFs may indicate that nonlinearity in the galaxy biasing is relatively small, at least small enough that it does not significantly affect the MFs (the MFs as a function of  $\nu_\sigma$  remain unchanged for the linear biasing). Furthermore, the dependence of the nonlinearity of the biasing on the luminosity and the morphological type of galaxies is also very small. The observational results that the effect of the galaxy biasing on the MFs is small is consistent with the predictions of theoretical studies [6].

## 6.5 Other statistical measures

In this section, we have presented the results on the basis of particular statistical measures including the two-point correlation functions, power spectrum, redshift distortion, and Minkowski functionals. Of course there are other useful approaches in analysing redshift surveys; the void probability function, counts-in-cells, Voronoi cells, percolation, and minimal spanning trees. Another area not covered here is optimal reconstruction of density field (e.g, using the Wiener filtering). The reader is referred to a good summary of those and other methodology in the book by Martinez & Saar (2002) [44].

Admittedly the results that we presented here are rather observational and phenomenological, and far from being well-understood theoretically. It is quite likely that when other on-going and future surveys are be analysed in great

detail, the nature of galaxy clustering will be revealed in a much more quantitative manner. They are supposed to act as a bridge between cosmological framework and galaxy formation operating in the universe. While the proper understanding of physics of galaxy formation is still far away, the future redshift survey data will present interesting challenges for constructing models of galaxy formation.

## 7 Discussion

While a classical probe, galaxy redshift surveys still remain an important tool for studying cosmology and galaxy formation. The exponential growth of redshift surveys has changed the character of the subject, in the sense that models can now be assessed quantitatively in great detail.

The redshift surveys mainly constrain  $\Omega_m$  via both redshift distortion (which also depends on biasing) and the shape of the  $\Lambda$ CDM power spectrum, which depends on the primordial spectrum, the product  $\Omega_m h$  and also the baryon density  $\Omega_b$ . Redshift surveys are not so sensitive to the Dark Energy (or the Cosmological Constant, in a specific case), but combined with the CMB they can constrain the Equation of State.

With the development of other probes, most notably the Cosmic Microwave Background, Supernovae Ia and Gravitational Lensing, the redshifts surveys may not be in the leading position in estimating cosmological parameters. As illustrated in §6, however, they are complementary and thus still very useful in constraining the cosmological parameters [72].

In 1960's, Sandage referred to the goal of cosmology as "a search for two numbers". It is now appreciated, however, that even the basic cosmological model requires a dozen or so parameters or even functions, which are linked in non-trivial ways. Different cosmological probes measure different combinations of parameters, given below just approximately.

1. big bang nucleosynthesis and the abundance of light elements:  $\Omega_b h^2$
2. the cosmic microwave background:  $\Omega_\Lambda + \Omega_m$ ,  $\Omega_m h^2$ ,  $\Omega_b h^2$ ,  $\sigma_8 e^{-\tau}$ ,  $n$ ,  $t_0$
3. the Hubble diagram of distant Type Ia Supernovae:  $3\Omega_\Lambda - 4\Omega_m$
4. redshift surveys of galaxies:  $\Omega_m^{0.6}/b$ ,  $b\sigma_8$ ,  $\Omega_m h$
5. peculiar velocities of galaxies:  $\sigma_8 \Omega_m^{0.6}$ ,  $\Omega_m h$
6. cluster abundance:  $\sigma_8 \Omega_m^{0.6}$ ,  $\Omega_m h$
7. weak lensing:  $\sigma_8 \Omega_m^{0.6}$ ,  $\Omega_m h$
8. baryon fraction in galaxy clusters:  $\Omega_b$ ,  $\Omega_m$ ,  $h$
9. quasar absorption lines:  $\sigma_8$ ,  $\Omega_m h$ ,  $\Omega_b h^2$
10. Cepheids, the Sunyaev-Zel'dovich effect, the time-delay in multiple gravitationally lensed quasar systems:  $h$

The first-year WMAP data combined with the other available cosmological probes (including the 2dFGRS among others) have established a set of cosmological parameters as summarized in Table 2. Some of the parameters is derived through the WMAP analysis alone, but mostly they are fitted assuming the

Table 2: Best-estimates of the cosmological parameters in 2003 (derived combining the WMAP result with other cosmological probes. see ref. [5] for detail.)

Symbol	Value	description
$\Omega_{\text{tot}}$	$1.02 \pm 0.02$	total energy density parameter
$w$	$< -0.78$	ratio of pressure and density of dark energy (95% CL)
$\Omega_{\Lambda}$	$0.73 \pm 0.04$	density parameter of cosmological constant
$\Omega_b$	$0.044 \pm 0.004$	baryon density parameter
$\Omega_m$	$0.27 \pm 0.04$	total matter (non-relativistic) density parameter
$\Omega_{\nu} h^2$	$< 0.0076$	upper limit on neutrino density parameter (95% CL)
$\Omega_b/\Omega_m$	$0.17 \pm 0.01$	mass fraction of baryon to matter
$h$	$0.71^{+0.04}_{-0.03}$	(dimensionless) Hubble constant
$\sigma_8$	$0.84 \pm 0.04$	mass fluctuation amplitude at $8h^{-1}\text{Mpc}$
$n_s$	$0.93 \pm 0.03$	primordial spectral index at $k_0 = 0.05 \text{ Mpc}^{-1}$
$z_{\text{dec}}$	$1089 \pm 1$	redshift at decoupling of matter and radiation
$t_0$	$13.7 \pm 0.2 \text{Gyr}$	present age of the universe
$t_{\text{dec}}$	$379^{+8}_{-7} \text{kyr}$	age of the universe at decoupling
$t_{\text{r}}$	$0.18^{+0.22}_{-0.08} \text{Gyr}$	age of the universe at reionization
$z_{\text{r}}$	$20^{+10}_{-9}$	redshift at reionization

$\Lambda$ -CDM model, and thus not completely free from the not-yet-justifiable assumption. While the degree of such phenomenological successes of the  $\Lambda$ -CDM model is truly amazing, there are many fundamental open questions:

- (i) Both components of the model,  $\Lambda$  and CDM, have not been directly measured. Are they ‘real’ entities or just ‘epicycles’? Historically epicycles were actually quite useful in forcing observers to improve their measurements and theoreticians to think about better models!
- (ii) ‘The Old Cosmological Constant problem’: Why is  $\Omega_{\Lambda}$  at present so small relative to what is expected from Early Universe physics?
- (iii) ‘The New Cosmological Constant problem’: Why is  $\Omega_m \sim \Omega_{\Lambda}$  at the present-epoch ? Why is  $w \sim -1$  ? Do we need to introduce new physics or to invoke the Anthropic Principle to explain it ?
- (iv) There are still open problems in  $\Lambda$ -CDM on the small scales e.g. galaxy profiles and satellites.
- (v) Could other (yet unknown) models fit the data equally well ?
- (vi) Where does the field go from here ? Should the activity focus on refinement of the cosmological parameters within  $\Lambda$ -CDM, or on introducing entirely new paradigms ?

Table 3: *Expanding* the expanding universe.

order	topic
$(\text{Cosmology})_{(0)}$	isotropic and homogeneous space-time [ cosmological parameters; $\Omega_0, \lambda_0, h$ ]
$(\text{Cosmology})_{(1)}$	CMB and large-scale structure of dark matter distribution [ primordial density fluctuations, nature of dark matter ]
$(\text{Cosmology})_{(2)}$	nonlinear growth of mass density fluctuations [ nonlinear spherical model, Press-Schechter theory, N-body simulations ]
$(\text{Cosmology})_{(3)}$	formation and evolution of luminous objects [ hydrodynamical evolution of gas, radiative processes, supernova feedback, biasing ]
...	...
$(\text{Cosmology})_{(L)}$	origin of matter [ photons, baryons, leptons, dark matter, dark energy, ... ]
...	...
$(\text{Cosmology})_{(M)}$	origin of life [ search for habitable planets, astrobiology, biocosmology, ... ]
...	...
$(\text{Cosmology})_{(N)}$	development of intelligence [ culture, civilization, religion, social system, ... ]
...	...
$(\text{Cosmology})_{(\infty)}$	origin/fate of the universe

Suppose that the cosmological research can be expanded (with respect to whatever parameter !) as follows:

$$\text{Cosmology} = \sum_{n=0}^{\infty} (\text{Cosmology})_{(n)}. \quad (171)$$

This expansion itself is definitely quite subjective, and never guaranteed for convergence by any means. Still let us show an ill-defined version of expansion in Table 3. Even if this expansion is very controversial, the determination of the values of the cosmological parameters should be the most fundamental, and therefore, the 0-th order task in cosmology. At present we are almost completing the 1st and 2nd order research in cosmology in the Table, and keep working on the 3rd order and beyond. Naturally the concept and the topics covered by the field of *cosmology* should evolve accordingly. Whether the present/upcoming *Precision Cosmology* is our goal or just a beginning of the next really depends critically on a personal taste of each individual researcher. Nevertheless given the incomplete but still vast list of topics which remain to be understood, we would like to say that the determination of the cosmological parameters is just the beginning for the *Physical Cosmology*.

## 8 Acknowledgements

We thank Joachim Wambsganss and Bernard Schutz for inviting us to write the present review article. O.L. thanks members of the 2dFGRS team and the Leverhulme Quantitative Cosmology group for helpful discussions. Y.S. thanks all his students and collaborators for over many years, in particular, Thomas Buchert, Takashi Hamana, Chiaki Hikage, Yipeng Jing, Issha Kayo, Hiromitsu Magira, Takahiko Matsubara, Hiroaki Nishioka, Jens Schmalzing, Atsushi Taruya, Kazuhiro Yamamoto, and Kohji Yoshikawa among others, for enjoyable and fruitful collaborations whose results form indeed the important elements in this review. Y.S. is also grateful for the hospitality at Institute of Astronomy, University of Cambridge, where the most of present review was put together and written up for completion. We also thank Idit Zehavi for permitting us to use Figure 28.

Numerical simulations were carried out at ADAC (the Astronomical Data Analysis Center) of the National Astronomical Observatory, Japan (project ID: mys02, yys08a). This research was also supported in part by the Grants-in-Aid from Monbu-Kagakusho and Japan Society of Promotion of Science.

## References

- [1] Ahmad, Q. R. *et al.*, *Phys. Rev. Lett.*, **87**, 071301 (2001)
- [2] Alcock, C., & Paczynski, B., *Nature*, **281**, 358 (1979)
- [3] Ballinger, W.E., Peacock, J.A., & Heavens, A.F., *MNRAS*, **282**, 877 (1996)
- [4] Bardeen, J. M., Bond, J. R., Kaiser, N., & Szalay, A. S., *Astrophys. J.*, **304**, 15 (1986)
- [5] Bennett, C.L., *et al.*, *Astrophys. J. Suppl.*, **148**, 1–27 (2003)
- [6] Benson, A. J., Frenk, C. S., Baugh, C. M., Cole, S., & Lacey, C. G., *MNRAS*, **327**, 1041 (2001)
- [7] Boyle, B. J., Shanks, T., Croom, S. M., Smith, R. J., Miller, L., Loaring, N., & Heymans, C., *MNRAS*, **317**, 1014 (2000)
- [8] Bullock J. S., Wechsler, R. H., Somerville R. S., *MNRAS*, **329**, 346 (2002)
- [9] Coles, P., & Jones, B., *MNRAS*, **248**, 1 (1991)
- [10] Coles, P. & Lucchin, F., *Cosmology - The Origin and Evolution of Cosmic Structure*, 2nd edition 2002, John Wiley & Sons, Chichester

- [11] Colless, M. to appear in Carnegie Observatories Astrophysics Series, Vol.2: Measuring and Modeling the Universe, ed. W.L. Freedman (Cambridge: Cambridge University Press) (2003) astro-ph/0305051
- [12] Cooray, A. & Sheth, R., *Phys.Rep.*, **372**, 1–129 (2002)
- [13] Dekel, A. & Lahav, O., *Astrophysical J.*, **520**, 24 (1999)
- [14] Dressler, A., *Astrophys. J.*, **236**, 351 (1980)
- [15] Elgaroy, O. et al., *Phys Rev L*, **89**, 061301 (2002)
- [16] Elgaroy, O., & Lahav, O., *Journal of Cosmology and Astroparticle Physics*, **4**, 004 (2003)
- [17] Efstathiou G P *et al.*, *MNRAS*, **330**, L29 (2002)
- [18] Ehlers, J., Geren, P. & Sachs, R.K., *J Math Phys*, **9(9)**, 1344 (1968)
- [19] Freedman, W.L. et al., *ApJ*, **553**, 47 (2001)
- [20] Fry J.N., *Astrophys. J.*, **461**, L65 (1996)
- [21] Fukuda, S. *et al.*, *Phys. Rev. Lett.*, **85**, 3999 (2000)
- [22] Gaztañaga, E., & Yokoyama, J., *Astrophys. J.*, **403**, 450 (1993)
- [23] Gott, J. R. III, Mellot, A. L., & Dickinson, M., *Astrophys. J.*, **306**, 341 (1986)
- [24] Hamana, T., Colombi, S., & Suto, Y., *A & A*, **367** 18–26 (2001)
- [25] Hamana, T., Yoshida, N., Suto, Y., & Evrard, A.E., *Astrophys. J.*, **561** L143–L146 (2001)
- [26] Hawkins E., et al., *MNRAS*, in press, (2003) astro-ph/0212375
- [27] Hikage et al., *Pub.Astron.Soc.Japan*, **55**, in press (2003)
- [28] Hinshaw, G., et al., *Astrophys. J. Suppl.*, **148**, 63–95 (2003)
- [29] Hu, W., Eisenstein, D., Tegmark, M., *Phys Rev Lett*, **80**, 5255 (1998)
- [30] Hubble, E. P., *Astrophys. J.*, **79**, 8 (1934)
- [31] Jing, Y. P., & Suto, Y., *Astrophys. J.*, **494**, L5 (1998)
- [32] Jing, Y.P., *Astrophys. J.*, **503**, L9 (1998)
- [33] Kaiser, N., *Astrophys. J.*, **284**, L9 (1984)
- [34] Kaiser, N., *MNRAS*, **227** 1–21 (1987)

- [35] Kayo, I., Taruya, A., & Suto, Y., *Astrophys. J.*, **561**, 22 (2001)
- [36] Kogut, A., et al., *Astrophys. J. Suppl.*, **148**, 161–173 (2003)
- [37] Komatsu, E., et al., *Astrophys. J. Suppl.*, **148**, 119–134 (2003)
- [38] Lahav, O. et al., *MNRAS*, **333**, 961 (2002)
- [39] Landy, S.D., & Szalay, A.S., *ApJ*, **412**, 64 (1993)
- [40] Loveday, J., Peterson, B. A., Efstathiou, G., & Maddox, S. J., *ApJ*, **390**, 338 (1992)
- [41] Madgwick, D.S., et al., *MNRAS*, in press (2003) astro-ph/0303668
- [42] Magira, H., Jing, Y.P., & Suto, Y., *Astrophys. J.*, **528** 30–50 (2000)
- [43] Magliocchetti, M., & Porciani, C., *MNRAS*, in press (2003) astro-ph/0304003
- [44] Martinez, V.J. & Saar, E., *Statistics of the Galaxy Distribution*, Chapman & Hall/CRC (2002)
- [45] Matsubara, T., *Astrophys. J.*, **434**, 43 (1994)
- [46] Matsubara, T., *Astrophys. J.*, **584**, 1 (2003)
- [47] Matsubara, T., & Suto, Y., *Astrophys. J.*, **460**, 51 (1996)
- [48] Matsubara, T., & Suto, Y., *Astrophys.J.*, **470**, L1–L5 (1996)
- [49] Matsubara, T., & Szalay, A.S., *Astrophys.J.*, **574**, 1 (2002)
- [50] Matsubara, T., & Szalay, A.S., *Phys.Rev.Lett.*, **90**, 021302 (2003)
- [51] Mo, H.J., Jing, Y.P., & Börner, G., *MNRAS*, **286**, 979 (1997)
- [52] Mecke, K. R., Buchert, T. & Wagner, H., *A&A*, **288**, 697 (1994)
- [53] Mo, H., & White, S.D.M., *MNRAS*, **282**, 347 (1996)
- [54] Nakamura, T.T., Matsubara, T., & Suto, Y., *Astrophys.J.*, **494**, 13–19 (1998)
- [55] Norberg P. et al., *MNRAS*, **332**, 827 (2002)
- [56] Padmanabhan, T., “*Structure Formation in the Universe*”, (Cambridge University Press, Cambridge, 1993)
- [57] Padmanabhan, T., *Galaxies and Cosmology (Theoretical Astrophysics: Volume 3*, Cambridge University Press (2003)

- [58] Peacock, J.A., “*Cosmological Physics*”, (Cambridge University Press, Cambridge, 1999)
- [59] Peacock, J.A. & Dodds, S.J., MNRAS, **280**, L19 (1994)
- [60] Peacock, J.A., Nature, **410**, 169(2001)
- [61] Peacock, J.A., to appear in the proceedings of the 13th Annual October Astrophysics Conference in Maryland: The Emergence of Cosmic Structure, eds. S. Holt and C. Reynolds (AIP) (2003), astro-ph/0301042
- [62] Peebles, P.J.E. , “*Large-scale Structure of the universe*”, (Princeton University Press, Princeton, 1980)
- [63] Peebles, P.J.E. , “*Principles of Physical Cosmology*”, (Princeton University Press, Princeton, 1993)
- [64] Peiris, H.V., et al., Astrophys. J. Suppl., **148**, 213–231 (2003)
- [65] Pen U.L., Astrophys.J., **504**, 601 (1998)
- [66] Percival, W.J. et al., MNRAS, **337**, 1068 (2002)
- [67] Rudnicki, K., *The cosmological principles*, (Jagiellonian University, Krakow, 1995)
- [68] Saslaw, W., “*Gravitational Physics of Stellar and Galactic Systems*” (Cambridge University Press, Cambridge, 1985)
- [69] Scharf, C.A., Jahoda, K., Treyer, M., Lahav, O., Boldt, E. & Piran, T., Astrophys. J., **544**, 49 (2000)
- [70] Seljak U., MNRAS, **318**, 203 (2000)
- [71] Somerville, R. S., Lemson, G., Sigad, Y., Dekel, A., Kauffmann, G. White, S. D. M., MNRAS, **320**, 289 (2001)
- [72] Spergel, D.N., et al., Astrophys. J. Suppl., **148**, 175–194 (2003)
- [73] Strauss, M. A., et al., Astron. J., **124**, 1810 (2002)
- [74] Suto, Y., Prog.Theor.Phys., **90**, 1173 (1993)
- [75] Suto, Y., Magira, H., Jing, Y.P., Matsubara, T., & Yamamoto, K., Prog. Theor. Phys. Suppl., **133**, 183–210 (1999)
- [76] Suto, Y., Magira, H., & Yamamoto, K., Pub.Astron.Soc.Japan, **52**, 249–257 (2000)
- [77] Taruya, A. & Suto, Y., Astrophys.J., **542**, 559 (2000)

- [78] Taruya, A., Magira, H., Jing, Y.P., & Suto, Y., Pub.Astron.Soc.Japan, **53**, 155–167 (2001)
- [79] Yamamoto, K., & Suto, Y., *Astrophys. J.*, **517** 1–12 (1999)
- [80] Yamamoto, K., Nishioka, H., & Suto, Y., *Astrophys. J.*, **527** 488–497 (1999)
- [81] Yoshikawa, K., Taruya, A., Jing, Y.P., & Suto, Y., *Astrophysical J.*, **558**, 520–534 (2001)
- [82] Weinberg, S., “*Gravitation and Cosmology*”, (John Wiley & Sons, New York, 1972)
- [83] Wu, K.K.S., Lahav, O. & Rees, M.J., *Nature*, **397** , 225 (1999)
- [84] York, D. G., et al., *Astron. J.*, **120**, 1579 (2000)
- [85] Zehavi, I. et al. *ApJ*, **571**, 172 (2002)
- [86] Zehavi, I. et al., *Astrophys.J.*, in press. (2003) astro-ph/0301280